

12-2009

FIRST-PRINCIPLES DENSITY FUNCTIONAL
THEORY STUDIES OF REACTIVITIES OF
HETEROGENEOUS CATALYSTS
DETERMINED BY STRUCTURE AND
SUBSTRATE

Lei Cheng

Southern Illinois University Carbondale, leicheng@siu.edu

Follow this and additional works at: <http://opensiuc.lib.siu.edu/dissertations>

Recommended Citation

Cheng, Lei, "FIRST-PRINCIPLES DENSITY FUNCTIONAL THEORY STUDIES OF REACTIVITIES OF HETEROGENEOUS CATALYSTS DETERMINED BY STRUCTURE AND SUBSTRATE" (2009). *Dissertations*. Paper 99.

This Open Access Dissertation is brought to you for free and open access by the Theses and Dissertations at OpenSIUC. It has been accepted for inclusion in Dissertations by an authorized administrator of OpenSIUC. For more information, please contact opensiuc@lib.siu.edu.

FIRST-PRINCIPLES DENSITY FUNCTIONAL THEORY STUDIES OF
REACTIVITIES OF HETEROGENEOUS CATALYSTS DETERMINED BY
STRUCTURE AND SUBSTRATE

by

Lei Cheng

B.S., Qingdao University, China, 2003

A Dissertation
Submitted in Partial Fulfillment of the Requirements for the
Doctor of Philosophy

Department of Chemistry and Biochemistry
in the Graduate School
Southern Illinois University Carbondale
December, 2009

Copyright by Lei Cheng, 2009
All Rights Reserved

DISSERTATION APPROVAL

FIRST-PRINCIPLES DENSITY FUNCTIONAL THEORY STUDIES OF
REACTIVITIES OF HETEROGENEOUS CATALYSTS DETERMINED BY
STRUCTURE AND SUBSTRATE

By

Lei Cheng

A Dissertation Submitted in Partial

Fulfillment of the Requirements

for the Degree of

Doctor of Philosophy

in the field of Chemistry

Approved by:

Qingfeng Ge, Chair

Boyd Goodson

Brian Lee

Punit Kohli

Leo Silbert

Graduate School
Southern Illinois University Carbondale

June 24th, 2009

AN ABSTRACT OF THE DISSERTATION OF

LEI CHENG, for the Doctor of Philosophy degree in Physical Chemistry, presented on June, 2009, at Southern Illinois University Carbondale.

TITLE: FIRST-PRINCIPLES DENSITY FUNCTIONAL THEORY STUDIES OF REACTIVITIES OF HETEROGENEOUS CATALYSTS DETERMINED BY STRUCTURE AND SUBSTRATE

MAJOR PROFESSOR: Dr. Qingfeng Ge

In this dissertation, density functional theory (DFT) calculations were used to investigate (1) NO₂ adsorption on BaO in NO_x Storage Reduction (NSR) catalyst affected by the morphology of BaO and the γ -Al₂O₃ support, (2) energy barrier of H₂ dissociative adsorption over Mg clusters affected by its electronic structure, and (3) comparison of the activities of CeO₂ clusters affected by two different supports—monoclinic ZrO₂ and non-spinel γ -Al₂O₃. Our results showed that the electronic effect caused by the non-stoichiometry of the bare BaO clusters and surfaces improves their reactivities toward NO₂ adsorption greatly, whereas the geometric structure of the catalyst has only minor effect on the activity; we also found that the γ -Al₂O₃ substrate improves the reactivities of the supported BaO clusters and at the same time the interface between BaO and γ -Al₂O₃ provided a unique and highly reactive environment for NO₂ adsorption. Hydrogen dissociation barrier over pure Mg clusters is greatly affected by the electronic structure of the clusters—closed shell clusters such as Mg₁₀ and Mg₉²⁻ have higher energy barrier toward H₂ dissociation; however, H₂ dissociation over clusters that are two electrons shy from the closed electronic shell are relatively easier. As substrates, neither ZrO₂(111) nor

γ -Al₂O₃(100) affects the reactivity of the supported Ce₂O₄ toward CO₂ adsorption and CO physisorption significantly; whereas the reactivity of Ce₂O₄ toward CO reactive adsorption were found to be affected by the two substrates very differently.

DEDICATION

To my family:

Father, Shaozhong Cheng

Mother, Yumin Shi

FOR THEIR LOVE, ENCOURAGEMENT AND BELIEVEING...

ACKNOWLEDGMENTS

I would like to give my appreciation to my research advisors, Dr. Qingfeng Ge for giving me the freedom to explore on my own, and at the same time providing patient guidance, encouragement and support. He has inspired me by his great research capabilities and desire to accomplish great goals. These are lessons that will benefit me for a lifetime. Thanks for all of the advice and motivation.

Thanks to Dr. Lichang Wang for always being there to listen and advise. I am grateful for her regard and help both on my research and on my life through my graduate study.

Special thanks to Dr. Donghai Mei at Pacific Northwest National Laboratory for mentoring me during my stay at PNNL and being a good friend.

I would like to extend my gratitude to my committee members Dr. Boyd Goodson, Dr. Brian Lee, Dr. Punit Kohli, Dr. Leo Silbert, Dr. Andrei Kolmakov and Dr. Ling Zang (now at University of Utah) for their time, constructive suggestions in my research and help throughout my graduate studies.

I would like to thank Jianjun Liu, Yunxiang Pan, Jiamei Yu, George Hudson, Tiffany Pawluk, Jenifer Yukna, Li Xiao and You Han, for the successful collaborations and wonderful discussions on my research. Special thanks to all the members of our big theoretical chemistry family for your help during the last few years.

Thanks all of my friends in the Chemistry Department: Lijuan Peng, Ping He, Lin Wang, Chasity Love, Panayiotis Nikolaou, Chuansong Duanmu, Xuelian Li, Xuegang Jia, Tao Lin, XiaoXia Li, Nicholas Whiting, Mark Sadek for the great times during my graduate study. Without them, life wouldn't have been this fun.

Finally, I wish to acknowledge my parents, who always support me and have been always proud of me. THANKS!

PREFACE

Partial content in Chapter 3 of this dissertation was previously published as *Surf. Sci.* 601, L65-L68 in 2007 (copyright 2007 Elsevier) and *J. Phys. Chem. C* 112, 16924-16931 in 2008 (copyright 2008 American Chemical Society). Content of Chapter 5 was previously published as *J. Phys. Chem. C* 113, 18296 in 2009 (copyright 2009 American Chemical Society). The author of Elsevier retains the right to include the journal article, in full or in part, in a thesis or dissertation. ACS extends blanket permission to students to include in their theses and dissertations their own articles, or portions thereof, that have been published in ACS journals or submitted to ACS journals for publication. ACS copyright credit line is noted on the appropriate pages in this dissertation.

TABLE OF CONTENTS

<u>CHAPTER</u>	<u>PAGE</u>
ABSTRACT	i
DEDICATION	iii
ACKNOWLEDGMENTS	iv
PREFACE	vi
LIST OF TABLES	xi
LIST OF FIGURES	xii
LIST OF EQUATIONS	xv
LIST OF SCHEMES	xvii
CHAPTERS	
CHAPTER 1: General Introduction and Outline	1
CHAPTER 2: Computational Methods	4
2.1 A Brief History of Quantum Mechanics	4
2.2 Density Functional Theory	6
2.2.1 Thomas-Fermi Theory	7
2.2.2 Hohenberg-Kohn Theory	9
2.2.3 Kohn-Sham Equations	10
2.2.4 The Functional Effect	12
2.2.5 Overview of the Theory	14
2.2.5.1 Major Contributions of Theory	14
2.2.5.2 Applications	16
2.3 Locating Transition States	18
2.4 Computational Codes	20

2.4.1 VASP	21
2.4.2 Gaussian 03	27
2.5 Computational Facilities	28
CHAPTER 3: Effect of Morphology, Stoichiometry and Support on Reactivity of	
Catalysts: NO ₂ Interaction with Unsupported and γ -Al ₂ O ₃	
Supported BaO	30
3.1 Introduction.....	30
3.2 Methodology	34
3.2.1 General Method	34
3.2.2 Modeling of Bare BaO Clusters, (100) and (310) Surfaces.....	34
3.2.3 Modeling of γ -Al ₂ O ₃ Supported BaO Clusters	35
3.3 Results and Discussion	37
3.3.1 NO ₂ Interaction with BaO(100) Surfaces	37
3.3.2 NO ₂ Interaction with Stoichiometric BaO Clusters and Stepped	
Surface	39
a. Stoichiometric Clusters	39
b. Stoichiometric Stepped Surface	43
3.3.3 NO ₂ Interaction with Non-stoichiometric BaO Surfaces and	
Clusters	46
a. Non-stoichiometric Clusters.....	46
b. Non-stoichiometric Surface	49
3.3.4 NO ₂ Interaction with γ -Al ₂ O ₃ Supported BaO Clusters	51
a. γ -Al ₂ O ₃ Supported BaO Clusters	51

b. NO ₂ Adsorption on γ -Al ₂ O ₃ Supported BaO Clusters	54
c. NO ₂ Adsorption on γ -Al ₂ O ₃ Supported BaO Clusters with Bigger Unit Cell	58
3.4 Conclusion	63
CHAPTER 4: Electronic Shell Effect on Reactivity of Small Metal Cluster— Examples of H ₂ Desorption on Magnesium Clusters	65
4.1 Introduction.....	65
4.2 Methodology	66
4.3 Results and Discussion	68
4.3.1 Structures of Mg ₉ , Mg ₉ ²⁺ , Mg ₉ ²⁻ , Mg ₁₀ and Mg ₁₀ ²⁺ Clusters	68
4.3.2 H ₂ Dissociation over Mg ₉ , Mg ₉ ²⁺ , Mg ₉ ²⁻ , Mg ₁₀ and Mg ₁₀ ²⁺ Clusters	71
4.3.3 Comparison of H ₂ Dissociation over Mg Clusters and Surfaces	78
4.4 Conclusion	79
CHAPTER 5: Origin of Support Effects on the Reactivity of Ceria Cluster	81
5.1 Introduction.....	81
5.2 Methodology	84
5.3 Results and Discussion	86
5.3.1 Adsorption of CO and CO ₂ on the ZrO ₂ (111) and γ -Al ₂ O ₃ (100) Surfaces.....	86
a. CO Adsorption	86
b. CO ₂ Adsorption.....	88
5.3.2 Ce ₂ O ₄ Cluster on the ZrO ₂ (111) and γ -Al ₂ O ₃ (100) Supports	89
5.3.3 CO ₂ Adsorption on the Supported Ce ₂ O ₄ Clusters	91

5.3.4 CO Adsorption on Ce Sites of the Supported Ce ₂ O ₄ Clusters	93
5.3.5 The Reactivity of the ZrO ₂ (111) and γ -Al ₂ O ₃ (100) Supported Ce ₂ O ₄ Clusters	94
5.4 Conclusion	104
CHAPTER 6: Summary	105
 BIBLIOGRAPHY	 106
APPENDICES	
Appendix I: VASP Input Files	119
Appendix II: Gaussian Input Files	124
VITA	125

LIST OF TABLES

<u>TABLE</u>	<u>PAGE</u>
Table 3.1 Atomic Bader Charges in BaO-Only and Synergistic Configurations	62
Table 4.1 H ₂ dissociation energy barrier (eV) over Mg clusters calculated using Gaussian with both B3LYP and PBE functional, as well as using VASP with PBE functional.	72
Table 4.2 H ₂ dissociation adsorption activation energies (eV) decomposed to H-H splitting energy cost and pure adsorption energies. Imaginary frequencies (cm ⁻¹) of H-H splitting were also reported. All results are PBE calculations....	75
Table 4.3 Band gaps (eV) of magnesium clusters and their corresponding transition states.....	76
Table 5.1 Calculated reactive adsorption energies (eV) of CO on the unsupported Ce ₂ O ₄ cluster (E _{ads}), an on the ZrO ₂ (111) and γ-Al ₂ O ₃ (100) supported Ce ₂ O ₄ cluster (E _{ads} ^s); the binding energies of Ce ₂ O ₄ cluster (E _{bind}) and (Ce ₂ O ₂) ²⁺ CO ₃ ²⁻ (E _{int}) on the ZrO ₂ (111) and the γ-Al ₂ O ₃ (100) substrates	98

LIST OF FIGURES

<u>FIGURE</u>	<u>PAGE</u>
Figure 2.1 A contour plot of potential energy surface for a three-atom system	19
Figure 2.2 Bulk CeO ₂ structure.....	22
Figure 2.3 Examples of unit cells of bulk CeO ₂ structure, a single CO ₂ molecule, and CeO ₂ (111) surface	25
Figure 3.1 Mechanism of NO _x storage reduction catalysis.....	31
Figure 3.2 The supercells of non-stoichiometric spinel Al ₁₈ O ₂₄ and stoichiometric defective spinel Al ₁₆ O ₂₄ after removing two Al atoms	36
Figure 3.3 Side view of γ -Al ₂ O ₃ (111) surface	37
Figure 3.4 Top view of the adsorption geometries and energies of NO ₂ on the BaO(100) surface	39
Figure 3.5 The adsorption geometries and energies of NO ₂ over the stoichiometric BaO clusters	41
Figure 3.6 BaO(310) surface and NO ₂ adsorption on the surface	45
Figure 3.7 NO ₂ adsorption on the non-stoichiometric clusters.....	47
Figure 3.8 Top view of NO ₂ adsorption on defective BaO(100).....	49
Figure 3.9 (BaO) ₂ supported on γ -Al ₂ O ₃ (111) with BaO cluster square plane parallel and normal to the support surface.....	53
Figure 3.10 Most stable structures of γ -Al ₂ O ₃ (111) supported (BaO) ₁ and (BaO) ₄	54
Figure 3.11 NO ₂ adsorption over γ -Al ₂ O ₃ (111) supported (BaO) ₁ O site and Ba site .	55
Figure 3.12 Synergistic adsorption of NO ₂ on γ -Al ₂ O ₃ (111) supported (BaO) ₂ and (BaO) ₄	56

Figure 3.13 Decomposition of NO ₂ synergistic adsorption on γ -Al ₂ O ₃ (111) supported (BaO) ₂	58
Figure 3.14 Top view of NO ₂ adsorption over the γ -Al ₂ O ₃ supported (BaO) ₂ in small and big unit cells	59
Figure 3.15 PDOS of Al and O atoms in NO ₂ adsorption on supported (BaO) ₂	60
Figure 4.1 Energy diagram of H ₂ dissociative adsorption over Mg ₉ , Mg ₉ ²⁺ , Mg ₉ ²⁻ , Mg ₁₀ and Mg ₁₀ ²⁺ clusters	69
Figure 4.2 Activation energy vs. band gap difference between the transition state and the corresponding reactant cluster/surface.....	77
Figure 4.3 Transition states of hydrogen dissociation over the Mg(100) and (110) surfaces	78
Figure 5.1 Top and side views of ZrO ₂ (111) and γ -Al ₂ O ₃ (100) surface slabs	85
Figure 5.2 Optimized structures of Ce ₂ O ₄ cluster supported on the ZrO ₂ (111) and γ -Al ₂ O ₃ (100) surfaces, and optimized structure of the unsupported Ce ₂ O ₄ cluster.....	90
Figure 5.3 CO ₂ adsorption on ZrO ₂ (111) supported and γ -Al ₂ O ₃ (100) supported Ce ₂ O ₄ cluster.....	91
Figure 5.4 CO adsorption on Ce atom of ZrO ₂ (111) supported and γ -Al ₂ O ₃ (100) supported Ce ₂ O ₄ cluster.....	93
Figure 5.5 Carbonate-like structure formed on ZrO ₂ (111) supported and γ -Al ₂ O ₃ (100) supported Ce ₂ O ₄ cluster upon reactive adsorption of CO	95
Figure 5.6 PDOS of the Ce atoms in the supported Ce ₂ O ₄ before and after CO reactive adsorption.....	99

Figure 5.7 Potential energy profiles of CO oxidation on unsupported, $\text{ZrO}_2(111)$ and $\gamma\text{-Al}_2\text{O}_3(100)$ supported Ce_2O_4 cluster, and $\text{CeO}_2(100)$ surface102

LIST OF EQUATIONS

<u>EQUATION</u>	<u>PAGE</u>
Equation 2.1 Planck's Description of Discrete Energies	5
Equation 2.2 Wavelength of Particles.....	5
Equation 2.3 Time-dependent Schrödinger Equation.....	6
Equation 2.4 Time-independent Schrödinger Equation.....	6
Equation 2.5 Electronic Density Equation.....	8
Equation 2.6 Effective Potential in Homogeneous Gas.....	8
Equation 2.7 Thomas-Fermi's Energy Equation	8
Equation 2.8 Hohenberg-Kohn Ground State Energy Equation	10
Equation 2.9 Hohenberg-Kohn Theory Kinetic Energy Equation.....	10
Equation 2.10 Hohenberg-Kohn Theory Coulumb Energy Equation.....	10
Equation 2.11 Kohn-Sham Energy Equation.....	10
Equation 2.12 Definition of Electron Density in Kohn-Sham Equation	11
Equation 2.13 Kinetic Energy in terms of Wavefunction.....	11
Equation 2.14 Orthonormality	11
Equation 2.15 Schrödinger's Equation of Non-interacting Particles.....	11
Equation 2.16 Effective Energy in Equation 2.15	11
Equation 2.17 Exchange-correlation Potential	11
Equation 2.18 Kohn-Sham Energy Equation in terms of Single Particle Wavefunction	13
Equation 2.19 LDA Exchange-Correlation Energy	13
Equation 2.20 LDA Exchange Energy.....	13
Equation 2.21 LDA Correlation Energy	13

Equation 2.22	GGA Exchange-Correlation Energy.....	13
Equation 2.23	B3LYP Functional.....	14
Equation 2.24	Time-Dependent Hamiltonian.....	16
Equation 2.25	Time-Independent Hamiltonian.....	16
Equation 2.26	Coulomb Integral.....	16
Equation 2.27	Exchange Integral.....	16
Equation 2.28	Arrhenius Equation.....	18
Equation 2.29	Eyring Equation.....	18
Equation 3.1	Calculation of Adsorption Energy.....	37
Equation 3.2	Calculation of Binding Energy.....	53
Equation 4.1	Calculation of Activation Energy.....	71
Equation 5.1	Calculation of Binding Energy.....	89
Equation 5.2	Calculation of Adsorption Energy on Supported Cluster.....	95
Equation 5.3	Calculation of Adsorption Energy on Unsupported Cluster.....	96
Equation 5.4	Calculation of Interaction Energy.....	97
Equation 5.5	Relationship between Adsorption Energies and Interaction Energy....	97

LIST OF SCHEMES

<u>SCHEME</u>	<u>PAGE</u>
Scheme 5.1 Thermodynamic cycle of CO reactive adsorption on the supported Ce ₂ O ₄ cluster.....	96

CHAPTER 1

GENERAL INTRODUCTION AND OUTLINE

Heterogeneous catalysis plays a vital role in many industrial operations and many other processes. These processes include oil refining¹, production of fertilizers, as well as eliminating the pollution from chemical and petroleum processes, and vehicular emissions.² The advancement of fuel-cell technologies also rely on the development of more efficient catalysts at both electrodes³. Heterogeneous catalysis is a type of catalysis process where the catalyst is in a different phase from the reactant. Normally the catalyst is a solid and the reactants are gas or liquid. The catalytic process usually proceeds by the chemisorption of the reactants to the catalyst surfaces, and the strength and characteristic of the chemisorption determine the performance of the catalyst. Therefore, gaining the knowledge of the catalyst performance as a function of the chemical composition and molecular structure of the catalyst surface or nanocluster is the science foundation for heterogeneous catalysis.

The state-of-the-art modern experimental approaches provided useful tools for the study of this field. For example, low energy electron diffraction (LEED) is widely used to characterize the structure of the surfaces⁴⁻⁶. The yet more powerful scanning tunneling microscopy (STM)⁷⁻⁹ and atomic force microscopy (AFM)^{10,11} allow the viewing the surface at the atomic level. Vibrational frequencies from high resolution electron energy loss spectroscopy (HREELS) or reflection adsorption infrared spectroscopy (RAIRS) are used to characterize the adsorbed reactive molecules on the surfaces. The measurement adsorption and reactivity from temperature programmed desorption (TPD) and temperature programmed reaction (TPR) experiments provides quantitative information

on the elementary adsorption and reaction steps that occur on these model surfaces. In addition, the technique of synthesizing metal clusters on well-defined thin oxide films¹²⁻¹⁸ enables the more controlled preparation of catalysts. With these carefully prepared samples, some atomic details of the catalysts were revealed and conditions affecting the performance of catalysts were well understood.

Despite the valuable information we can obtain from the experiments, there are also phenomenon and insights into the system hitherto unobservable using pure experimental approaches. For example, some experimental approaches merely reveal the average behavior of a system, while the contribution of distinct localized domains/structures cannot be measured. Furthermore, some experimental data are hard to be interpreted due to the complexity of the system and the coupling of multiple interactions. For example, the information of molecular bonding and orbital and electronic charge distributions cannot be obtained from experiments. The strength of interactions and the relative stabilities between different structures cannot be predicted by experiments. The information of a complete reaction pathway cannot be described by any experimental approach. Therefore, an approach beyond experiment is needed to predict the unobservable properties and improve the interpretation of the experimental data.

Quantum mechanics methods can be used to solve some of the problems that experimental approaches failed. By applying different theoretical methods, most of the molecular behavior can be predicted. For example, the structures and the relative energies of a molecule or solid can be calculated to obtain the knowledge of stable atomic structures of a system. The frequency calculations of each individual mode can be used to assign the peaks from experimentally obtained spectrum. Some methods based on

transition state theory can discover the complete reaction pathways, calculating the transition state structures and also determine which of the pathways is more favorable for the reaction. Depending on the quantum theory being used, there are several types of computational methods: ab initio method, semi-empirical/empirical method, molecular mechanics and molecular dynamics. Here we consider the density functional theory (DFT) belong to ab initio category since the molecular Hamiltonian needs to be solved although some of the functionals employ parameters derived from empirical data.

In this dissertation, a brief review of the DFT and its implementation in computational packages are present in Chapter 2. The transition state theory applied in my work is also briefly discussed in this chapter. Chapter 3–5 presents my study of the properties that influence the activities of catalysts: geometric and electronic structures of a catalyst, defect and substrate effect. Chapter 3 presents how the morphologies of BaO surfaces and clusters, as well as the existence of defects and support substrate, affect the BaO-NO₂ interaction. Chapter 4 reports the influence of the electronic structures of magnesium clusters on the energy barriers of magnesium-catalyzed H₂ dissociation. The effect of the nature of the support substrate on the reactivities of the supported metal oxide was studied in Chapter 5. The reactivities of monoclinic ZrO₂(111) and non-spinel γ -Al₂O₃(100) supported Ce₂O₄ clusters toward CO and CO₂ adsorption were compared to reveal the different support effects.

CHAPTER 2

COMPUTATIONAL METHOD

2.1. A Brief History of Quantum Mechanics

Toward the end of the nineteenth century, thanks to the work of the great physicists, most important principles of the classical physics have been discovered and brought to a high degree of sophistication¹⁹. The turn of 20th century is a heady era of great success for a more profound discoveries and revolution that impact the science field of physics, chemistry and biology, as well as engineer and technologies. This revolution starts with the birth of the theory of relativity and quantum mechanics and these two constitute what now is called modern physics. Modern physics completely altered our way to look at the world. Quantum mechanics was initially developed to provide a better explanation of the behavior of systems at atomic length scales and smaller, especially the spectra of light emitted by different atomic species. After several decades of development, quantum mechanics nowadays not only plays a very important role in the field of physics, but also has its many applications in chemistry.

In early 1838, Michael Faraday discovered the “cathode rays” when passing current through a rarefied air filled glass tube. These cathode rays are actually streams of electrons. In 1897, the British physicist Joseph John Thomson performed an early version of the famous oil drop experiment of Millikan and calculated the charge and mass of the electron. Although his calculations of charge and mass were in error by 50%, the experiment did show that there exists a subatomic particle much lighter than the lightest atom. After Gustav Kirchhoff’s study of the black body radiation problem in 1859, Ludwig Boltzmann suggested in 1877 that the energy states of a physical system could be

discrete. Finally in 1900, Germany physicist Max Planck successful proposed a mathematical formula for the discrete energies of the black body:

$$\varepsilon = nh\nu, \quad (2.1)$$

where n is an integer, h is a constant and ν is the frequency. However, Planck's theory was too revolutionary to be accepted by most physicists at the time. A few years later, in 1905, Einstein explained the photoelectric effect using the very same idea of Planck's and obtained a value of h in close agreement with Planck's value. In 1907, he further proved that the mechanical vibrations of the atoms in crystals are also quantized. Ever since then, the idea of quantization condition became provocative. In effort of explaining the line spectrum of hydrogen, Niels Bohr formulated a model of hydrogen atom that was in good accordance with the spectrum. However, Bohr's theory could not be successfully extended to explain some phenomenas such as the spectrum arising under a magnetic field. The stage for the next advance was set by de Broglie, who, in 1923, postulated that electrons and other particles have waves associated with them and the wavelength is given by

$$\lambda = h/p, \quad (2.2)$$

where p is the momentum of the particle. Combining this wave nature of particles with Bohr's theory, the quantization of Bohr orbitals can be explained by whether the wave is in phase of the orbital. In 1926, the electron was experimentally shown to act like wave for the first time by George Paget Thomson, J. J. Thomason's son. Following the discovery of both particle-like and wave-like properties of atomic and subatomic particles, Schrödinger found a wave equation that governs the behavior of those particles in 1926²⁰.

The Schrödinger's equation is a very fundamental equation in quantum mechanics. The solution of this equation is called wavefunction. It is the most complete description of any system. The general equation for one particle can be written as:

$$i\hbar \frac{\partial}{\partial t} \Psi(r, t) = \hat{H} \Psi(r, t) = -\frac{\hbar^2}{2m} \nabla^2 \Psi(r, t) + V(r) \Psi(r, t), \quad (2.3)$$

where $\Psi(r, t)$ is the wavefunction, r is the position in three-dimensional space, \hat{H} is the Hamiltonian operator, m is the mass and $V(r)$ is the potential at point r . The time-independent Schrödinger's equation can be written as:

$$E\psi(r) = -\frac{\hbar^2}{2m} \nabla^2 \psi(r) + V(r)\psi(r), \quad (2.4)$$

which formulated the Schrödinger's equation as an eigenvalue problem.

Shortly after Schrödinger's equation for the electronic wavefunction was validated for simple small systems like H_2 and many-electron atom He, there was a saying that chemistry had come to an end because all the chemistry can be entirely contained in the powerful equation. However, in most of the cases, the quantum mechanical equation is way too complicated to be solved exactly, so finding proper approximation to Schrödinger's equation became an intuitive and straightforward solution. As matter of fact, during the decades after Schrodinger's equation, the entire field of computational chemistry is built around approximate solutions. Some of these solutions are very crude and others are expected to be more accurate than any experiment that has yet been conducted. The knowledge of each approximation and how accurate the results are expected to be the key to the choice of method. Extremely powerful computers, sometimes supercomputers, are needed for obtaining very accurate results. Generally, the larger the system is (containing more particles), the more expensive the computation is.

2.2. Density Functional Theory

Density Functional Theory (DFT) method uses the electron density of a system to provide us the properties of the ground states. It was first introduced in 1960s by Hohenberg-Kohn²¹ and Kohn-Sham in two of the seminar papers^{21,22}. Later, the theory has attracted a lot of research interest in improving the adaption of the method for practical computational use. The last few decades have witnessed the prevailing applications of DFT method—especially after 90s, the usage of the method has increased exponentially. It is so far the most successful and most promising approach to compute the electronic structure of the matter. It also calculates a large variety of molecular properties such as molecular structures and energies, vibrational frequencies, electric and magnetic properties and reaction pathways, etc. It is among the most popular methods available in condensed matter physics, computational physics, and computational chemistry... Nowadays, it is often referred to as “theory of the moment”. In 1998, Walter Kohn was awarded with the Nobel Prize in Chemistry for his contributions to the “development of the density functional theory”, symbolizing the recognition of the contribution of the theory to physics and chemistry science societies.

There are three important benchmark works in DFT development history: First, the rudimentary but inspirational form of DFT that was discussed in 1927 by Thomas and Fermi, known as Thomas-Fermi theory. In 1964 and 1965, the Thomas-Fermi theory was put forward in two seminar papers, known as Hohenberg-Kohn theory and Kohn-Sham equation. These three benchmarks will be introduced below:

2.2.1. Thomas-Fermi Theory

The Thomas-Fermi theory first introduced electron density instead of wavefunction as the variable to quantum equations. The theory considered interacting electrons moving in

an external potential field and it has a very crude description of electronic energy in terms of the electron density distribution $n(r)$:

$$n(r) = \gamma(\mu - v_{\text{eff}}(r))^{3/2}, \quad (2.5)$$

where

$$v_{\text{eff}}(r) = v(r) + \int \frac{n(r')}{|r-r'|} dr'. \quad (2.6)$$

μ in Equation (2.5) is the coordinate-independent chemical potential and r is a constant. Equation (2.6) calculates the difference between external potential (the first term) and the electrostatic energy that is generated by the electron density distribution $n(r)$ (the second term). The number of electrons within a small enough distance element dr is homogeneous and can be expressed as $n(r)dr$. So the energy of the system can be calculated by:

$$E_{TF}[n(r)] = \int \frac{3}{10} (3\pi^2)^{2/3} n(r)^{5/3} dr + \int v(r)n(r)dr + \frac{1}{2} \int \frac{n(r)n(r')}{|r-r'|} drdr', \quad (2.7)$$

where the first term is the electronic kinetic energy calculated by integrating the kinetic energy density of homogeneous electron gas.

One big breakthrough of the Thomas-Fermi theory is it provided a crude form of expressing the solution of the many-electron Schrodinger's equation in terms of electron density $n(r)$ instead of in terms of wavefunction ψ , so we can characterize the electronic structure of the system by knowing the electron density $n(r)$. However, Equation (2.5) was based on the expression of a uniform electron gas distribution under the external potential, so the theory suffers many deficiencies. First, the gradients of $v_{\text{eff}}(r)$ were obviously ignored. Therefore, the theory only applies for systems with slowly varying density. Second, the description of kinetic energy is very crude. While the kinetic energy represents a substantial portion of the total energy of a system so the small error of

kinetic energy description for each point can lead to disastrous results. So it is only good in describing the qualitative trends of energies. Third, the electron-electron interaction is over-simplified. These interactions were treated classically so a lot of the quantum phenomenon was not taken account of. The theory totally fails to calculate chemical bonding^{23,24}. Although later on, the gradient, exchange and correlation were made to improve the method, it was generally considered too rough to be useful for the applications of electoral structure calculation.

2.2.2. Hohenberg-Kohn Theory

Uniqueness: The first important lemma of the Hohenberg-Kohn theory is the proof of “the ground state density $n(r)$ of a bound system of interacting electrons in some external potential $v(r)$ determines this potential uniquely”. The proof of this lemma was simply assuming an electron density $n(r)$, corresponds to two non-degenerate ground state potentials $v_1(r)$ and $v_2(r)$ with ground state wavefunction of ψ_1 and ψ_2 . However, the ground state energy E_1 and E_2 calculated from the two different potential and wavefunction but the same electron density yielded $E_1 + E_2 < E_1 + E_2$, contradicting with the assumption that two states are non-degenerate.²¹ Therefore, the ground state can be uniquely determined by the ground state electron density $n_0(r)$.

Variational Theory: The variational theory, which is very useful to a lot of quantum method, stated that the expectation value of the Hamiltonian for a trial wavefunction must be greater than or equal to the actual ground state energy. Based on the uniqueness theorem, the ground state energy can be solved if the groundstate electron density $n_0(r)$ is known. So adding the Variational Theory on top of it, the ground state energy can be solved by minimizing the energy in terms of electron density $n(r)$. The energy can be

written as a summation of kinetic energy, electrostatic energy and the energy of non-interacting electron moving under external potential:

$$E_{[n(r)]} = T_{[n(r)]} + U_{[n(r)]} + \int V(\vec{r})n(\vec{r})d^3r, \quad (2.8)$$

where the first two terms are independent of external potential $V(r)$ and can be expressed using a universal functional of the electron density $n(r)$:

$$T = \int \frac{3}{10} [3\pi^2 n(r)]^{\frac{2}{3}} n(r) dr \quad (2.9)$$

$$U = \frac{1}{2} \int \frac{n(r)}{|r-r'|} dr' dr \quad (2.10)$$

So, the Hohenberg-Kohn Theory provided a form of calculating energy in terms of electron density. But the method is not accurate due to the inadequate representation of the kinetic energy T .

2.2.3. Kohn-Sham Equations

Following the Hohenberg-Kohn theorem, the Kohn-Shaw theorem stated that if we can find the true ground state electron density, we find the lowest energy of the system and thus the ground state of the system. Furthermore, the theorem provided a way of finding the ground state density. Kohn and Sham proposed the ground state energy can be written as a functional of the charge density:

$$E_{[n(r)]} = T_{[n(r)]} + E_{\text{ext}[n(r)]} + 1/2 \int \frac{n(r)n(r')}{|r-r'|} + v_{\text{xc}[n(r)]}, \quad (2.11)$$

where the first term is the kinetics energy and the second term is the interaction between electron and the external potential. The third and fourth terms are electron-electron electrostatic interaction and the non-classical exchange-correlation energy, respectively. The last two terms combined describe the electron-electron interaction. Inspired by the self-consistent single particle equations for the approximation of the electronic structure

by Hartree^{25,26} where every electron was regarded as moving in an effective single particle potential, Kohn and Sham then reintroduced the single particle wavefunctions:

$$n(r) = \sum_{i=1}^n \psi_i^*(r)\psi_i(r). \quad (2.12)$$

The kinetic energy can be written in terms of wavefunctions by:

$$T[n(r)] = -\frac{\hbar^2}{2m} \sum_{i=1}^n \langle \psi_i | \nabla^2 | \psi_i \rangle. \quad (2.13)$$

Equation

$$\int \psi_i^*(r)\psi_j(r)dr = \delta_{i,j} \quad (2.14)$$

guarantees the orthonormality of the wavefunctions. These wavefunctions are the solutions to the Schrödinger's equation of non-interacting particles moving in an effective potential $v_{eff}(r)$:

$$-\frac{\hbar^2}{2m} \nabla^2 \psi_i(r) + v_{eff}(r)\psi_i(r) = \epsilon_i \psi_i(r), \quad (2.15)$$

where

$$v_{eff}(r) = v_{ext}(r) + v_{xc}(r) + \frac{1}{2} \int \frac{n(r')}{|r-r'|} dr'. \quad (2.16)$$

The exchange-correlation potential is given by:

$$v_{xc}(r) = \frac{\delta E_{xc}[n(r)]}{\delta n(r)}. \quad (2.17)$$

So the energy of the system can be written as:

$$E_{[n]} = \sum_{i=1}^n \epsilon_i - 1/2 \int \frac{n(r)}{|r-r'|} + E_{xc}[n(r)] - \int \frac{\delta E_{xc}[n(r)]}{\delta n(r)} n(r) dr, \quad (2.18)$$

where ϵ_i s are the eigenvalues of non-interacting single-particle equation which is supposed to be an "exact" term.

Now the attention turned into the exact form of the exchange-correlation functional. Actually, this term is so important that the practical use of the ground state DFT entirely

depends on the accuracy of this approximation term. The discussion of the exchange-correlation term will be presented in the following section.

2.2.4. Functional Effect

This exchange-correlation term is, in my opinion, the beauty of DFT because we do not need to deal with the electron exchange and correlation term explicitly any more. In Hartree-Fock method, the electron correlation energy was ignored and the electron exchange term has to be treated by solving the mixed wavefunction terms of different electrons. Sometimes these crossing terms from the electron exchange can be really “nasty” and solving them cost a lot of computational effort. While in DFT, not only was the electron correlation calculated, it was treated along with the exchange term which makes the calculation a lot easier. The idea of treating electron exchange and correlation together is great, however, the exact form of this term is unknown. Therefore, like lots of the other quantum theories, approximations were made to express this term.

As discussed above, finding a good approximation of the exchange-correlation functional is critical for the proper application of DFT. As a matter of fact, after the appearance of the Kohn-Sham equation, a lot of research effort has been focused on developing an accurate approximation functional which, at the same time, sufficiently simple to be solved. There are three categories of exchange-correlation functional—the local density approximation (LDA), general gradient approximation (GGA) and hybrid functional.

The LDA functional is the simplest approximation for the $E_{\text{ex}(n)}$. The exchange-correlation term can be approximated to the energies of a homogeneous electron gas of the same local density:

$$E_{\text{ex}(n)} = \int e_{\text{xc}}(n(r))n(r) dr \quad (2.19)$$

where the $e_{\text{xc}}(n)$ is the exchange-correlation energy of a uniform electron gas of density n . The exchange part is given by

$$e_{\text{x}}(n) = -\frac{0.458}{r_{\text{s}}}, \quad (2.20)$$

where r_{s} is the radius of a sphere containing one electron. The correlation part was first estimated by Wingner²⁷:

$$e_{\text{c}}(n) = -\frac{0.44}{r_{\text{s}}+7.8}, \quad (2.21)$$

reflecting the combined effect of the Pauli principle and the electron-electron interaction.

The accuracy of the exchange energy for the LDA form is typically within 10%, while the correlation energy, which is normally much smaller, is generally overestimated by up to a factor 2. Fortunately, the two errors typically cancel each other partially. Thus, the LDA gives ionization energies of atoms, dissociation energies of molecules and cohesive energies with a fair accuracy of typically 10-20%, while the bond lengths of molecules and solids are typically decent with an accuracy of 2%. However, the LDA calculations are insufficient for most applications in chemistry, especially when it comes to systems like heavy fermions, where the electron-electron interaction effect dominates.

The GGA is an improved form based on the LDA functional by including the gradient expansion term:

$$E_{\text{ex}(n)} = \int e_{\text{xc}}(n(r), |\partial n(r)|)n(r) dr. \quad (2.22)$$

Furthermore, some of the GGA methods that were developed in recent years often have been empirically calibrated to optimize the accuracy of the atomization energies of standard sets of molecules and have really successfully produced the structural and

energetic properties of various systems. Major contributors include A.D. Becke, D.C. Langreth, M. Levy, R.G. Parr, J.P. Perdew, C. Lee and W. Yang.²⁸ Examples of commonly used GGAs are PW91 and PBE.

Another successful functional was introduced is the hybrid method which incorporates linear combination of exact exchange from Hartree-Fock theory with exchange-correlation from other sources. The idea was first introduced by Axel Becke in 1993.²⁹ For example, the famous B3LYP^{30,31} functional is written as:

$$E_{xc}^{B3LYP} = E_{xc}^{LDA} + \alpha_0(E_x^{KS} - E_x^{LDA}) + \alpha_x(E_x^{GGA} - E_x^{LDA}) + \alpha_c(E_c^{GGA} - E_c^{LDA}), \quad (2.23)$$

where the values of the three parameters α_0 , α_x and α_c are determined by fitting the predicted values to a set of experimental data such as atomization energies and ionization energies etc.

GGA's and hybrid approximations have reduced the LDA errors of atomization energies of standard set of small molecules by a factor 3-5. This improved accuracy has made DFT nowadays a very important and popular computational method of quantum chemistry. The hybrid functional can even deal with some problems that cannot be achieved by the LDAs and GGAs such as the highly localized f electrons in transition metals.

2.2.5. Overview of Theory

2.2.5.1. Major Contributions of Theory

Fundamental Understanding (DFT v.s. Hartree-Fock): Following Schrödinger's equation, traditionally, we consider a system as Hilbert space of single particle orbitals and the wavefunctions are the most important variables for a system. While the DFT

provided a complimentary perspective by focusing on quantities in real coordinate space $n(\mathbf{r})$, so this is conceptually a totally different point of view. In addition, the exchange-correlation energies were included in DFT and they were cleverly written together using an exchange and approximated functional.

Practical: Another success of the DFT is it is actually a very practical method for the study of quantum system. In quantum computations, Hartree-Fock method is a basic method that provides a “reasonable” physical description of the interactions such as attractions, repulsions and electron exchanges between nucleus and electrons of a system. However, the method has its limitation: by increasing the complexity of the basis set in the calculation, the convergence eventually reaches to the “exact” solution of the Hartree-Fock calculation and this is called Hartree-Fock limit. Unfortunately, the limit is still far from the exact description of many electronic structures and properties simply due to the ignorance of the electron correlation term. For example, Hartree-Fock calculations yield poor results for the dissociation energies and even worse results for the reaction energies. DFT, along with others such as perturbation theory (MP2, MP3 and MP4 calculations), configuration interaction method and coupled-cluster method are considered “beyond Hartree-Fock” approaches. These “beyond Hartree-Fock” methods provide more accurate computational results by including the correlation energies. However, except the DFT, all the other “beyond Hartree-Fock” methods all suffer a big drawback: if we use traditional wavefunction methods, when the system size increases, at certain point, we encounter a so called “exponential wall”—as the particle number increases, the computational effort increases exponentially. While the computational effort of DFT is significantly lowered, thus the computation of large systems became achievable. The

“practical” success can be explained by showing the difficulties of solving traditional Hartree-Fock in terms of wavefunction below:

The original Hamiltonian is written as:

$$\hat{H} = -\frac{\hbar^2}{2m} \sum_{i=1}^n \nabla^2 - \frac{\hbar^2}{2m_a} \sum_{a=1}^m \nabla^2 - \sum_{i=1}^n \sum_{a=1}^m \frac{Z_a}{r_{ia}} + \sum_{i=1}^n \sum_{j>1}^n \frac{1}{r_{ij}} + \sum_{ia=1}^m \sum_{b>a}^m \frac{Z_a Z_b}{R_{ab}} \quad (2.24)$$

After the first “famous” approximation, that is, Born-Oppenheimer approximation, the electronic Hamiltonian can be written as:

$$\hat{H}_{elec} = -\frac{\hbar^2}{2m} \sum_{i=1}^n \nabla^2 - \sum_{i=1}^n \sum_{a=1}^m \frac{Z_a}{r_{ia}} + \sum_{i=1}^n \sum_{j>1}^n \frac{1}{r_{ij}}, \quad (2.25)$$

where there are only three terms left—the electron kinetics, the nuclei-electron attractions and the electron-electron repulsions. The first and second terms in Equation 2.25 are usually very straightforward and easy to deal with, but the electron-electron interaction is often cumbersome. The Hartree-Fock method describe the electron-electron interaction using $\sum_{i,j=1}^n J_{ij} - K_{ij}$ where

$$J_{ij} = \int \int \psi_i(\vec{x}_1) \psi_i^*(\vec{x}_1) \frac{1}{r_{12}} \psi_j(\vec{x}_2) \psi_j^*(\vec{x}_2) d\vec{x}_1 d\vec{x}_2 \quad (2.26)$$

$$K_{ij} = \int \int \psi_i^*(\vec{x}_1) \psi_j(\vec{x}_1) \frac{1}{r_{12}} \psi_i(\vec{x}_2) \psi_j^*(\vec{x}_2) d\vec{x}_1 d\vec{x}_2. \quad (2.27)$$

J_{ij} is Coulomb integrals, and K_{ij} is exchange integrals which covers the electron exchange energy. It was the last exchange term of the Hartree-Fock model that made the Hartree-Fock equation not “separable” for each electron, and furthermore, solving equations with this mixed term can be really “painful”. One of the reasons why DFT method is so efficient compared with the Hartree-Fock method is it avoids dealing with this term. Instead, only the Schrödinger’s equations of single particles need to be solved.

2.2.5.2 Applications

DFT has been successfully applied to calculate various ground state properties of a lot of different systems. Theoretically, any property that can be derived by solving Schrödinger's equation can be calculated by the DFT. Those properties typically include: mechanical properties (elasticity and plasticity), phonons and thermodynamics, theoretical crystallography and mineralogy. It can also deal with some chemical processes such as heterogeneous catalysis (oxidation and hydrogenation), hydrodesulfurization and isomerization cracking, as well as electrochemistry and electrocatalysis. Furthermore, the time-dependent density functional theory (TD-DFT)³² is the extension of DFT method and can be used to calculate the excited state properties such as excitation energy and photoadsorption spectrum. The DFT method can also be conveniently implemented into ab initio Car-Parronello molecular dynamics simulations³³ wherein the electronic degree of freedom is included.

Other techniques to improve the applications of DFT include: using high-performance code (MPI-based code, for example), good choice of basis set (planewave for extended system, Pseudopotentials rather than full-electron methods) and tight-binding techniques (semi-empirical).

DFT still have unsolved issues of dealing with certain systems and properties. Because the DFT calculations are very sensitive to the electron density and thus it fails for systems where electron density is not a slowly varying function such as Van der Waals energies between non-overlapping subsystems and electronic tails evanescent into the vacuum near the surfaces of bounded electronic systems and electronic Wigner crystal. The poorly calculated properties also include long range polarization energies, regions of evanescent electron densities, partially filled electron shells and reaction

barriers. Only through proper special approximations, these problems can be successfully treated.

2.3. Locating Transition States

Before the development of transition state theory (TST), the empiricism-based Arrhenius equation

$$\kappa = Ae^{-E/RT} \quad (2.28)$$

is generally accepted³⁴. However, the equation is based the experimental observation and does not have theoretical or mechanism base. The detailed consideration of the pre-factor A and the activation energy E was not dealt with until 1935 when the TST was discussed by Henry Eyring and by Gwynne Evans and Michael Polanyi simultaneously.³⁵⁻³⁷ The Eyring equation, also known as the Eyring-Polanyi equation

$$\kappa = \frac{k_B T}{h} e^{-\Delta G^\ddagger/RT} \quad (2.29)$$

successfully addressed the two factors (pre-factor and activation energy) in the Arrhenius equation. The fundamental assumption is that there exists a hypersurface in phase space which divides space into a reactant region and a product region, and once the trajectory passes through this dividing surface to the product direction it will never recross the hypersurface again. Thus, the reaction rate can be calculated by focusing attention on the activated complex which lies at the saddle point of the potential energy surface and the details before the transition state is reached is not important. A more refined version of transition state theory is the variational transition state theory (VTST)^{38,39}. It is distinguished from the conventional TST by varying the definition of the dividing surface. The dividing surface does not only intersect the saddle point, it is also perpendicular to the reaction coordinate in all reaction coordinate dimensions. Thus, the

dividing surface between reactant and product regions is variationally optimized to minimize the reaction rate. Some recent development of the original TST include RRKM theory⁴⁰⁻⁴² and quasi-equilibrium theory (QET)⁴³ etc.

In my study, the Nudged Elastic Band (NEB) method^{44,45} was used to seek the minimum energy pathway (MEP) and locate the saddle point of the MEP. The NEB method was developed by Hannes Jonsson et al. The method is a very efficient approach for finding MEP between given initial and final state even for systems with very complex potential energy surfaces. In the NEB method, first a set of images (replicas) of the system are constructed between initial and final states. Then a spring interaction is added to between adjacent replicas so that the images on the path are continuous. The spring force limits any irrational movement of the images that would not end up with the transition state and the system now mimics an elastic band. Figure 2.1 shows the potential energy surface of a reaction that involves three atoms a, b and c. Atom b either binds with a or c. At point AB, compound ab forms

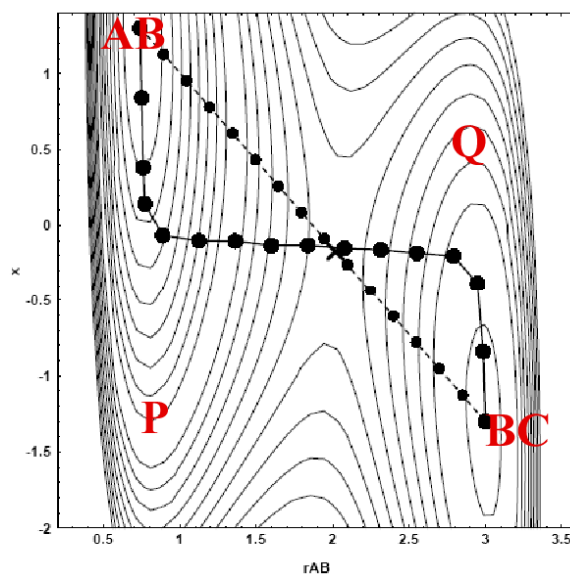


Figure 2.1. A contour plot of potential energy surface for a three-atom system.

and at point BC compound bc forms and these two points are both energy minimum on the plot. The points at the straight line with small dots which connect to initial and final state AB and BC represent the set of images constructed at the beginning of a NEB calculation. If the spring force didn't exist between the images, optimizing the images at the straight line would lead to the images on the right hand side of the system falling into region Q and those on the left into P at the end, which obviously would not lead to a transition state. However, minimizing the force acting on the images with the spring force, we end up with the MEP which is indicated by the line with large dots. To be more specific, the tangent to the path at each image during the minimization was calculated so that both spring force and true force can be decomposed into components parallel or perpendicular to the path. Only the parallel spring force and the perpendicular real force should be included in minimization. This ensures that the spring forces only controls the spacing between the images along the band but do not interfere with the convergence of the elastic band to the MEP (the perpendicular spring force prevent the band from following a curved pathway causing "corner-cutting"); at the same time, the true force pushes the images into the MEP but does not affect the distribution of images along the band (the parallel true force causes the images to slide away from the high energy regions towards the minima, reducing the density of images where they are needed most).

The NEB has been conveniently adapted for conjunction use with the DFT calculation code VASP. In my study, I used the *Perl* code developed by Henkelman et al.⁴⁵

2.4. Computational Codes

The density functional theory has been implemented in various computational codes. Two simulation codes were used in my study—the VASP and GAUSSIAN. Both codes are very well commercialized and widely used.

2.4.1. VASP. The Vienna Ab-initio Simulation Package (VASP) performs *ab-initio* density functional theory calculations. It is by far one of the most popular computational codes for calculations of infinite systems such as solid states and condensed matters.

VASP uses plane wave basis set rather than localized basis set. The PAW method or ultra-soft pseudopotentials are used to describe the interaction between ion and non-valence electron so that the size of the basis set can be reduced. The self-consistency cycles and choices of numerical methods to calculate the electronic Kohn-Sham ground-state in VASP are quite efficient and robust. Periodic boundary conditions are used to treat infinite numbers of atoms. The package also includes the Monkhorst Pack to sample the Brillouin zone. In the actual computation, only the atoms within one periodic cell was optimized and computed with the consideration of their interactions with atoms in the neighboring cells. For example, a CeO₂ bulk structure is shown in Figure 2.2. The system is infinite, but in the actual calculation, only atoms in the highlighted unit cell is computed, however, when calculating the atoms in the highlighted unit cell, their interactions with the atoms in neighboring cells are also considered.

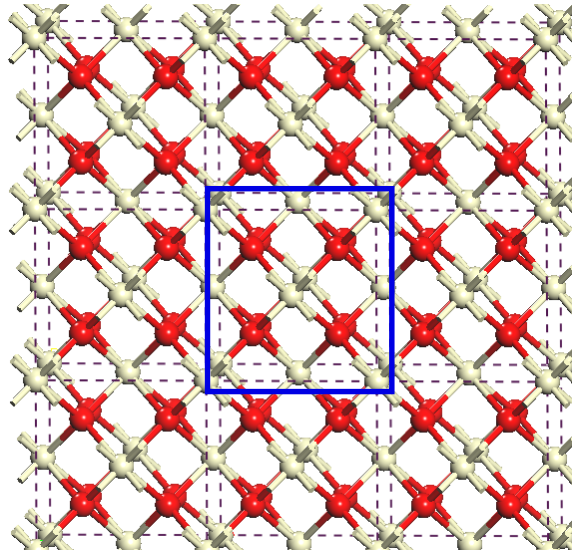


Figure 2.2. Bulk CeO₂ structure. Atoms in each box are repeated in other boxes.

The VASP offers support for a large variety of platforms, such as Pentium, Athlon, IBM, HP, Cray and SUN(-). High performance computation (paralleled computers) is available. All these features make the package very suitable for computations of extended large systems. In principle, in paralleled computing the more processors are used, the faster the calculation is. However, for the computer clusters, depending on the processor type, there is always a critical number of CPUs, larger than which the computation speed does not increase linearly with the number of CPUs used—for example, computing on four nodes might be two times faster than computing on two nodes, but computing on eight nodes does not necessarily improve the efficiency by as much as four times.

A typical VASP calculation requires at least four basic input files—INCAR, POTCAR, POSCAR and KPOINTS.

INCAR: The actual calculation control parameters are included in this file. It decides what calculations need to be done and how they should be done. The basic parameters are as following:

IBRION = 2 *Ionic relaxation algorithm: 0-MD 1-quasi-New 2-Conjugated Gradient.*

POTIM	=	0.50	<i>Time-step for ion-motion. The proper value can speed up the calculation</i>
ISIF	=	2	<i>What to relax. Typically 7- bulk, 2-cluster, and 3 or 2 for surface.</i>
NSW	=	100	<i>Number of steps for ionic relaxation. Stopping criteria before EDIFFG is reached.</i>
EDIFF	=	.5E-04	<i>Stopping-criterion for electronic self consistent loop.</i>
EDIFFG	=	.5E-03	<i>Stopping-criterion for ionic relaxation. Typically ten times of the value of EDIFF.</i>
ISPIN	=	1	<i>Spin state. 1-unpolarized 2-polarized. Different setup will yield different energy value.</i>
ENCUT	=	450.0	<i>Cut-off energy. Directly affects the accuracy of the calculation and the calculated absolute energy value.</i>

The parameters listed above are the basic important parameters for an INCAR file. One should try to keep all the parameters as consistent as possible within one system for the comparison reason, i.e., all the calculations should have the same accuracy to be compared with each other.

Additional parameters:

PREC	=	high	<i>Precision of the calculation. "High" will change cut-off energy.</i>
LCHARG	=	T	<i>Whether to write CHGCAR.</i>
LWAVE	=	T	<i>Whether to write WAVECAR. CHGCAR and WAVECAR take a lot of disk space. Unless necessary, don't write them out.</i>
LORBIT	=	12	<i>Whether to write DOSCAR and in what format.</i>

POTCAR: The VASP is supplied with a set of standard pseudopotentials of various atoms. Before starting a calculation, one should have the pseudopotentials of each atom involved in the system concatenated in POTCAR under the working directory.

POSCAR: This file contains the lattice geometry and the ionic positions. For MD calculations, it also optionally contains the starting velocities. For VASP calculations, the system of interest is always a “box”, so the shape and size of the box should be defined in this file. The number of each type of atoms should be written in one line according to the order the element appears in the POTCAR file. Then the coordinates of each atom should be listed either in Direct or Cartesian coordinate. One can also conveniently specify which dimension of which atom should be allowed to relax and what should be confined/frozen. Vacuum space can be inserted between images in neighboring cells when the interactions between them need to be avoided. As shown in Figure 2.3a, for a bulk structure calculation the system is periodically continuous, so the atoms should fill up the unit cell in all three dimensions. For one single gas phase molecule, enough vacuum space should be inserted in all three dimensions to avoid the interactions between the molecule and its images in neighboring cells. The example of unit cell containing a single CO₂ molecule is shown in Figure 2.3b. A surface is normally simulated using a slab. As shown in Figure 2.3c, the atoms in the two surface dimensions (x and y) should be “continuous” (no vacuum space) and in the direction normal to the surface a vacuum space should be added.

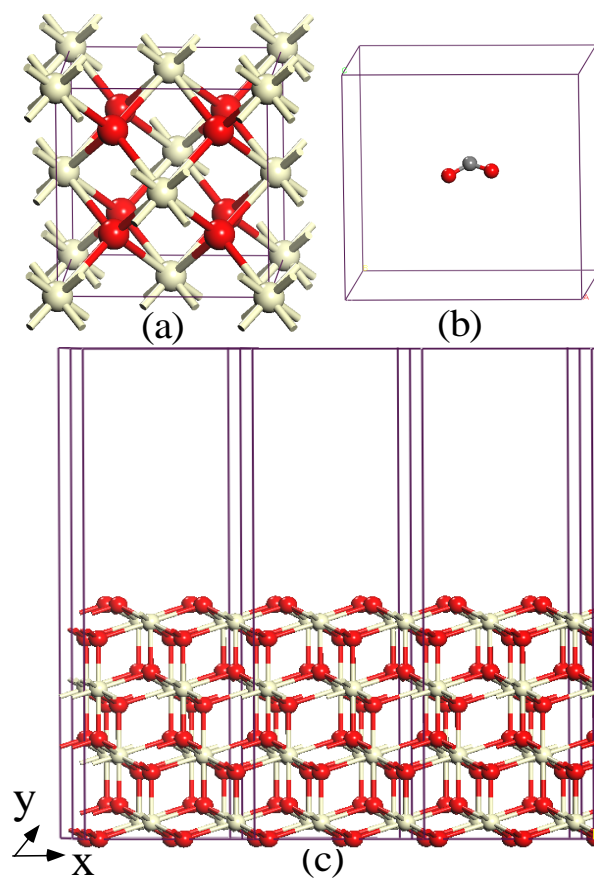


Figure 2.3. Examples of unit cells of (a) bulk CeO_2 structure, (b) a single CO_2 molecule and (c) $\text{CeO}_2(111)$ surface.

KPOINTS: The choice of KPOINTS depends both on the type of the system (cluster, surface or bulk) and on the size of the unit cell. For isolated *clusters*, due to the vacuum space inserted in all three dimensions, Γ -point was used. A *bulk* structure extends in all three dimensions of the box, so the K-points according to the Monkhorst-Pack scheme should be used. Normally, the larger the number of K-points, the more accurate the results should be and the more expensive the calculation is. Therefore, the numbers of K-points need to be large enough to guarantee the accuracy but not too large for the consideration of computational cost. The safest way to determine the proper K-points is to do an energy convergence test—calculating the same system with increasing number of K-points and the number of K-points at which the calculated energies start to converge

should be the choice of K-points. Fortunately, the convergence test is not always required. Empirically, a division in reciprocal space of less than 0.05\AA^{-1} has been shown to provide converged structures and adsorption energies, so one can conveniently choose the values of K-points accordingly. For example, if the size of a bulk unit cell is $4 \times 5 \times 2 \text{\AA}$, then the K-points should be set up to $5 \times 4 \times 10$. For surface calculations, the two dimensions within the surface (x and y) are extended in neighboring cells while a vacuum space is inserted along the dimension that is vertical to the surface (z). Thus, the choice of K-points values for the dimensions in the surface should follow the same rule as for bulk, i.e. a division in reciprocal space of less than 0.05\AA^{-1} . For the “discontinuous” z dimension, 1 should be used.

Examples of INCAR, KPOINTS, POTCAR and POSCAR files are shown in Appendix I.

If the input files are set up properly, after the calculation, the structure will be written in a file called CONTCAR. If after the required ionic relaxation steps (NSW), the calculation is still not converged yet, one can continue the calculation using the structure optimized but not yet converged from the last run (*cp CONTCAR POSCAR*). Detailed information of the calculation, including the energy of the system, will be written in the file OUTCAR.

By setting LORBIT = 12 in the INCAR file, the phase projected density of state (DOS) will be written in DOSCAR. This allows us to plot out the phase decomposed (s , p or d) density of state graph to analyze the interactions between atoms.

Bader charge⁴⁶ of the system can be analyzed by using the *Perl* code written by Henkelman et al⁴⁷. However, it is necessary to set LCHARG = T and LAECHG = T in the INCAR file before starting the calculation.

Due to the variation of the systems studied in this work, additional descriptions of computational parameters are presented in each individual chapter.

2.4.2. GAUSSIAN 03. Gaussian is very popular and widely used computational software due to its user-friendly interface. A lot of the standard or default inputs are very useful to amateurs while at the same time modifications of parameters are also available for more sophisticated users. Unlike VASP, GAUSSIAN collected various quantum mechanical methods, including the DFT method with different functional, and the perturbation method such as MP2, MP3. Both Cartesian coordinates and Z-matrix are accepted as the input coordinate. A variety of basis set are available in the program. Besides optimizing structure and calculating energy of the system, it can also be used to calculate frequencies, Raman and NMR spectrums, two or three layers of ONIOM geometry optimizations, molecular dynamics simulations, and locate transition states.

The GAUSSIAN input consists of a series of lines:

- *Link 0 Commands:* Locate and name scratch files. The location of the “Checkpoint” file should be specified in this line. The “Checkpoint” file is machine-readable and it stores the calculation results (optimized structure and orbital information). The checkpoint file is really handy when using the results of one calculation as the starting point for a second calculation. This shall save computational time. For example, when running a calculation that starts with the structure stored in the checkpoint file, one should use keyword “geom = check

guess=read” so that the system will read the structure and basis set information from the checkpoint file. However, if this line is not changed before running the second calculation, the original checkpoint file will be overwritten.

- *Route section (# lines)*: Specify desired calculation type and *iop* parameters. The main information of job type (e.g. optimization, frequency, IRC, NMR, or ADMP), computational method (e.g. ground state, TD-DFT, HF, DFT, CCSD, or MP2) and basis set are specified in this line. The internal options can also be set in this line to overwrite the system default parameters.
- *Title section*: Brief description of the calculation. Blank line is acceptable.
- *Molecule specification*: Specify molecular system to be studied. It is usually a line of charge and spin state information followed by the atom types and coordinations of each atom. Both Z-matrix and Cartesian coordinate are legal format.
- *Optional additional sections*: Additional input needed for specific job types.

Examples of GAUSSIAN 03 input were shown in Appendix II including calculations for structure optimization, transition state optimization and IRC calculation.

2.5. Computational Facilities

The Gaussian calculations in this work are performed on Dell WORKSTATION PWS650 running on Windows XP with quad-core Xeon CPU 3.20 GHz and 3.50 GB of RAM, as well as Dell Precision 380 running on Linux Redhat release 4 with Xeon CPU 2.27 GHz and 7.60 GB of RAM.

The VASP calculations were computed on high performance computer clusters “Pluto”, “Sirius” and “Procyon” of Ge’s research group, as well as the molecular science computing facility “Chinook” in Environmental Molecular Sciences Laboratory (EMSL)

located at Pacific Northwest National Laboratory. "Pluto" is composed of 25 slave nodes. Each of these slave nodes has 1.4 GHz dual Athlon processors and 1 Gb of memory. "Sirius" is composed of 24 slave nodes each with 1.8 GHz dual Opteron 244 processors and 2 Gb of memory. "Procyon" is composed of 23 slave nodes and each node has quad-core and 15.67 Gb memory. "Chinook" is sponsored by the US Department of Energy Office of Biological & Environmental Research. It has 2,310 nodes each with HP/Linux supercomputer two quad-core AMD Barcelona processors (2.2 GHz).

CHAPTER 3

EFFECT OF MORPHOLOGY, STOICHIOMETRY AND SUPPORT ON REACTIVITY OF CATALYSTS:

NO₂ INTERACTION WITH UNSUPPORTED AND Γ -Al₂O₃ SUPPORTED BaO

3.1. Introduction

NO_x (NO and NO₂) species is one of the common pollutants for our environment. One of the main manmade sources of NO_x is produced by fuel combustion in motor vehicles—diatomic nitrogen in combustion air is oxidized at high temperature. Nowadays, most of the vehicles were equipped with emission control system called catalysis convertor. The most conventional catalyst used in the catalysis convertor is the three-way catalysts. The catalysts abate hydrocarbon, CO and NO_x in the exhaust simultaneously at the stoichiometric air-to-fuel ratio combustion condition. However, in order to improve fuel efficiency, “lean-burn” technology was introduced to gasoline internal combustion engines. The lean-burn engine operates at a higher air-to-fuel ratio than the stoichiometric ratio so that the engine achieves a more complete combustion and therefore, a better fuel economy. The relative oxidative environment resulted from the high air-to-fuel ratio makes the reduction of NO_x generated during combustion more challenging, so the three-way catalysts are ineffective to eliminate NO_x under lean burn conditions.⁴⁸ To meet the stringent NO_x emission standards, alternative NO_x control technologies are needed. One of the new technologies is the NO_x storage-reduction (NSR) catalysts.⁴⁸⁻⁵¹

The design of the NSR catalyst is based on the cyclic operation of the engine between lean and rich modes, i.e. at high air-to-fuel ratio lean mode, the reduction of NO_x is not

favored, so the catalysis system stores the NO_x species temporarily; when the engine is switched to the rich mode, the stored NO_x will be released and then reduced to N_2 before being emitted into the air.⁴⁸ A typical NSR catalyst consists of porous materials as support, noble metals as active redox catalyst components and alkaline earth metal oxides as NO_x storage components. Previous study showed among many candidates for NO_x storage, BaO is the most effective towards NO_x adsorption, so it has been chosen as the main NO_x storage component in NSR catalysts.⁵² There is a general consensus that the oxidation of NO to NO_2 over the Pt sites precedes NO_x storage. A schematic illustration of this process is shown in Figure 3.1.

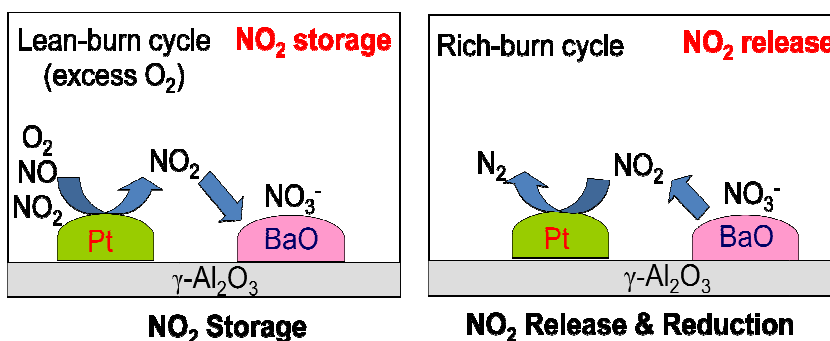


Figure 3.1. Mechanism of NO_x storage reduction (NSR) catalysis.

It was shown that the effective removal of NO_x depends strongly on effective NO_2 storage on BaO.^{49-51,53} Therefore, among all the steps involved in a cycle of NSR catalysis, the NO_x storage step has been intensely studied both experimentally^{48,54-60} and computationally.⁶¹⁻⁶⁸ The DFT method is the most popular theoretical method used to study the NO_x interaction with BaO. For example, in a work of Broqvist et al., they studied the interaction of NO_2 with the BaO(100) surface using GGA-PBE method with a $(\sqrt{2}\times\sqrt{2})$ surface slab unit cell.⁶¹ They reported that a single NO_2 molecule adsorbed over surface O sites in an N-down configuration is the most stable, with an adsorption energy

of 0.8 ± 0.05 eV. In a later publication by the same group, they studied NO_2 adsorption over a $(\text{BaO})_9$ cluster.⁶⁹ The low-coordinated cluster sites were found to have a stronger affinity towards NO_2 compared with the surface sites on a flat $\text{BaO}(100)$ surface.

However, the reported values cannot be compared to the results in our study due to the fact that the methods used in two studies were different. Branda et al. also showed that the low-coordinated sites were much more active towards NO_2 adsorption than the flat surface sites using the DFT cluster model.⁶⁴

Although the previous computational studies on NO_2/BaO interactions provided us valuable information and fundamental understanding of NO_2 interaction with BaO , the roles of other factors that can greatly impact the performance of the catalyst, such as defects and support materials, were not properly accounted for. In a lot of heterogeneous catalysis processes, the stability and activity of a catalyst can be greatly affected by the defect and support material. Particularly for the NSR catalysts, the choice of support materials has been illustrated to strongly influence the sorption property of BaO towards NO_x .^{55,60,70-75} Furthermore, the support material itself can also provide storage sites at temperatures below 300°C .⁷⁶ Therefore, the effect of defect and support cannot be ignored and need to be studied.

The NO_2 adsorption over defected clusters and surfaces was studied to illustrate the defect effect. To be able to show the change of NO_2/BaO interaction caused by the defect, we have used the results of NO_2 adsorption over $\text{BaO}(100)$ as references. Although the (100) surface were studied previously by many groups, we built and calculated our own model of $\text{BaO}(100)$ so that the results can be directly compared with the rest of the work with consistent method treatment. The (100) surface results are

shown in Section 3.3.1. The NO₂ adsorption over stoichiometric clusters is reported in the first part of Section 3.3.2. This part of results show us the size effect of BaO clusters. Stoichiometric step surface was studied as one type of defective surface and the results are shown in the second half of Section 3.3.2. Non-stoichiometric clusters and non-stoichiometric surfaces were both studied as the defects whose effect on NO₂/BaO interaction was not investigated before. The results are shown in Section 3.3.3.

Among many support materials, γ -Al₂O₃ has been used as a support material for NSR catalysts in many studies.^{49,50,59,77-81} It was shown to provide the highest NO_x storage capacity⁷⁰, so γ -Al₂O₃ surface is the choice of support in my study. The structure of γ -Al₂O₃ is by far still controversial. There are two schools of general models for γ -Al₂O₃ structure—non-spinel and defective spinel. In my worked I used the defective spinel structure that was proposed by Pinto et al⁸². More detailed information about this model will be given in the Methodology section. In addition to the choice of the support material, a highly dispersed phase of BaO on the support surface is also critical to achieve high NSR reactivity.^{71,80,83-85} For example, a flame-made Pt-Ba/Al₂O₃ catalyst was shown to contain an active Ba-containing phase where Ba species were in intimate contact with the support.⁷⁷ It has also been observed that the decomposition of Ba(NO₃)₂ crystalline supported on γ -Al₂O₃ leads to nanosized BaO particles during a NSR cycle.^{80,86} As such, a study of BaO clusters dispersed over the γ -Al₂O₃ surface and their activities towards NO₂ adsorption would help to gain insights into the NSR catalysts. The results are reported in Section 3.3.4.

In addition to the contributions of the physics that this study revealed for the NRS catalysis, this is the first time that an oxide supported oxide model was developed and studied.

3.2. Methodology

3.2.1. General Method. All the calculations in this chapter were carried out using the VASP code⁸⁷. The interaction between ions and electrons was described using the projector augmented wave (PAW) method.⁸⁷ The plane wave basis set with a cutoff energy of 400 eV was used to expand the wavefunction of valence electrons. The PBE functional⁸⁸ were used to evaluate the nonlocal exchange-correlation energy. All calculations include spin-polarization. K-point meshes generated with the Monkhorst-Pack⁸⁹ scheme were used to sample the first Brillouin zone of the surface unit cell. As discussed in Section 2.4.1, the division in reciprocal space of less than 0.05\AA^{-1} led to a $8 \times 8 \times 1$, $5 \times 8 \times 1$ and $3 \times 3 \times 1$ for BaO(100), BaO(310) and γ -Al₂O₃ supported BaO clusters, respectively. Γ -point was used for isolated clusters. The atomic structures were relaxed until the forces on the unconstrained atoms were less than 0.05 eV/\AA . Bader charge analysis was carried out for selected structures using the program developed by Henkelman and co-workers.⁹⁰

To validate the computational parameters we chose, we first optimized the bulk structure BaO with above parameters. The lattice constant was calculated to be 5.549 \AA , in good agreement with both the literature value of 5.539 \AA ⁹¹ (experimental) and 5.59 \AA ⁶⁹ (DFT calculation).

3.2.2. Modeling of Bare BaO Clusters, (100) and (310) Surfaces. Initial structures of small BaO clusters were built by extracting different size of BaO fragments from the

relaxed bulk structure. The cluster together with the adsorbed NO₂ molecule was then allowed to relax without constraints. For unsupported cluster calculations, a vacuum space of at least 10 Å in each direction was inserted between neighboring cells to avoid the unwanted interactions between its periodic images. The initial structures of unsupported BaO (100) and (310) surfaces were cleaved from the relaxed bulk BaO structure. Both surface slabs have five layers. Convergence test of NO₂ adsorption energy on BaO(100) was carried out to validate the 5-layer slab model. The test proves that five layers are thick enough to simulate the surface. The bottom two layers of the five layer slab were kept frozen at the respective bulk positions whereas the top three layers together with the adsorbed NO₂ molecule were allowed to relax during the calculations.

3.2.3. Modeling of γ -Al₂O₃ Supported BaO Clusters. There exist two molecular models of γ -Al₂O₃⁹²⁻⁹⁵—the defective spinel⁸² model and the non-spinel model⁹⁶. In this work, the defective spinel model was used. The perfect spinel structure was named after the crystal structure of MgAl₂O₄. We start building the defective γ -Al₂O₃ structure by substituting Mg atom in the MgAl₂O₄ crystal structure with Al atom, so that we have spinel Al₃O₄. Then a supercell containing 18 Al and 24 O atoms was created, in which two Al atoms have to be removed to maintain the stoichiometry (defective spinel). The nature and distribution of the vacancies in the spinel structure is also a hotly debated subject⁹⁷. The choice of Al atoms to be removed was discussed in Pinto's work⁸². We chose to remove the two Al atoms that correspond to the lowest energy penalty, i.e. the system is most stable after removing this combination of Al atoms. The removals of the two Al atoms were illustrated in Figure 3.2. This Al₁₆O₂₄ structure was then allowed to fully relax.

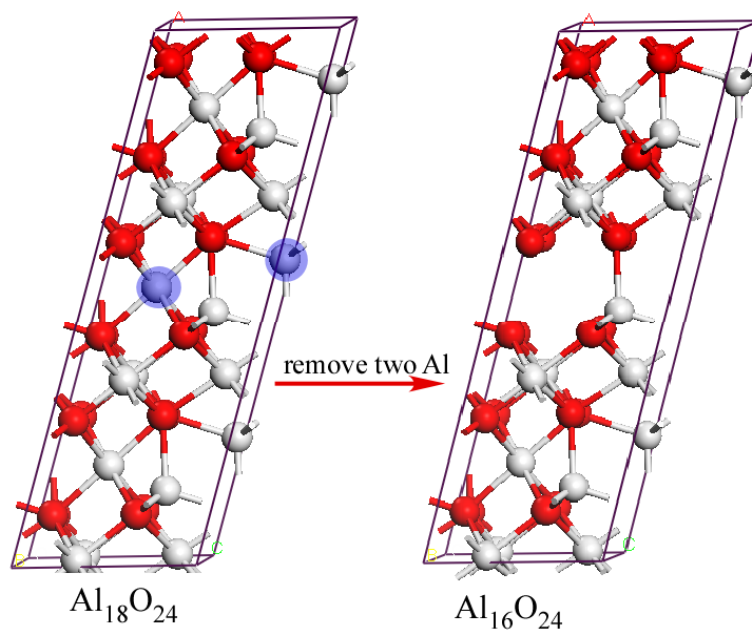


Figure 3.2. The supercells of non-stoichiometric spinel $\text{Al}_{18}\text{O}_{24}$ and stoichiometric defective spinel $\text{Al}_{16}\text{O}_{24}$ after removing two Al atoms highlighted in the $\text{Al}_{18}\text{O}_{24}$ structure. ($a = 17.14\text{\AA}$, $b = 5.71\text{\AA}$, $c = 5.17\text{\AA}$, $\alpha = \beta = \gamma = 60^\circ$)

The $\gamma\text{-Al}_2\text{O}_3(111)$ surface with the lowest surface energy of 0.98 J/m^2 after relaxation was chosen as the substrate for BaO in this study. The $\gamma\text{-Al}_2\text{O}_3(111)$ surface is shown in Figure 3.3. For the calculations of the $\gamma\text{-Al}_2\text{O}_3$ supported BaO clusters, the bottom four layers of $\gamma\text{-Al}_2\text{O}_3(111)$ were kept frozen and the top five layers together with BaO and NO_2 were allowed to relax.

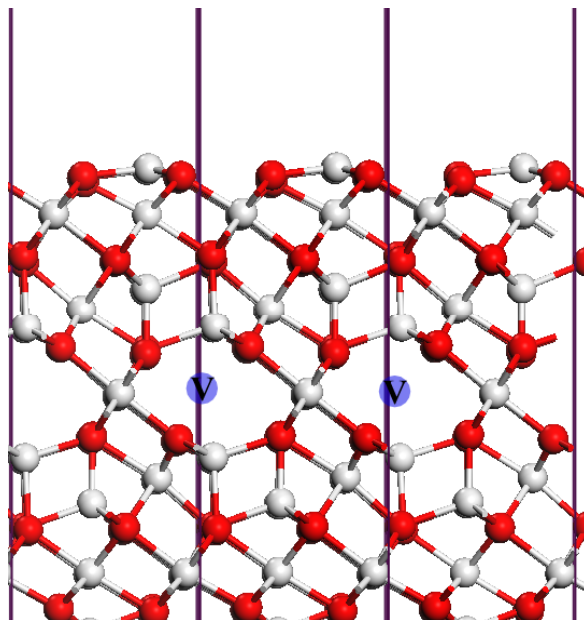


Figure 3.3. Side view of $\gamma\text{-Al}_2\text{O}_3(111)$ surface. The Al vacancy sites were labeled.

3.3. Results and Discussion

3.3.1. NO_2 Interaction with $\text{BaO}(100)$ Surface. We first calculated NO_2 adsorption over the perfect $\text{BaO}(100)$ flat surface. This system has been a subject of many theoretical studies^{61,63,66-68}, and our results only serve as references for comparison with NO_2 adsorption on other BaO substrates. Top views of three optimized NO_2 adsorption configurations on various surface sites are shown in Figure 3.4, along with the corresponding adsorption energies. The adsorption energies were calculated using

$$E_{ads} = E_{sub+NO_2} - (E_{NO_2} + E_{sub}), \quad (3.1)$$

where E_{sub} and E_{NO_2} are the energies of BaO substrate and gas phase NO_2 molecule, respectively. E_{sub+NO_2} is the energy of the structure where NO_2 is adsorbed on the BaO substrate. The most stable NO_2 adsorption configuration is shown in Figure 3.4a. In this structure, the N atom of the NO_2 molecule sits on top of a surface O site and the two O atoms of NO_2 point to two surface Ba atoms. The plane of the adsorbed NO_2 molecule is

almost parallel to the surface. The adsorption energy of this structure was calculated to be -1.06 eV. The two configurations with NO_2 being adsorbed at the surface Ba site(s) (Figure 3.4b and c) are less stable. The relative stabilities of these three adsorption structures are in agreement with previous works.^{15,17,66,67} For example, using the GGA-PBE method implemented in CASTEP with a fixed two-layer slab, Broqvist et al. also reported that the NO_2 adsorption on the O site of $\text{BaO}(100)$ surface is the most favorable adsorption configuration⁶¹. The adsorption structure they reported is very similar to the structure in Figure 3.4a and the adsorption energy is ~ -0.8 eV. In later works by the same group, the NO_2 adsorption on the $\text{BaO}(100)$ surface were again calculated but using the GGA-PBE method implemented in the CPMD code and three-layer $p(3\times 3)$ surface slabs. The NO_2 adsorption over the surface O site with an adsorption energy of -1.32 eV was also found to be most stable.^{66,67} Using the GGA-PW91 method and ultrasoft pseudopotentials implemented in the VASP code, Schneider calculated the adsorption energy to be ~ -1.5 eV for a similar NO_2 adsorption geometry on the O site of $\text{BaO}(100)$ surface.⁶³ Clearly, the values of adsorption energy calculated by different authors with different methods may not be directly compared. Tutuianu et al. compared the results reported by different authors and found that the calculated NO_2 adsorption energies on $\text{BaO}(100)$ in a similar adsorption configuration can be greatly affected by the NO_2 coverage and the number of BaO layers.⁶⁸ The NO_2 adsorption energy at the coverage of the present work was -0.9 eV in that study using five-layer slab.⁶⁸ Nevertheless, a consistent conclusion that the O site of the $\text{BaO}(100)$ surface is the most favorable NO_2 adsorption site can be reached.

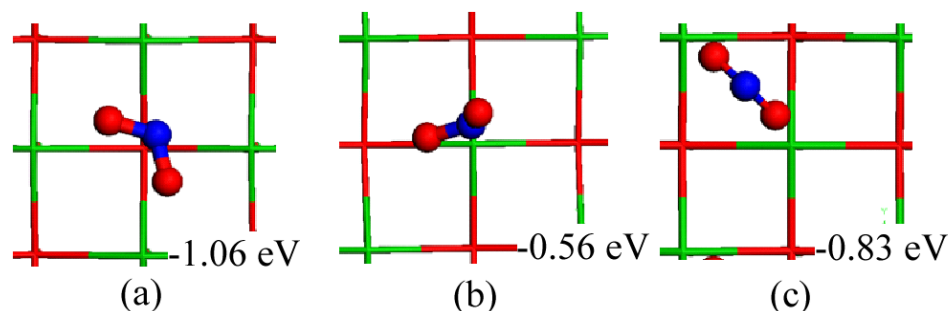


Figure 3.4. Top view of the adsorption geometries and energies of NO₂ on the BaO(100) surface. (a) N-down over the surface O site; (b) N-down over surface Ba site; (c) O-down in a bidentate configuration. The BaO(100) surface is shown in stick and NO₂ molecule in ball and stick. (Red: O, Green: Ba, Blue: N) Reproduced with permission from *J. Phys. Chem. C*, 2008, 112, 16924. Copyright 2008 American Chemical Society.

3.3.2. NO₂ Interaction with Stoichiometric BaO Clusters and Stepped Surface. *a.*

Stoichiometric Clusters. Our calculation started with the smallest cluster (BaO)₁ and increased to (BaO)₂, (BaO)₄, and (BaO)₃₂. The structures of these clusters were constructed based on the rock-salt structure of bulk BaO. The smallest cluster (BaO)₁ is linear and only has one dimension. The (BaO)₂ cluster is a square and it has two atoms on each side (2 × 2). The (BaO)₄ cluster is the smallest three-dimensional cluster and has a cubic structure with 2 atoms on each edge (2 × 2 × 2). The clusters that have 3 atoms on each edge (3 × 3 × 3) have odd number of atoms. They are non-stoichiometric and will be discussed in the following section. Therefore, the next stoichiometric cluster in this series is (BaO)₃₂ which has 4 atoms on each edge (4 × 4 × 4). The mean Ba–O bond lengths of these clusters were calculated to be 2.02, 2.30, 2.45 and 2.68 Å for (BaO)₁, (BaO)₂, (BaO)₄ and (BaO)₃₂, respectively. These bond lengths are shorter than the Ba–O bond length of 2.79 Å in bulk BaO. Bader charge analysis showed that for (BaO)₁, (BaO)₂ and (BaO)₄, the charge on each Ba atom and O atom has the same magnitude but opposite signs. The charges on Ba atoms in these clusters are 1.22, 1.31 and 1.36 |e|, respectively. Unlike in the smaller clusters, Ba or O atoms in (BaO)₃₂ are not in the

equivalent positions. Consequently, the charges on Ba or O atom in $(\text{BaO})_{32}$ varies according to the exact location of the atom in the cluster. The interior Ba and O atoms (4 each) have Bader charges of 1.33 and $-1.40 |e|$, respectively. These values are close to the Bader charge of the atoms in bulk BaO ($1.36 |e|$). The Bader charges of the surface and edge Ba atoms span in the range of $1.42 \sim 1.45 |e|$, whereas those of surface and edge O atoms range from -1.40 to $-1.45 |e|$. Obviously, the charges on the surface and edge atoms are bigger than those on the atoms in bulk BaO. In fact, similar charge redistribution was observed in the BaO(100) surface layers—the surface atoms have bigger charges than the bulk atoms. The larger charges on the surface Ba/O atoms are related to the relaxation at the surface.

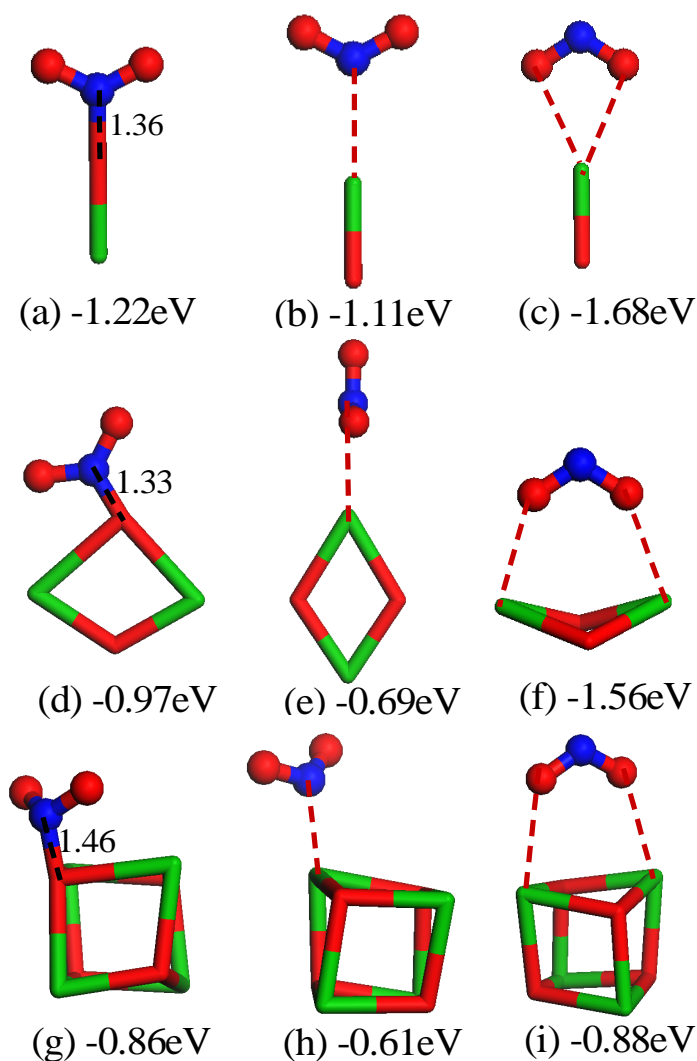


Figure 3.5. The adsorption geometries and energies of NO_2 over the stoichiometric BaO clusters. NO_2 adsorption at the O site of (a) $(\text{BaO})_1$, (d) $(\text{BaO})_2$ and (g) $(\text{BaO})_4$; NO_2 adsorption at the Ba site of (b) $(\text{BaO})_1$, (e) $(\text{BaO})_2$ and (h) $(\text{BaO})_4$; NO_2 bidentate adsorption at (c) $(\text{BaO})_1$, (f) $(\text{BaO})_2$ and (i) $(\text{BaO})_4$. While $\text{NO}_3^{\delta-}$ species forms, the $\text{N-O}_{\text{cluster}}$ bond length is labeled. Reproduced with permission from *J. Phys. Chem. C*, 2008, 112, 16924. Copyright 2008 American Chemical Society.

For each of the stoichiometric clusters, we calculated the NO_2 adsorption over a single O site and a single Ba site as well as in a bridging bidentate configuration over two Ba sites. The optimized structures were shown in Figure 3.5 together with the corresponding adsorption energies. The adsorption energies were also calculated

according to Equation 3.1. The structures in Figure 3.5 were arranged from left to right in each row: NO₂ adsorption on a single O site, on a single Ba site, and in a bidentate configuration with O down bridging over Ba atoms adsorption. As shown in Figure 3.5, for each cluster, the NO₂ adsorption configuration in which the two O atoms of NO₂ bridge over the cluster Ba atom(s) (Figure 3.5c, f and i) is the most energetically favorable. This is different from NO₂ adsorption on BaO(100), as shown in Figure 3.4, where the surface O site is most stable.

The bridging bidentate configuration of NO₂ adsorption on the (100) surface of MgO, CaO, SrO, and BaO was classified as basic NO₂ by Schneider.⁶³ This can be attributed to the fact NO₂ was adsorbed in a surface Ba (basic) site and acted as an electron acceptor. Bader charge analysis showed that for the bidentate configuration in Figure 3.5f, the NO₂ fragment became negatively charged with a net charge of $-0.86 |e|$. The charges on the two Ba atoms were increased to $1.48 |e|$, whereas those on the two O atoms became $-1.05 |e|$. The interaction through the O atoms of NO₂ was weakened as the size of the cluster was increased, as shown in the right column of Figure 3.5. We note that the strong Ba_{cluster}-O_{NO2} interactions caused the BaO square to deform from its original planar structure (Figure 3.5f). However, the structural distortion of (BaO)₄ due to NO₂ adsorption was counteracted by the underneath BaO units, as shown in Figure 3.5i. The structural rigidity of (BaO)₄ reduced the energy gain through the “basic adsorption”. As such, the “acidic adsorption” of forming a NO₃^{δ-} shown in Figure 3.5g became almost as stable as the “basic adsorption” of forming NO₂^{δ-}. Our results of the adsorption structures of NO₂ on the (BaO)₁ and (BaO)₄ clusters are similar to the results reported by Gronbeck et al.⁶⁷ However, our calculated adsorption energies of -1.68 and -0.88 eV on (BaO)₁

and $(\text{BaO})_4$, respectively, are consistently larger than the corresponding values of -1.48 and -0.74 eV reported in that work.⁶⁷ Furthermore, these authors⁶⁷ did not report the formation of $\text{NO}_3^{\delta-}$ structures shown in Figure 3.5a,d,g. For example, the N-down configuration on the edge of $(\text{BaO})_6$ has a $\text{N}-\text{O}_{\text{cluster}}$ distance of 3.09 \AA and adsorption of -1.07 eV ⁶⁷.

We also explored NO_2 adsorption on different sites of the $(\text{BaO})_{32}$ cluster. Due to the large size of the cluster, each facet of the cluster has some characteristics of the $\text{BaO}(100)$ surface. As such, we expected the interaction of NO_2 with the center of the cluster surface to be similar to that with the $\text{BaO}(100)$ surface. Indeed, our results showed that the NO_2 adsorption energies at the center O and Ba sites of each facet were slightly smaller than but comparable to those on the $\text{BaO}(100)$ surface. The adsorption at the cluster edge and corner site, on the other hand, is stronger than on the flat (100) surface. For example, at the cluster O edge site and Ba corner site, the NO_2 adsorption energies are -1.14 and -0.90 eV, respectively. Adsorption at the edge O site also led to the formation of a $\text{NO}_3^{\delta-}$ species with a $\text{N}-\text{O}_{\text{cluster}}$ distance of 1.45 \AA .

b. Stoichiometric Stepped Surface. In addition to the edges of a cluster, edge sites can also be generated by a controlled cleavage of a bulk crystal. Step-edge is a common type of defect on surfaces, often separated by varying sizes of terraces. In this study, we used $\text{BaO}(310)$ cleaved from the relaxed bulk BaO to represent the stepped surface. A perspective view of $\text{BaO}(310)$ was shown in Figure 3.6a, with the step-edge and terrace sites being labeled. On the $\text{BaO}(310)$ surface, the activities of the terrace Ba and O sites that are away from the step-edge are very similar to those on the flat $\text{BaO}(100)$ surface. However, the step-edge Ba and O sites show different activities towards NO_2 adsorption.

For example, the adsorption of NO_2 at the step-edge O site forms a $\text{NO}_3^{\delta-}$ -like species that was not found on the flat $\text{BaO}(100)$ surface (Figure 3.6b). NO_2 adsorption in this configuration has an adsorption energy of -1.13 eV. Although the adsorption energy is only slightly greater than the NO_2 adsorption energy at the surface O site of $\text{BaO}(100)$ (Figure 3.4a, -1.06 eV), the formation of $\text{NO}_3^{\delta-}$ species makes the configuration similar to the adsorption at the edge O site of the $(\text{BaO})_{32}$ cluster rather than on the O site of $\text{BaO}(100)$. The $\text{N}-\text{O}_{\text{surface}}$ distance in the $\text{NO}_3^{\delta-}$ species is 1.46 Å. The NO_2 molecule can also be adsorbed on the step-edge Ba site with two oxygen atoms pointing to the Ba site (Figure 3.6c), yielding an adsorption energy of -0.73 eV, stronger than that on the Ba sites of the (100) surface (-0.56 eV). The enhanced activities of the step-edge Ba and O sites on $\text{BaO}(310)$ can be attributed to the low coordination numbers of these sites. These low-coordination sites have a higher degree of bond unsaturation and allow a higher degree of steric flexibility than the sites on the flat surface. Our results are different from that of Broqvist et al⁹⁸, who showed the higher coordination 4S and 5S oxygen sites on a $(\text{BaO})_9$ cluster had stronger binding toward NO_2 than the low-coordination 3S sites. We again note that none of the adsorption configurations of a single NO_2 molecule reported in their work⁹⁸ resulted in the nitrate species.

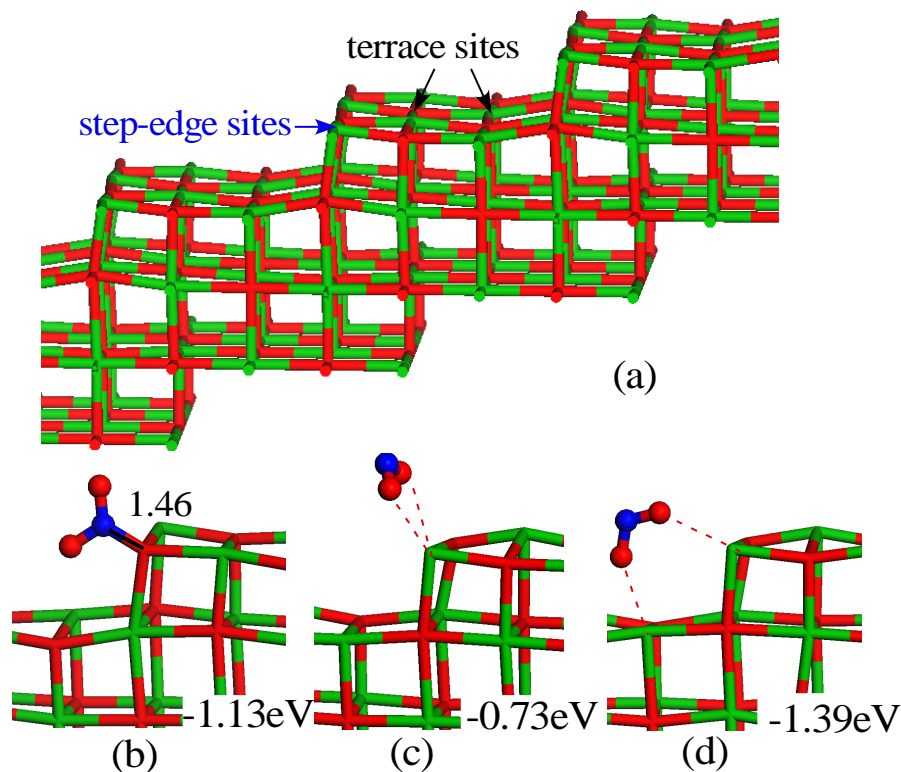


Figure 3.6. (a) A perspective view of the BaO(310) surface showing the step-edge sites and terrace sites. (b) NO₂ is adsorbed at the (310) edge O site forming NO₃^{δ-}. The N-O_{cluster} bond length of the NO₃^{δ-} species is labeled. (c) NO₂ is adsorbed in O-down (bidentate) configuration over a step surface edge Ba site. (d) NO₂ bridges over the step-edge and terrace Ba sites. Reproduced with permission from *J. Phys. Chem. C*, 2008, 112, 16924. Copyright 2008 American Chemical Society.

Furthermore, the creation of the steps produced adsorption sites that did not exist on the flat BaO(100) surface. For example, an NO₂ adsorption configuration with the two O atoms bridging over the two Ba sites from different terraces, shown in Figure 3.6d, would not be formed on BaO(100). This adsorption configuration has an adsorption energy of -1.39 eV and is the energetically most favorable NO₂ adsorption configuration on the BaO(310) surface. The NO₂-BaO interaction in this configuration is even stronger than the bidentate adsorption configuration on the perfect BaO(100) surface and has not been reported.

Branda et al. also studied the effect of the steps on BaO-NO₂ interaction by using an embedded cluster model to simulate the stepped BaO surfaces.⁶⁴ They concluded that the adsorption energies of NO₂ at the surface step sites were enhanced by ~ 100% and 35% from those on the BaO(100) surface for N-down and O-down configurations, respectively. Our results showed enhancements of step-edge sites towards NO₂ adsorption but much less dramatic. Our calculated adsorption energies for N-down configuration was increased by 0.07 eV (~6%). The adsorption energy in the new NO₂ adsorption configuration formed across the step of BaO(310) (Figure 3.6d) was increased by -0.56 eV over the O-down configuration on BaO(100). We would like to stress that this new configuration cannot be formed on BaO(100).

3.3.3. NO₂ Interaction with Non-stoichiometric BaO Surfaces and Clusters. a. Non-stoichiometric Clusters. The study of stoichiometric clusters in previous section provided a measure of the geometry of the substrate on its interaction with NO₂. The study of the non-stoichiometric clusters shown next will illustrate how the electronic characters of the substrate affect the adsorption of NO₂. The initial structures of the two non-stoichiometric cubic clusters, Ba₁₃O₁₄ and Ba₁₄O₁₃, were also constructed on the basis of the bulk structure. Apparently, Ba₁₄O₁₃ cluster has an extra Ba atom whereas the Ba₁₃O₁₄ has an extra O atom with respect to the 1:1 stoichiometric ratio. Bader charge analysis was performed for both clusters. The averaged charges of Ba and O atoms are +1.44 |e| and -1.34 |e| in Ba₁₃O₁₄ and +1.34 |e|, -1.44 |e| in Ba₁₄O₁₃, respectively. There are two types of Ba atoms and two types of O atoms in each cluster, depending on position of each atom. In Ba₁₃O₁₄, twelve Ba atoms are located at the center of each edge of the cube (edge-center) and one is in the center of the cube (cube-center) (Figure 3.7a). The charge

on the two types of Ba atoms differs only by ~ 0.1 |e|. Two types of oxygen atoms, eight are located at the corner and six in the center of each face (face center). The difference in the charge of the two types of oxygen atoms is less than 0.1 |e|. The excess O atom in $\text{Ba}_{13}\text{O}_{14}$ makes the cluster electrophilic. For the $\text{Ba}_{14}\text{O}_{13}$ cluster, there are 12 edge-center oxygen atoms and one cube center oxygen atom, and eight corner Ba atoms and 6 face-center Ba atoms (Figure 3.7e). Again, the difference of charges on the atoms in different positions is noticeable. The excess electrons due to the extra Ba atom of $\text{Ba}_{14}\text{O}_{13}$ can be easily donated, making the cluster nucleophilic.

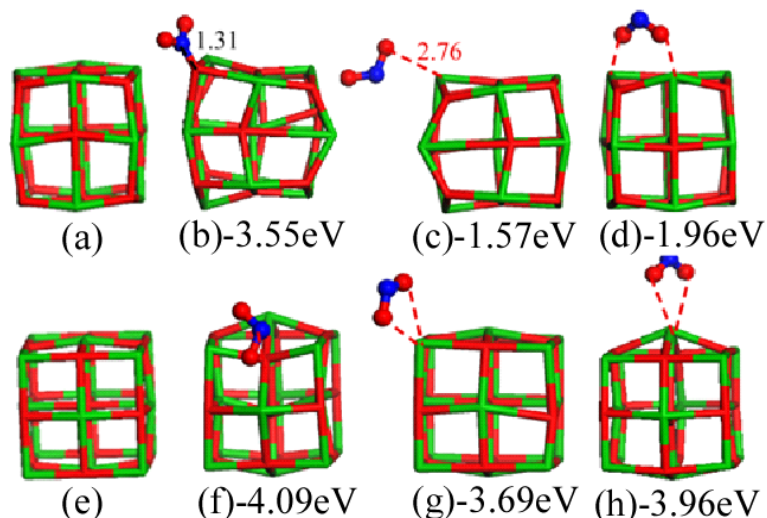


Figure 3.7: NO_2 adsorption on the non-stoichiometric clusters. (a) and (e): The bare $\text{Ba}_{13}\text{O}_{14}$ and $\text{Ba}_{14}\text{O}_{13}$ cluster. On the $\text{Ba}_{13}\text{O}_{14}$ cluster: (b) N-down forming nitrate at cluster corner O site. The $\text{N-O}_{\text{cluster}}$ bond length of the $\text{NO}_3^{\delta-}$ species is labeled. (c) one O atom of NO_2 interacts with the cluster edge Ba site, and (d) bidentate with two O atoms bridging over two cluster Ba sites. On $\text{Ba}_{14}\text{O}_{13}$ cluster: (f) N-down at the cluster edge O site, (g) O-down at the cluster corner Ba site, and (h) O-down at the cluster face-center Ba site. Reproduced with permission from J. Phys. Chem. C, 2008, 112, 16924. Copyright 2008 American Chemical Society.

We first examined NO_2 adsorption over the $\text{Ba}_{13}\text{O}_{14}$ cluster at corner O site and edge Ba site as well as in a bridging bidentate configuration over the two Ba atoms. The optimized NO_2 adsorption geometries were shown in Figure 3.7. The adsorption energies are -3.55 , -1.57 , and -1.96 eV for adsorption at the corner O site (Figure 3.7), the edge

Ba site (Figure 3.7c) and the bridge bidentate configurations (Figure 3.7d). These adsorption energies are significantly larger than those on the stoichiometric clusters. The structure of the clusters was strongly distorted upon NO₂ adsorption (Figures 3.7b-d). Among the three adsorption structures, NO₂ directly bound the cluster O site with an adsorption energy of -3.55 eV is the most stable structure. In this structure, a NO₃^{δ-} species is formed through the “acidic adsorption”.⁶³ The N-O_{cluster} distance in this NO₃^{δ-} species is 1.31 Å, close to 1.24 Å of N-O bond in NO₃⁻. The formation of the NO₃^{δ-} species was facilitated by both the electrophilic nature of the Ba₁₃O₁₄ cluster and the electron donating ability of NO₂: the lone pair electrons on N atom were shared with Ba₁₃O₁₄.

We then calculated NO₂ adsorption on the Ba₁₄O₁₃ cluster edge O site, corner Ba site and face-center Ba site. The adsorption energies are -4.09, -3.69 and -3.96 eV for the relaxed structures shown in Figure 3.7f (edge O site), Figure 3.7g (corner Ba site) and Figure 3.7h (face-center Ba site), respectively. Strong distortions from the bare Ba₁₃O₁₄ cluster structure can be observed upon NO₂ adsorption in Figure 3.7f and h, whereas the original cluster geometry was very much maintained after NO₂ adsorption at the corner Ba site (Figure 3.7g). In structure shown in Figure 3.7f, the N-O_{cluster} distance (3.02 Å) is too long to have any significant bonding interactions although the N atom points to the edge O atom of the cluster. In fact, the distances between the O atoms of NO₂ and the nearest Ba atoms are ~ 2.8 Å, close to that of a Ba-O ionic bond. Consequently, the O-Ba interactions dominate NO₂ adsorption on Ba₁₄O₁₃ in all three structures shown in figure 3.7f-h. The strong basic adsorption of NO₂ on various Ba₁₄O₁₃ cluster sites is a consequence the nucleophilic nature of the cluster: the excess Ba atom makes the cluster

electron-rich. As a Lewis base, the nucleophilic $\text{Ba}_{14}\text{O}_{13}$ cluster can interact with NO_2 strongly by donate its electrons to the molecule. As such, the “acidic adsorption” where NO_2 shares its lone pair electrons with the substrate and forming $\text{NO}_3^{\delta-}$ does not occur on the $\text{Ba}_{14}\text{O}_{13}$ cluster.

b. Non-stoichiometric Surfaces. Surface vacancy is another type of defects that may have great effects on the catalytic activity of metal oxides.^{14,64} The existence of vacancies creates charged centers on the surface which may affect the relative stability between the reactant and product states as well as the transition state. Herein, we studied the effect of both Ba and O vacancies in the $\text{BaO}(100)$ surface on NO_2 adsorption. We used the same surface unit cell as in our calculations for NO_2 adsorption on the perfect $\text{BaO}(100)$ surface to eliminate the coverage effect for comparison. Although the vacancy density simulated by such a unit cell may be too high to quantitatively compare with the surface under operating conditions, we expect the model will provide some insights into the effect of these defects on NO_2 adsorption.

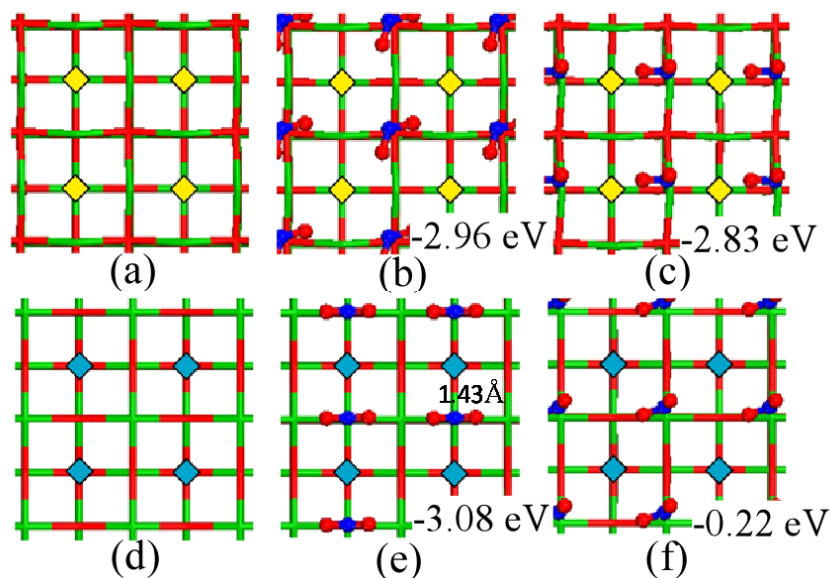


Figure 3.8: Top view of NO_2 adsorption on defective $\text{BaO}(100)$. (a) $\text{BaO}(100)$ with oxygen vacancies. (b) NO_2 adsorption at the surface O site. (c) NO_2 adsorption at the surface Ba site. (d) $\text{BaO}(100)$ with barium vacancies. (e) NO_2 adsorption at the surface O site forming nitrate. The N-

O_{cluster} bond length of the $\text{NO}_3^{\delta-}$ species is labeled. (f) NO_2 adsorption at the surface Ba site. The surface is shown in stick and the adsorbed NO_2 molecule is shown in ball and stick. Yellow and cyan diamonds represent the surface O and Ba vacancies, respectively. Reproduced with permission from J. Phys. Chem. C, 2008, 112, 16924. Copyright 2008 American Chemical Society.

The O vacancy on BaO(100) was created by eliminating a neutral O atom from the surface layer of the slab, as shown by the yellow diamond in Figure 3.8a. By creating a neutral O vacancy on the surface, the slab simulating the BaO surface became non-stoichiometric with an extra Ba atom. Similar to $\text{Ba}_{14}\text{O}_{13}$, this extra Ba atom made the electron transfer from the defective BaO surface to adsorbed NO_2 favorable, resulting in a strong adsorption of NO_2 on both surface O site and Ba site. The optimized adsorption structures on the O site and the Ba site were shown in Figure 3.8b and c with the corresponding adsorption energies of -2.96 and -2.83 eV, respectively. In the adsorption configuration of NO_2 over the surface O site (Figure 3.8b), the NO_2 molecular plane was parallel to the surface with each O atom pointing to the corresponding surface Ba site. The structure of NO_2 adsorption on top of Ba site is very similar to that of perfect (100) surface (Figure 3.4b) except for that one of the O atoms in the NO_2 molecule now points to the surface O vacancy site where the surface oxygen used to reside. Bader charge analysis show that NO_2 adsorbed at the Ba site of the defective surface gains $0.85 |e|$ from the surface, significantly larger than the charge gained in similar adsorption geometry on the perfect (100) surface. Similar to the $\text{Ba}_{14}\text{O}_{13}$ cluster, such nucleophilic substrate can readily donate its electronic charge to the adsorbate. Therefore, the charge transfer from the surface with O vacancies to NO_2 molecule is significantly larger than that from the perfect (100) surface. For the same reason, the “acidic adsorption” configuration where NO_2 shares its lone pair with the surface O site, forming a nitrate-like species, was not found on the defective surface with oxygen vacancies.

In contrast, creating a surface Ba vacancy (shown in Figure 3.8d in cyan diamond) makes the slab have an extra oxygen atom in the unit cell. Consequently, the slab holds onto its electrons tight, making the slab electrophilic. As such, the “acidic adsorption” that NO₂ shares its lone pair electrons became favorable. The structure of NO₂ adsorbed over the surface O site forming a nitrate-like species (Figure 3.8e) has an adsorption energy of -3.08 eV. On the other hand, the “basic adsorption” on the surface Ba site (Figure 3.8f) yielded an adsorption energy of only -0.22 eV.

In summary, the non-stoichiometric clusters have multiple sites that are much more active towards NO₂ adsorption than the stoichiometric clusters. Many surface sites on the defective BaO surfaces also became highly active towards NO₂ adsorption. The NO₂ molecule is amphiphilic and can act as either Lewis acid or base by interacting with the surface through different parts of the molecule. When the barium oxide is electron-rich, the excess electrons can be readily donated to the NO₂ molecule through the “basic” adsorption mode, i.e. the O atoms of the NO₂ molecule approaching the surface sites. On the other hand, if the defects make BaO electron-deficient, NO₂ favors the “acidic” adsorption mode by forming a nitrate-like species. In the latter case, N atom of the molecule approaches a surface O site and shares its lone pair electrons with the surface O atom. On both non-stoichiometric clusters and non-stoichiometric slabs, the “basic” adsorption of NO₂ occurs for both electron-rich and electron-deficient substrates although the NO₂-substrate interaction for the electron-rich substrate is much stronger. In contrast, only “acidic” adsorption occurs at the O site of an electron-deficient adsorbate.

3.3.4. NO₂ Interaction with γ -Al₂O₃ Supported BaO Clusters. a. γ -Al₂O₃ Supported BaO Clusters. To study the support effect on NO₂-BaO interaction, we used a c(2×1) unit cell of the γ -Al₂O₃(111) supported (BaO)₁, (BaO)₂ and (BaO)₄ clusters as the computational model. The c(2×1) unit cell of γ -Al₂O₃ surface slab is consist of 32 Al and 48 O atoms.

The initial structures of the supported cluster models were built based on the structurally optimized γ -Al₂O₃(111) surface and BaO clusters. For example, to build γ -Al₂O₃ supported (BaO)₂ structure, in a molecular modeling visualization software, the optimized (BaO)₂ square was placed on top of the optimized γ -Al₂O₃ surface slab. The BaO square can be placed with its plane either normal or parallel to the γ -Al₂O₃(111) as shown in Figure 3.9. By comparing the energies of these two structures, it was found the “paralleled” BaO square is more stable, so the “parallel” model was selected for further study of NO₂ adsorption.

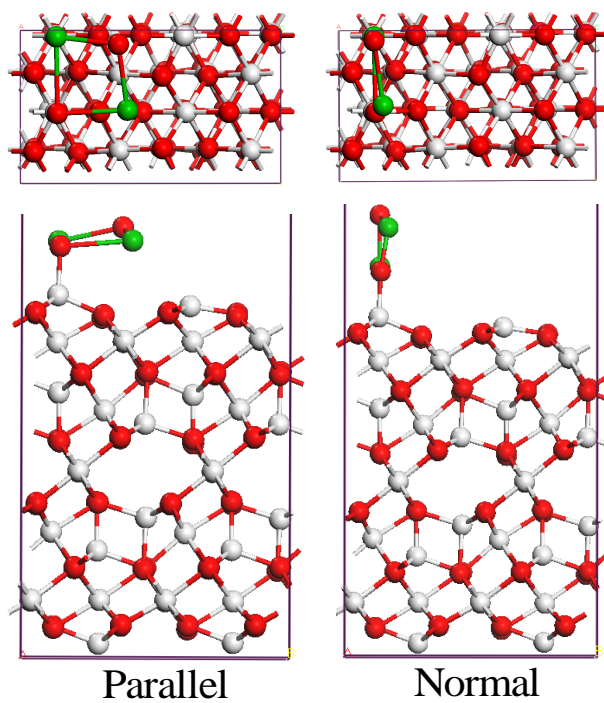


Figure 3.9: (BaO)₂ supported on γ -Al₂O₃(111) with the BaO cluster square plane parallel and normal to the support surface, respectively.

The same rule applied to the selections of the supported (BaO)₁ and (BaO)₂ cluster structures for further NO₂ adsorption study. The selected supported cluster structures are shown in Figure 3.10.

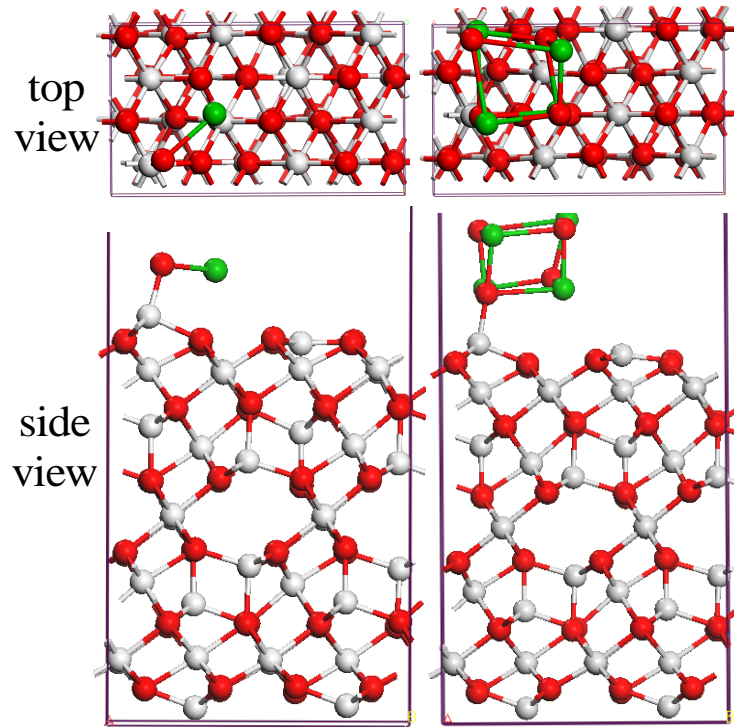


Figure 3.10: Most stable structures of $\gamma\text{-Al}_2\text{O}_3(111)$ supported $(\text{BaO})_1$ and $(\text{BaO})_4$.

Note that for all the structures of supported clusters, all the BaO clusters were stabilized by anchoring an oxygen atom at the $\gamma\text{-Al}_2\text{O}_3(111)$ surface cation site. The other atoms in the clusters do not have direct bonding interaction with the substrate. The binding energy of the clusters to the support surface can be calculated using:

$$E_{\text{Binding}} = E_{\text{SuppCluster}} - (E_{\text{cluster}} - E_{\text{Supp}}), \quad (3.2)$$

where E_{cluster} and E_{Supp} are the energies of the gas phase BaO cluster and bare $\gamma\text{-Al}_2\text{O}_3(111)$ surface, respectively. $E_{\text{SuppCluster}}$ is the energy of the support surface along with the cluster bound to it. E_{Binding} were calculated to be -5.99 , -5.74 and -5.54 eV for $(\text{BaO})_1$, $(\text{BaO})_2$ and $(\text{BaO})_4$, respectively, implying strong interactions between the BaO clusters and the support surface. Bader charge analysis showed that with the support surface, the Ba–O bonds of the BaO clusters became more ionic. For example, the Bader

charges of two oxygen atoms in the supported $(\text{BaO})_2$ are -1.72 (anchoring) and -1.40 $|e|$, respective, larger than -1.31 $|e|$ of the oxygen in the bare/unsupported $(\text{BaO})_2$ cluster.

b. NO_2 Adsorption on $\gamma\text{-Al}_2\text{O}_3$ Supported BaO Clusters. For the supported $(\text{BaO})_1$ cluster, there are two sites available on the BaO for NO_2 adsorption—the O site which is also anchoring the cluster to the support surface and the Ba site. The adsorption energies can be calculated using Equation 3.1 with the relaxed structure of $\gamma\text{-Al}_2\text{O}_3$ -supported $(\text{BaO})_1$ as the substrate. The NO_2 can be adsorbed on the $(\text{BaO})_1$ anchoring O site forming a $\text{NO}_3^{\delta-}$ species (Figure 3.11a) with an adsorption energy of -0.85 eV. NO_2 adsorption at the Ba site corresponds to an adsorption energy of -0.42 eV, less stable than on the anchoring O site. This implies that although the O site is already bonded to Al and Ba atoms, it is still more active towards NO_2 adsorption than the Ba site. This is in contrast to the NO_2 interaction with unsupported BaO monomer where Ba site was favored.

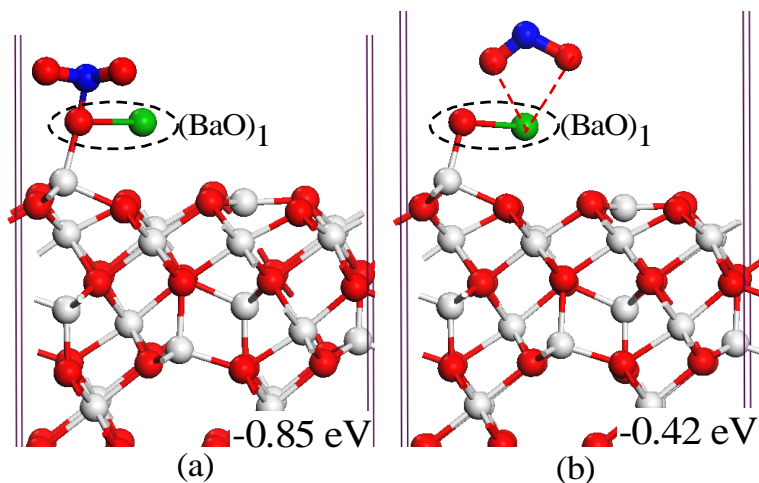


Figure 3.11 NO_2 adsorption over $\gamma\text{-Al}_2\text{O}_3(111)$ supported $(\text{BaO})_1$ O site (a) and Ba site (b).

Based on the results of the supported BaO monomer calculations, the O site of the cluster is more active towards NO_2 adsorption, so for the calculations of NO_2 interacting

with supported $(\text{BaO})_2$ and $(\text{BaO})_4$, only the cluster O sites that were not connected to the $\gamma\text{-Al}_2\text{O}_3$ surface were studied as the active adsorption sites. We found a strong synergy from BaO clusters and $\gamma\text{-Al}_2\text{O}_3$ for NO_2 adsorption: a NO_2 molecule interacts with the BaO cluster O atom and the $\gamma\text{-Al}_2\text{O}_3$ support surface simultaneously, yielding a very large adsorption energy. The synergistic adsorption structures are shown in Figure 3.12 with the adsorption energies of -3.10 and -2.23 eV for supported $(\text{BaO})_2$ and $(\text{BaO})_4$ clusters, respectively. These two structures are the most favorable NO_2 adsorption geometries on the supported clusters. The most favorable adsorption structure for NO_2 over unsupported $(\text{BaO})_2$ and $(\text{BaO})_4$ clusters with the two oxygen atoms of NO_2 bridging over two Ba sites (Figure 3.5f and i) were much less stable over the supported $(\text{BaO})_2$ and $(\text{BaO})_4$.

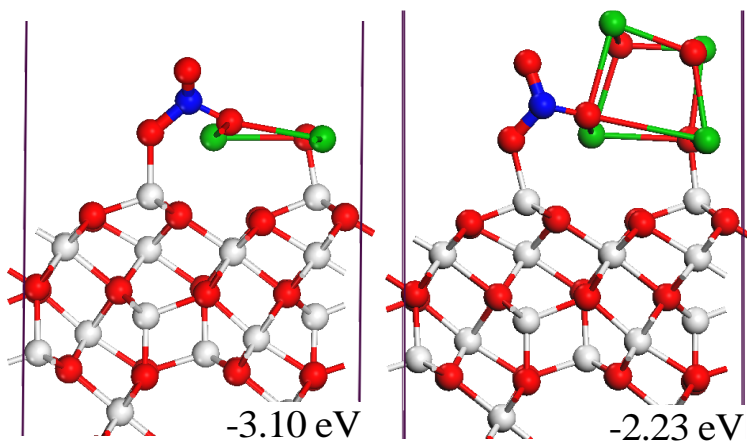


Figure 3.12 Synergistic adsorption of NO_2 on supported (a) $(\text{BaO})_2$ and (b) $(\text{BaO})_4$.

In order to understand the greatly enhanced interaction of NO_2 with the supported $(\text{BaO})_2$ and $(\text{BaO})_4$, we constructed a model where the adsorbed NO_2 molecule only interacts with the $(\text{BaO})_2$ cluster part and another where the NO_2 interacts with the substrate only but in the presence of the $(\text{BaO})_2$ cluster. The structures were shown in Figure 3.13 together with the structure of NO_2 adsorption over the $\gamma\text{-Al}_2\text{O}_3$ support

surface with no presence of BaO. Adsorption energy of the NO₂ molecule at the oxygen atom of the supported (BaO)₂ (Figure 3.13b) yields an adsorption energy of -1.46 eV; on the other hand, an adsorbed unidentate NO₂ molecule with an oxygen bonded to a surface Al in the presence of (BaO)₂, as shown in Figure 3.13c, gives a binding energy of -2.24 eV. The NO₂ adsorption on the bare γ -Al₂O₃ surface in a similar unidentate configuration and obtained an adsorption energy of -1.15 eV (Figure 3.13d). This value is significantly smaller than the adsorption energy of -2.24 eV with the same configuration in the presence of (BaO)₂. These results indicate that there is a synergistic effect between the supported (BaO)₂ cluster and the alumina substrate for NO₂ adsorption: the mere presence of the BaO cluster on the surface greatly strengthens the interaction between NO₂ and the γ -Al₂O₃ surface; at the same time, the NO₂-BaO interaction is enhanced when the BaO clusters are supported by the γ -Al₂O₃ surface, e.g. the adsorption energy of NO₂ on the supported (BaO)₂ cluster (Figure 3.13b) is larger on (BaO)₂ without support (Figure 3.5d). The bridging structure between (BaO)₂ and the substrate surface formed upon NO₂ adsorption (Figure 3.13a) further enhances this effect. However, the strength of synergistic adsorption (NO₂ binds with both support surface and BaO cluster) for supported (BaO)₄ cluster is not as strong as it is for (BaO)₂, implying that adding more BaO layer will weaken the synergy effect. As such, we conclude that the submonolayer BaO dispersed on the γ -Al₂O₃ surface with available substrate Al sites provides strong binding sites for NO₂ adsorption. These strong binding sites may be the active sites for NO_x storage in the NSR catalysts.

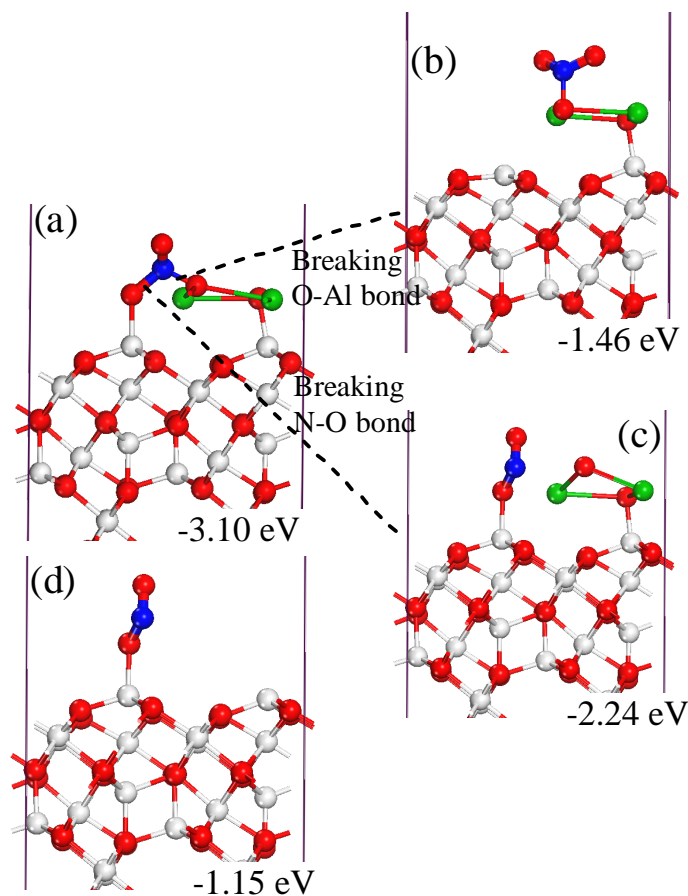


Figure 3.13. Decomposition of (a) NO₂ adsorption on supported-(BaO)₂ into (b) NO₂-BaO interaction and (c) NO₂-support interaction. (d): NO₂ adsorption on clean γ -Al₂O₃ surface.

c. NO₂ Adsorption on γ -Al₂O₃ Supported BaO Clusters with Bigger Unit Cell. In the small unit cell calculations of γ -Al₂O₃ supported BaO, the supported (BaO)₂ clusters formed a BaO strip by linking with its periodic images from the neighboring unit cells, as shown in Figure 3.14a. In order to answer the criticism whether such strong synergistic effect was an artifact of the particular (BaO)₂ structure, we re-examined NO₂ adsorption on γ -Al₂O₃-supported (BaO)₂ with a bigger γ -Al₂O₃ surface unit cell. The number of layers in the slab simulating the γ -Al₂O₃ surface was kept the same as the previous study, but the area of the surface unit cell was doubled, as shown in Figure 3.14b. The increase

in the surface unit cell size reduces the coverage of BaO by half. In the new surface unit cell, the supported $(\text{BaO})_2$ cluster is isolated from its periodic images in the neighboring unit cells. Using this surface unit cell, the adsorption energy of NO_2 over the supported $(\text{BaO})_2$ in synergistic configuration was calculated to be -3.0 eV, very close to -3.1 eV of the previous result. The similar adsorption energies calculated using different sizes of unit cell indicates that the synergistic effect is independent of BaO coverage within the submonolayer regime. The availability of the surface Al site and the unbound oxygen atom at the $\gamma\text{-Al}_2\text{O}_3$ and BaO interface is the key to the formation of the strong binding synergistic structure.

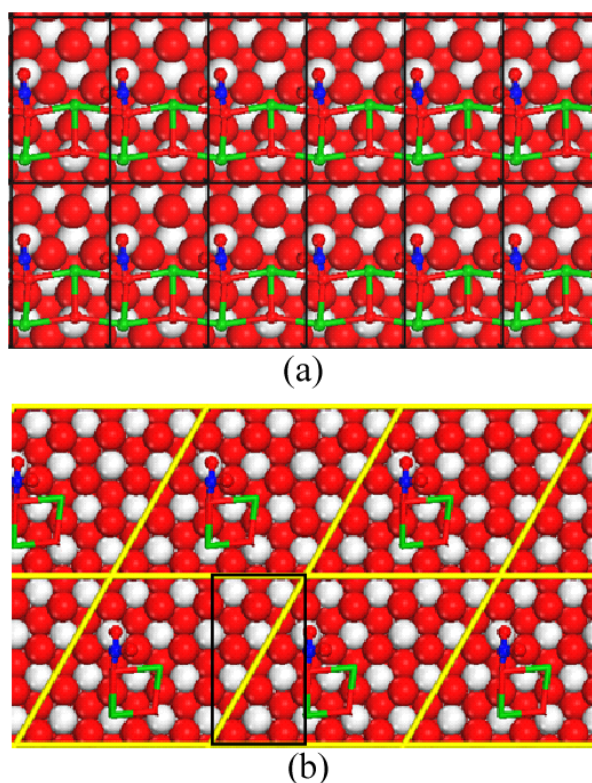


Figure 3.14. Top view of NO_2 adsorption over the $\gamma\text{-Al}_2\text{O}_3$ supported $(\text{BaO})_2$. (a) The small unit cell shown as black rectangular box used in previous study. (b) The big unit cell, shown as the yellow box, used in the present calculations. Reproduced with permission from J. Phys. Chem. C, 2008, 112, 16924. Copyright 2008 American Chemical Society.

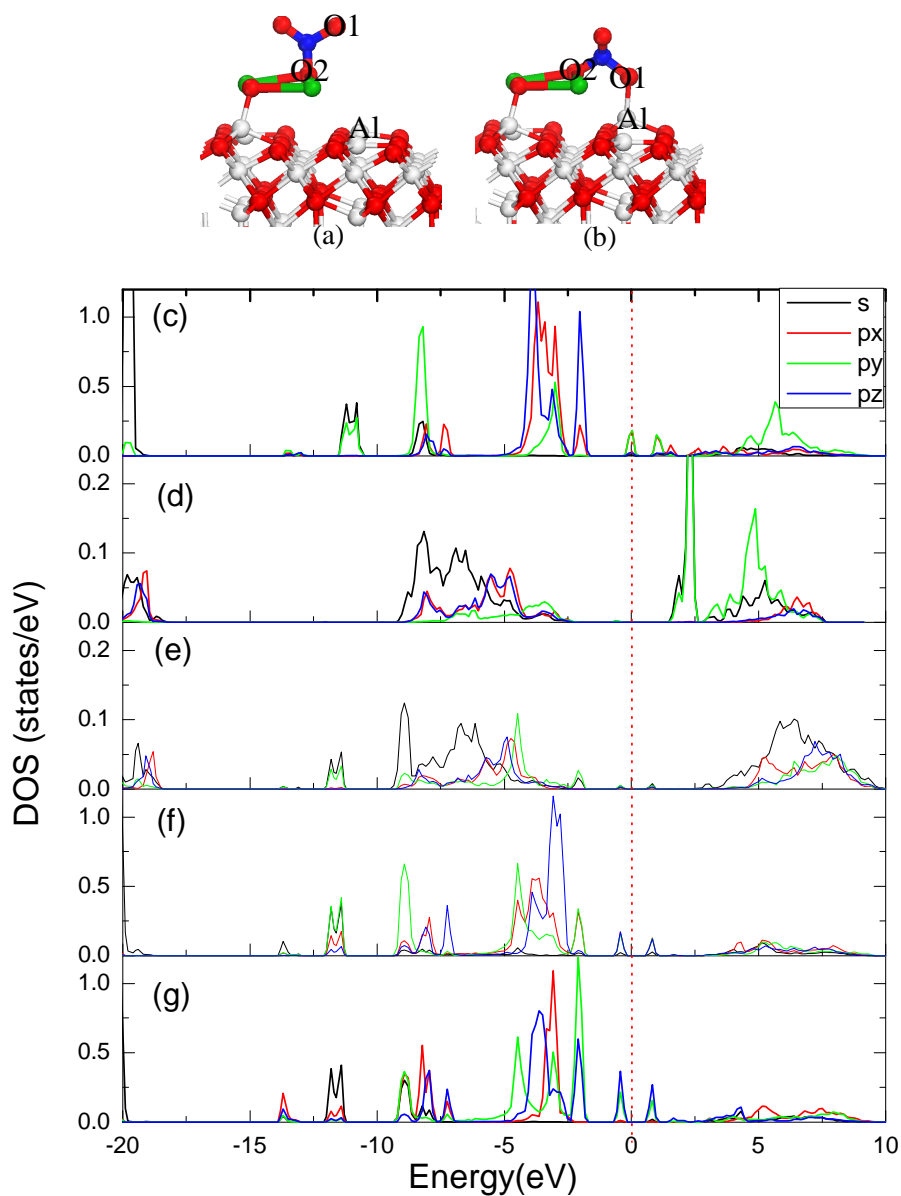


Figure 3.15 (a) NO₂ interacts only directly with supported (BaO)₂. (b) NO₂ interacts only simultaneously with both supported (BaO)₂ and γ-Al₂O₃. (c) PDOS plot of the Al site shown in (a). (d) PDOS plot of the Al site shown in (b). (e) PDOS plot of the O1 shown in (b). (f) PDOS plot of the O2 shown in (b). (g) PDOS plot of the O2 shown in (a). Reproduced with permission from J. Phys. Chem. C, 2008, 112, 16924. Copyright 2008 American Chemical Society.

In order to understand the origin of the synergistic effect for NO₂ adsorption, we compared the local projected density of states (PDOS) of NO₂ only interacting with the supported (BaO)₂ (Figure 3.15a), which will be referred to as BaO-only, with those of

NO_2 interacting simultaneously with $(\text{BaO})_2$ and $\gamma\text{-Al}_2\text{O}_3$, which will be referred to as synergistic (Figure 3.15b). We also numbered three O atoms and labeled the surface Al site in Figure 3.15a,b. Parts c and d of Figure 3.15 show the local PDOS of the O2 atom and the Al site, respectively, in the BaO-only configuration. The PDOS of the Al site and the O1 and O2 atoms in the synergistic configuration (Figure 3.15b) were plotted in parts e, f, and g of Figure 3.15, respectively. The scales of the oxygen PDOS plots are 5 times those of Al atoms. The intensity difference between the O and Al PDOS is a reflection of the ionic nature of Al-O interaction. A comparison of the two Al PDOS plots shows that the p_y -derived states above the Fermi level in Figure 3.15d disappear after the Al site became occupied by the O1 atom, as shown in Figure 3.15e. The p_y -derived states become dominant in the energy range of -5 to -2.5 eV, as shown in Figure 3.15e. These states were clearly a result of Al-O1 bond formation in the synergistic configuration shown in Figure 3.15b. The s-states of Al also contribute to bonding with the O1 atom in the synergistic configuration, as indicated by the peak at 8.5 eV. The binding of O1 on the Al site changes not only the PDOS of the O1 and Al atoms but also the PDOS of the O2 atom, as shown in Figure 3.15c,g. The states below -7 eV as well as those small peaks around the Fermi level were mainly results of covalent bonding with the N atom. The strong p_y -derived states above Fermi level in BaO-only configuration (Figure 3.15c) almost disappeared in the synergistic configuration (Figure 3.15g). The states in the energy range of -5 to -2.5 eV are a result of interaction with the neighboring Ba atoms.

We further compared the atomic Bader charges of NO_2 in the BaO-only and synergistic configurations. The Bader charges on N and O atoms as well as the binding O and Al sites are summarized in Table 3.1. The change of Bader charge on Ba and other O

and Al atoms is negligible and was not included in the table. The charges in Table 1 show that allowing O1 to interact with the surface Al site makes the NO₃ fragment more negatively charged. There are some charge redistributions within the fragment, but the charge transfer occurs primarily on the O1 atom. These results indicate that acidic Al site enhances the binding of the adsorbed NO₂ on the supported (BaO)₂ by donating its charge.

Table 3.1: Atomic Bader Charges in BaO-Only (Figure 3.15a) and Synergistic (Figure 3.15b) Configuration^a. Reproduced with permission from J. Phys. Chem. C, 2008, 112, 16924. Copyright 2008 American Chemical Society.

	BaO-only	Synergistic
N	+0.62	+0.60
O1	-0.68	-0.92
O2	-0.84	-0.78
O3	-0.66	-0.60
Al	+0.66	+0.61

^a Refer Figure 3.15 for numberings of atoms.

We also compared the atomic Bader charges of NO₂ in the BaO-only configuration with NO₂ interaction with a bare (BaO)₂ cluster in a similar configuration. On BaO-only, the charges on NO₂, (BaO)₂, and γ -Al₂O₃ support are -0.72, +0.87, and -0.15 |e|, respectively. In the case of NO₂ interacting with bare (BaO)₂, the charges on NO₂ and (BaO)₂ are -0.33 and +0.33 |e|, respectively. These results demonstrated that the presence of γ -Al₂O₃ as support facilitated an electron transfer from (BaO)₂ to both the adsorbed NO₂ molecule and γ -Al₂O₃, resulting in a positively charged (BaO)₂ sandwiched between the negatively charged NO₂ molecule and the γ -Al₂O₃ slab. The γ -Al₂O₃ surface enabled the charge redistribution although it does not have direct contact with the adsorbed NO₂ molecule.

We then analyzed the charge distribution for NO_2 interacting with $\gamma\text{-Al}_2\text{O}_3$ support in the presence of the $(\text{BaO})_2$ cluster but not directly in contact with the cluster. Our results showed that $(\text{BaO})_2$ lost 0.52 |e| upon NO_2 adsorption although NO_2 does not have direct contact with $(\text{BaO})_2$. After $(\text{BaO})_2$ was replaced by a cubic $(\text{BaO})_4$, the overall charge loss by $(\text{BaO})_4$ was reduced to 0.31 |e|. These results indicated that the supported BaO clusters act as an electron donor, enhancing NO_2 interaction with the $\gamma\text{-Al}_2\text{O}_3$ support. In other words, the supported BaO clusters enhance the electron donating ability of the $\gamma\text{-Al}_2\text{O}_3$ support and, therefore, the Lewis basicity of the support.

The present study addressed some important aspects of the NSR catalysis: the effect of BaO morphology and $\gamma\text{-Al}_2\text{O}_3$ support on NO_2 adsorption. We showed that the morphology of BaO as well as the interaction of BaO with the support will play important roles in stabilizing the active species and modifying the interaction of other gases with the surface. NSR catalysis also involves many other aspects such as the existence of other gaseous species in the exhaust stream and operating conditions. Competitive adsorption of different gases on BaO and other alkaline earth metal oxides have been examined.^{68,99} Furthermore, the coupling between the redox sites and the storage sites will be critical to the overall de- NO_x efficiency.^{78,100} All these issues need to be addressed before a more complete understanding of the NSR catalysis can be developed.

3.4. Conclusion

First principles density functional theory calculations have been used to characterize NO_2 adsorption on BaO surfaces, unsupported and $\gamma\text{-Al}_2\text{O}_3$ supported BaO clusters. Our results showed that the adsorption energy of NO_2 depends strongly on the morphology of

BaO and the existence of defects. On the stoichiometric BaO, the low-coordinate sites are more flexible for NO₂ adsorption, resulting in stronger NO₂ bindings. NO₂ adsorption at the edge O sites of the clusters and the stepped surface resulted in a NO₃^{δ-} species. Furthermore, the electronic properties of the BaO substrates were found to have more dramatic effect on NO₂-BaO interaction. On the non-stoichiometric BaO clusters and surfaces, the adsorption energy of NO₂ is much greater than on the stoichiometric clusters and surfaces, up to -4.09 eV for NO₂/Ba₁₄O₁₃.

We also demonstrated that the γ -Al₂O₃ support is critical for NO_x storage. On one hand, the support surface alters the electronic character of the supported BaO cluster, thus affect the NO₂ adsorption configuration and energy of the BaO. On the other hand, a BaO cluster covered over the γ -Al₂O₃ support modifies the acidity of the top layer cation (Al) sites, therefore, the reactivities of the support surface sites are enhanced. The interface where the adsorbed NO₂ can interact with both BaO and γ -Al₂O₃ provides the strongest binding towards NO₂. However, the synergistic effect of enhancing the adsorption of NO₂ was weakened by adding an extra BaO layer on the supported (BaO)₂: the adsorption energy of NO₂ on the supported (BaO)₄, of which the configuration is in the form of two layers of (BaO)₂, was reduced to -2.23 eV from -3.10 eV on the supported (BaO)₂. We therefore propose that a highly dispersed submonolayer BaO will be the most effective for NO_x storage in a NSR catalyst.

CHAPTER 4
ELECTRONIC SHELL EFFECT ON REACTIVITY OF SMALL METAL CLUSTERS
—EXAMPLES OF H₂ DESORPTION ON MAGNESIUM CLUSTERS

4.1. Introduction

The study of H₂ dissociation over Mg clusters reveals the effect of electronic structures on the reactivities of the small metal clusters. The reaction was studied as an important step in using magnesium as hydrogen storage material.

Although magnesium dihydride has for long been recognized as one of the most attractive hydrogen storage materials candidate due to its low cost and high hydrogen storage capacity (7.6 wt%), its actual onboard application is limited by the high desorption temperature and the slow H₂ adsorption and desorption kinetics. A DFT calculation using PBE functional predicted an activation barrier of ~1.05 eV for H₂ dissociation over the Mg (0001) surface¹⁰¹. This relatively high threshold energy is responsible for the slow H₂ adsorption kinetics over the bulk surface although the phase transition between Mg and MgH₂ can also be rate-limiting. As the research focus of hydrogen storage swings from demonstrating possibilities to improving commercial viability, lots of effort has been made to decrease the operation temperature and increase the adsorption/desorption rates of Mg-based system. Alloying and doping magnesium with other metals¹⁰²⁻¹⁰⁶ or metal oxide¹⁰⁷⁻¹⁰⁹ can actually improve the kinetics of and increase the rate hydrogen sorption, however, this sacrifices hydrogen storage capacity due to the added weight of the doped metal and oxide. So the intuitive ideal solution to the problem would be modifying the thermodynamics and kinetics of H₂ sorption over Mg/MgH₂ without the addition of extra component. Ball milling technique effectively

reduced Mg grain size and increased H₂ sorption rates. However, the enhanced rate is solely related to surface area enlargement and diffusion length decrease while the grain size of particles obtained by this technology is still not small enough to change thermodynamics of the system, the H₂ desorption process still requires high temperature (~300 °C at 1 bar H₂).^{110,111}

Recently, it has been demonstrated that when the crystal grain size is down to about 1.3 nm, the hydrogen desorption energy decreases significantly, so that, thermodynamically speaking, the hydrogen desorption on small size MgH₂ can occur at lower temperature, e.g. 200 °C for 0.9 nm crystalline.¹¹² In a work by Li et al.¹¹³, Mg nanowires were demonstrated to have improved H₂ sorption kinetics. For example, the nanowires with diameter of 30-50nm can achieve 7.60 wt% uptake of hydrogen within 30 min at around 300 °C. The accelerated sorption rates should be related to the low sorption activation energy barriers. Therefore, in this chapter, we investigated the H₂ dissociation energy barriers over Mg clusters. The aim is to provide the insight into the difference between H₂ sorption kinetics over Mg surfaces and small clusters.

4.2. Methodology

The structure optimizations of the Mg₉, Mg₉²⁺, Mg₉²⁻, Mg₁₀ and Mg₁₀²⁺ clusters and the reactions (H₂ dissociation over the clusters) were carried out using the GAUSSIAN 03 package¹¹⁴. The DFT method with both the B3LYP and the PBE^{88,115,116} forms of exchange/correlation energies were used. The choice of basis sets are 6-31+g(d,p). In the discussions of the results, we refer to the GAUSSIAN calculation results with PBE functional unless otherwise noted. The structures of clusters were optimized until the energies were minimized to the GAUSSIAN default convergence criteria. The transition

states were located by minimizing the force of the structures to the saddle points. Then frequency calculations of those optimized structures were performed to confirm that they are indeed the transition states corresponding to H₂ dissociation.

The calculations of the Mg₉, Mg₁₀ and Mg₁₀²⁺ clusters were also carried out using the DFT implementation program package the VASP code¹¹⁷ for comparison and supporting purpose. The VASP code was also used to calculate H₂ dissociation over the Mg(100) and (110) surfaces. In the VASP calculations, the exchange-correlation energy was evaluated by the PBE⁸⁸ functional. The interaction between ions and electrons was described using the projector augmented wave method,^{87,118} and a plane wave basis set with a cutoff energy of 450 eV was used to expand the wavefunction of valence electrons. The atomic structures were relaxed using spin-polarized conjugate-gradient algorithm until the forces on the unconstrained atoms were less than 0.005 eV/Å. The transition states were located using nudged elastic band method and confirmed by frequency calculations. In the calculations of Mg clusters, there were at least 20 Å separations in all three directions (*a*, *b* and *c*) between clusters in neighboring unit cells to avoid the interactions. The cluster structures were subjected to relaxation without constraints. The Mg(100) and (110) surfaces were cleaved from the relaxed bulk Mg structure and were simulated with six and four layers slabs, respectively. Separations of at least 10 Å in *c* directions were inserted between neighboring cells to minimize the interactions along these directions between periodic images. The bottom layers of the surface slabs were kept frozen at the respective cleaved-from-bulk positions whereas the top layers together with the two hydrogen atoms were allowed to relax. For the cluster calculations, Γ -point was used for Brillouin zones. $6 \times 3 \times 1$ and $4 \times 4 \times 1$ K-point

meshes generated with the Monkhorst-Pack scheme were used to sample the Brillouin zones for surface (100) and (110), respectively.

4.3. Results & Discussion:

4.3.1. Structures of Mg_9 , Mg_9^{2+} , Mg_9^{2-} , Mg_{10} and Mg_{10}^{2+} Clusters. The most stable structure of Mg_9 is a six-atom triangular prism core with three atoms attached to each side square of the triangular prism (Figure 4.1a). The same structure was also reported previously in a work by Lyalin *et al.*¹¹⁹ The structures of Mg_9^{2+} and Mg_9^{2-} clusters were calculated by relaxing the optimized Mg_9 cluster with +2 and -2 charges, respectively. These two structures were shown in Figure 4.1 b and c. Comparing these three 9-atom clusters, we found that the more electron the cluster has, the more closely packed the triangular prism is. For example, the average bond length of the triangles of the triangular prism in the Mg_9^{2+} cluster is ~ 4.2 Å, much larger than that of the neutral Mg_9 cluster (3.2 Å) and the Mg_9^{2-} cluster (3.06 Å). The calculated HOMO-LUMO band gaps were 0.73, 0.90 and 0.81 eV for Mg_9 , Mg_9^{2+} and Mg_9^{2-} , respectively. Adding one atom to the Mg_9 triangle cap, we obtain the Mg_{10} structure shown in Figure 4.1d. The Mg_{10}^{2+} cluster was calculated by relaxing the Mg_{10} cluster with two positive charges shown in Figure 4.1e. The HOMO-LUMO band gaps for these two structures are 1.25 eV for Mg_{10} and 0.92 eV for Mg_{10}^{2+} .

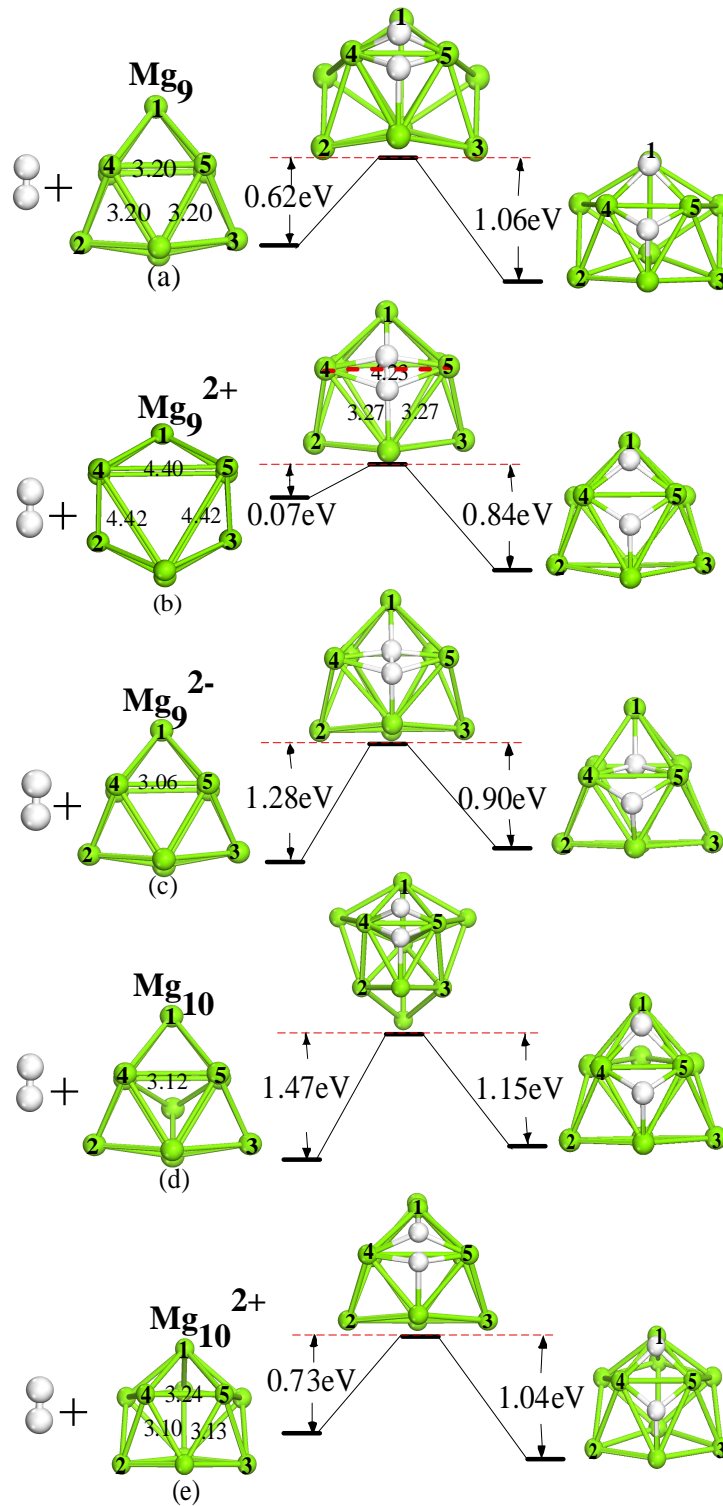


Figure 4.1. Energy diagram of H₂ adsorption over (a) Mg₉, (b) Mg₉²⁺, (c) Mg₉²⁻, (d) Mg₁₀, and (e) Mg₁₀²⁺ clusters. For clarity, five of the Mg atoms were labeled in initial state, transition state and final state structures (green: Mg; white: H).

For small metal clusters consisting of less than hundred atoms, a mean field potential can be introduced to calculate the energy level of the system where every atom and electron counts. This is the base of the Jellium model, which has successfully explained the unusual stabilities of the Na clusters with closed electronic shells¹²⁰, i.e., Na clusters consisting of 2, 8, 20, 40, ...atoms have higher binding energies due to the successive complete filling of electron shells. Such clusters were known as the magic clusters. Experimental evidence of such concept is the observation of high peaks corresponding to those magic clusters in mass spectrum.¹²¹ The stabilities of certain divalent and trivalent clusters, where each atom contribute two and three electrons, respectively, can also be explained from the electronic shell closure rules^{121,122}. For example, in the work of Doppner etc.¹²¹, the neutral Mg₁₀ and doubly positive-charged Mg₁₁ clusters both contain 20 electrons and have enhanced stabilities compared with their corresponding uncharged and doubly charged neighbors. Applying the same rule, Mg₉²⁻ has a closed-shell (9 Mg atoms × 2 valence electron/atom + 2 e⁻ = 20 e⁻) thus should have extra stability. Because the binding energies of the three clusters, Mg₉, Mg₉²⁺ and Mg₉²⁻, are not directly comparable due to the fact that they are differently charged, we compare the HOMO-LUMO gaps of the clusters instead of binding energies as indication of their relative stabilities. We found that the band gap of the closed-shell Mg₉²⁻ (0.81 eV) is larger than that of Mg₉ (0.73 eV) which is two electrons shy than the magic number. This obeys the magic rules that the closed shell clusters are more stable thus having larger band gaps. However, the Mg₉²⁺ cluster is an exception—the band gap of Mg₉²⁺ is 0.90 eV, larger than the other two 9-atom clusters which cannot be explained by the magic rule. For the two 10-atom clusters, our results also follow the magic rule that the Mg₁₀ is the close-

shell cluster and its band gap of 1.25 eV is larger than that of the Mg_{10}^{2+} cluster (0.92 eV).

4.3.2. H_2 Dissociation over Mg_9 , Mg_9^{2+} , Mg_9^{2-} , Mg_{10} and Mg_{10}^{2+} Clusters. To calculate the transition states, we first used the nudged elastic band (NEB) method implemented in VASP to calculate the transition states of H_2 dissociation on the Mg_9 , Mg_{10} and Mg_{10}^{2+} clusters. Those transition state structures were then used as the initial input structures for the GAUSSIAN calculations and allowed to be optimized to the saddle points. These three transition state structures also provided prior knowledge of the transition state structures of such systems. Based on this information, the initial structures of the transition states of H_2 dissociation over the Mg_9^{2+} and Mg_9^{2-} clusters were constructed and subjected to optimize to their corresponding saddle points. For comparison purpose, the H_2 dissociation locations on all clusters were chosen to be very similar, i.e. over the Mg4-Mg5 bridging bond (Figure 4.1). The activation energies were calculated using:

$$\Delta E_{act} = E_{TS} - (E_{cluster} + E_{H_2}), \quad (4.1)$$

where E_{TS} , $E_{cluster}$ and E_{H_2} are the energies of the transition state, the initial Mg cluster and a gas phase H_2 molecule, respectively. ΔE_{act} calculated using both GAUSSIAN and VASP were reported in Table 4.1.

Table 4.1. H₂ dissociation energy barrier (eV) over Mg clusters calculated using Gaussian with both B3LYP and PBE functional, as well as using VASP with PBE functional.

	# of electrons of the cluster	# of electrons of the transition state	ΔE_{act} (Gaussian,B3LYP)	ΔE_{act} (Gaussian,PBE)	ΔE_{act} (VASP, PBE)
Mg ₉	18	20	1.03	0.62	0.61
Mg ₉ ²⁺	16	18	0.73	0.07	
Mg ₉ ²⁻	20	22	1.37	1.28	
Mg ₁₀	20	22	1.66	1.47	1.64
Mg ₁₀ ²⁺	18	20	1.15	0.73	0.77

As shown in Table 4.1, although ΔE_{act} calculated using different computational codes and functionals have different absolute values, the relative orders of the values for different clusters within each method are consistent. Note that for the same cluster, the activation energies calculated using GAUSSIAN with PBE and using VASP with PBE are very similar, while the results using GAUSSIAN with B3LYP is much higher than the former two, for example, the ΔE_{act} of the Mg₉²⁺ cluster calculated using B3LYP is 0.66 eV higher than the PBE result. Therefore, the choice of the functional significantly affects the calculated energy barriers. However, comparing the values calculated by the same method, the ΔE_{act} of the Mg₉²⁻ and Mg₁₀ clusters are consistently the two highest among all five clusters and the ΔE_{act} for the Mg₉²⁺ cluster is significantly smaller than all the other clusters. Since the local steric environments for H₂ dissociation on all clusters are very similar, the obvious difference of ΔE_{act} of different clusters should be attributed to the relative stabilities of the reactant Mg clusters and the transition states, which are determined by the difference of their electronic structures. From herein, we only compare the activation energies of different clusters calculated using Gaussian/PBE.

When a hydrogen molecule approaches and dissociates over a magnesium cluster, the electronic shell structure of the reaction transition state and final state differs from that of the original magnesium cluster. According to the electron counting rule developed for Al_nH_m clusters¹²³, when a hydrogen atom is at the bridge bonded Al–Al position, its electron would become delocalized and should be counted in the electron shell of the metal-hydrogen cluster entity. Since in the transition state structures of hydrogen dissociation, both hydrogen atoms sit on bridge magnesium bonds, the two electrons from the hydrogen atoms should be both counted for the electron shells. Accordingly, the hydrogen dissociation transition states $\text{TS}_{\text{Mg}_{10}}$ and $\text{TS}_{\text{Mg}_9(2-)}$ both have 22 shell electrons. At the same time, the initial structures of both Mg_{10} and Mg_9^{2-} clusters are both very stable due to the electron closures, therefore, changing electron shell from 20 electrons (closed) to 22 electrons (open) by adding a hydrogen molecule is not favored, thus the ΔE_{act} for these two are expected to be high. On the other hand, the Mg_9 and Mg_{10}^{2+} clusters are both two electrons shy from closed shells. Adding two hydrogen atoms to the cluster, the transition state structures of hydrogen dissociation complete closed electronic shells since the electrons from two hydrogen atoms are both counted as delocalized electrons. Therefore, opposite to H_2 dissociation on the Mg_{10} and Mg_9^{2-} clusters discussed above, the reactions on Mg_9 and Mg_{10}^{2+} are from open to closed electron shells. Because the closed-shell transition states TS_{Mg_9} and $\text{TS}_{\text{Mg}_{10}(2+)}$ have enhanced stabilities compared with their corresponding reactant clusters, the height of the potential barrier that the system needs to overcome is reduced. This explains why the ΔE_{act} of 0.62 and 0.73 eV for Mg_9 and Mg_{10}^{2+} , respectively, are much lower than Mg_{10} and Mg_9^{2-} clusters, as well as Mg(0001) surface.

The reaction of a hydrogen molecule dissociates over a Mg cluster is a simultaneous process of H-H bond elongating/splitting and hydrogen adsorption on the magnesium cluster. The H-H elongation normally costs energy, thus it raises the energy of the system and contributes to the increase the activation energy. The latter involves the two hydrogen atoms joining the magnesium cluster skeleton accompanied by the structure adjustment of the original magnesium cluster to adopt the newly added two atoms. This can either stabilize or destabilize the system depending on the interaction between the two hydrogen atoms and the magnesium cluster. Accordingly, we decompose the ΔE_{act} into two parts of energies—the H-H elongation/splitting energy and the hydrogen adsorption energy. The H-H elongation/splitting energy cost was calculated by subtracting the energy of a gas phase hydrogen molecule from the energy of two hydrogen atoms at the distance of the transition state H-H bond length. These energies are reported in Table 4.2. Depending on the transition state H-H bond length, the elongation energy on different clusters varies—the longer the H-H bond length is in the transition state structure, the larger the elongation energy is. The absolute value of the imaginary H-H stretch frequency of the transition state also increases as the H-H distance of the transition state and the splitting energy increase. Subtracting the H-H elongation energy cost from ΔE_{act} yields the adsorption energy, e.g. the stabilizing/destabilizing energy by forming the magnesium cluster and hydrogen entity. When this adsorption energy is positive, it will be added up to the H-H elongation energy and raise the activation energy of H₂ adsorptive dissociate over the cluster; however, if the adsorption energy is negative, it will compensate the H-H elongation energy cost and thus decrease the activation energy. The adsorption energies are also reported in Table 4.2. The smaller

this energy is, the more stabilized the cluster structure becomes after the addition of two hydrogen atoms. The adsorption energy calculated as such should be a good indication of the stability change caused by the interaction between the magnesium cluster and the newly added two hydrogen atoms, thus the values of this energy follow the magic rule. For example, the adsorption energies for Mg_9 and Mg_{10}^{2+} , -0.62 and -0.75 eV, respectively, are lower than Mg_{10} and Mg_9^{2-} . This is, again, because for the former two the originally 18-electron clusters were greatly stabilized by the addition of two hydrogen atoms; while for the latter two clusters, the electron shells changed from 20-electron to 22-electron, which is not a thermodynamically favored. Especially for the Mg_9^{2-} , besides the unfavorable electronic shell structure change from closed to open, the added electron from the hydrogen atoms entered an anti-bonding orbital. Thus, the adsorption energy for this cluster is the highest, with a positive energy of 0.19 eV.

Table 4.2. H_2 dissociation adsorption activation energies (eV) decomposed to H-H splitting energy cost and pure adsorption energies. Imaginary frequencies (cm^{-1}) of H-H splitting were also reported. All results are PBE calculations.

	Mg_9	Mg_9^{2+}	Mg_9^{2-}	Mg_{10}	Mg_{10}^{2+}
ΔE_{act}	0.62	0.07	1.28	1.47	0.73
H-H splitting energy cost	1.24	1.01	1.09	1.61	1.48
Adsorption energy	-0.62	-0.94	0.19	-0.14	-0.75
H-H frequency	-1086	-741	-815	-1355	-1105

The Mg_9^{2+} cluster has 16 electrons in the valence shell. Adding one hydrogen molecule to the Mg_9^{2+} cluster makes the transition state an 18-electron structure. The reaction over the Mg_9^{2+} cluster is an open shell (reactant) to open shell (transition state) process. Neither reactant nor product cluster structure has extra stability by completing electronic shell closure. However, the activation energy of 0.07 eV is exceptionally low,

indicating the reaction is almost barrierless. This is probably because the 18-electronic shell structure of the transition state is closer to the closed shell compared with the reactant. As the electronic shell structure of a cluster getting close to closure, the stability of the cluster increases. Thus the reaction is very readily to occur so that the electrons from the hydrogen can help stabilizing the structure of the cluster.

Table 4.3. Band gaps (eV) of magnesium clusters and their corresponding transition states.

	Mg ₉	Mg ₉ ²⁺	Mg ₉ ²⁻	Mg ₁₀	Mg ₁₀ ²⁺
Band gap of cluster	0.73	0.90	0.81	1.25	0.92
Band gap of transition state	1.23	2.12	0.54	0.90	1.36

The band gaps of the transition states of H₂ dissociation on the five clusters were reported in Table 4.3. The two 22-electron structures TS_{Mg₉(2-)} and TS_{Mg₁₀} have smaller band gaps (0.54 and 0.90 eV, respectively) than the two 20-electron structures TS_{Mg₉} (1.23 eV) and TS_{Mg₁₀(2+)} (1.36 eV). Again, the exception to the magic rule here is the transition state of Mg₉²⁺ — the 18-electron transition state TS_{Mg₉(2+)} has an remarkable large band gap of 2.12 eV. Since ΔE_{act} was calculated by $E_{TS} - (E_{cluster} + E_{H_2})$ and the E_{H_2} term for each cluster is the same, the value of ΔE_{act} is actually determined by the value of $(E_{TS} - E_{cluster})$. Base on the fact that both energy and band gap are good indication of the stability of small clusters, the value of $(E_{TS} - E_{cluster})$ should be proportional to the band gap (BG) difference between the transition state and initial cluster ($BG_{TS} - BG_{cluster}$). Therefore, when we plot out $(BG_{TS} - BG_{cluster})$ vs. ΔE_{act} of each cluster, the ΔE_{act} is linear to $(BG_{TS} - BG_{cluster})$ as clearly shown in Figure 4.2.

For the Mg_9^{2-} and Mg_{10} clusters, because the products have smaller band gaps than their corresponding reactants, their $(BG_{TS} - BG_{cluster})$ terms are negative. This implies the transition state cluster entities are less stable than the reactants, in good agreement with the prediction of the magic rule. As a result, for such reaction to occur the systems need to overcome large energy barriers. For cluster Mg_9 , Mg_{10}^{2+} and Mg_9^{2+} , the transition states are more stable than reactants ($BG_{TS} - BG_{cluster} > 0$), ΔE_{act} are lower. We also plotted the H_2 dissociation reaction energy of each cluster vs. the corresponding ΔE_{act} in Figure 4.2. Clearly, the activation energy and the reaction energy do not exactly follow the linear free energy relationship, e.g. the Mg_9^{2+} has higher reaction energy but lower activation energy than Mg_{10} .

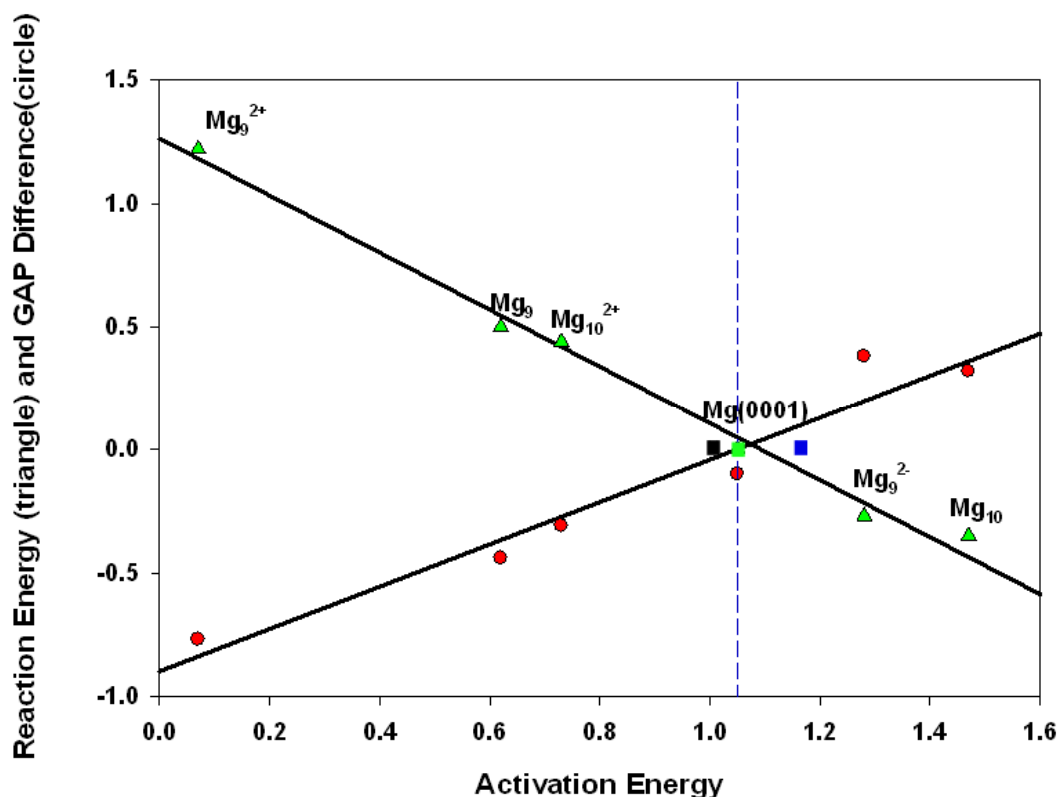


Figure 4.2. Activation energy vs. band gap difference between the transition state and the reactant of the Mg clusters/surfaces.

4.3.3. Comparison of H₂ Dissociation over Mg Clusters and Surfaces. As discussed above, the very different reactivities of the Mg clusters with similar sizes depend on the electronic shell structure changes from the initial to the final state. As we can imagine, these changes are only significant for small metal clusters that can be described with Jellium model. For the H₂ dissociation occurring on surfaces or clusters with larger sizes, the adsorption of H atoms on Mg species is not very strong and the structural adjustment of Mg to adapt H would be relatively localized, thus, the H–H splitting energy cannot be properly compensated. The transition states of H₂ dissociation over Mg(100) and (110) are shown in Figure 4.3. The ΔE_{act} of 0.98 and 1.16 eV, respectively, are very similar to the ΔE_{act} of 1.05eV on (0001).

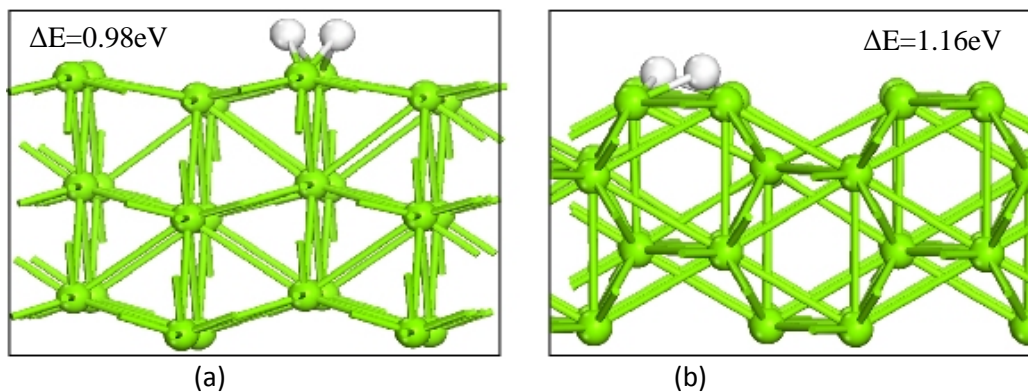


Figure 4. 3. Transition states of hydrogen dissociation over the (a) Mg(100) surface and (b) Mg(110) surface.

Furthermore, the reaction occurring on Mg surfaces is too localized to bring any significant change to the overall band gap of the system. Thus the $(BG_{TS} - BG_{cluster})$ approximately equals zero. Assuming $BG_{TS} - BG_{cluster} = 0$ for these three surfaces, we

marked the data points in green (0001), black (100) and blue (110) squares, respectively, in Figure 4.2. All three points are converged nearly on the linear data line at approximately 1.0–1.1 eV. Furthermore, the interaction between the Mg surfaces and the hydrogen atoms at the transition state is so weak, that the energy cost of the H-H elongation/splitting cannot be compensated. Thus ΔE_{act} on the Mg surfaces are relatively high comparing with some of the clusters where the adsorption energy of hydrogen on Mg clusters lowers the activation energy.

Furthermore, our results demonstrated that the kinetics of H₂ dissociation over small Mg clusters, to which the magic rule applies, is very different from that of the surfaces.

4.4. Conclusions:

First principles density functional theory was used to study the H₂ dissociation over selected Mg clusters. We have demonstrated the reaction energy barrier of hydrogen dissociation on these clusters highly depends on the electronic structure of the initial bare cluster and the transition state cluster entity (magnesium with hydrogen attached). For cluster Mg₉ and Mg₁₀²⁺, the electronic structures change from open shell initial states to closed shell transition states, so the activation energies are relatively lower than for cluster Mg₉²⁻ and Mg₁₀, of which the electron shells change from closed (initial state) to open (transition state). This follows the magic rule that the clusters with closed electronic shell have extra stability than the open shell. However, the Mg₉²⁺ cluster is exceptionally stable and the hydrogen dissociation barrier over the cluster is expectedly low, which is not discussed in the magic rule. More importantly, we demonstrate that some of the clusters, compared with surfaces, have very high reactivities and completely different

kinetic properties toward H₂ dissociation, which might shed light on tailoring the materials for better usage of hydrogen storage.

CHAPTER 5

ORIGIN OF SUPPORT EFFECTS ON THE REACTIVITY OF CERIA CLUSTER

5.1. Introduction

Metal oxides are commonly used as catalyst supports in a variety of commercial heterogeneous catalytic processes, including the conversion of hydrocarbon and emission control.^{124,125} Metal oxide also acts as active catalysts and/or promoters in many reactions.¹⁴ Catalysts comprised of an active metal oxide dispersed on the surface of another metal oxide support are used widely.^{14,126} In these catalysts, the supporting oxides and the dispersed oxides may exhibit very different physical and chemical properties from their corresponding bulk counterparts. The geometric structure and the variable oxidation states of metal in the active oxide, as well as the local environment where the reaction takes place, control the overall catalytic performance.¹²⁷⁻¹³¹ In this regard, the loading of active oxide, the nature of the supporting oxide, and the preparation method all contribute to the activity of the catalyst. For example, it was well documented that the turn-over frequency of the selective oxidation of methanol to formaldehyde on metal oxide supported vanadia/molybdena can be greatly affected by the support^{51,132-139}. In the mean time, the loading of the dispersed active metal oxide determines the number of active sites since the coverage of the dispersed phase is in the range of submonolayer (< 100%). Establishing a relationship between the reactivity of the dispersed metal oxide catalysts on different oxide substrates by investigating the oxide cluster and overlayer on the different support oxides is key to understand and design more efficient catalysts. Unfortunately, unlike the very well studied metal clusters supported on metal oxide

systems^{12-17,140-148}, the supported oxide catalysts are not as well understood as the supported metal catalysts due to the challenges in manipulating the dispersion oxide particles and characterizing the oxide overlayers.

Ceria-based catalysts have attracted enormous interest because of their various applications in heterogeneous catalysis such as automobile exhaust treatments and oxidative dehydrogenation of hydrocarbons.^{142,149-153} The unique capability of cerium that it adapts its oxidation states under different environments, makes ceria not only a good support for transition metals, but also an active component in many practical catalysts.^{149,150,154} However, pure ceria is not suitable for the dual functionalities in those catalysts because of the rapid sintering, poor thermal stability, and high reduction temperature.^{2,155} A second metal oxide, such as ZrO_2 or $\gamma\text{-Al}_2\text{O}_3$, was generally added in ceria-based catalysts.¹⁵⁶⁻¹⁵⁹ The addition of another metal oxide is expected to enhance the dispersion and resist the sintering, as well as improve the redox property of CeO_2 .^{2,155,160} Numerous experimental investigations have attempted to follow the structural transformation and to elucidate stability of the oxygen vacancy in the mixed oxides.^{132,153,156-159,161-166} However, to establish a structure-property relationship for the complex mixed oxide systems on the molecular level is still prohibited.¹⁴

Experimentally, it has been demonstrated that the loading of the ceria species and the nature of the support result in different reactivity of the catalyst. For example, the dispersion of the CeO_2 entities in an alumina-supported ceria catalyst was found to depend upon the interaction between CeO_2 and the underlying alumina support.¹⁵⁸ In the range of 1 ~ 39 wt% CeO_2 , two general types of CeO_2 structures have been observed.¹⁵⁸ At low CeO_2 loadings, CeO_2 particles are highly dispersed on the support as two-

dimensional (2D) patches. As the CeO₂ content increases, three-dimensional (3D) crystalline CeO₂ particles form and grow at the expense of the 2D CeO₂ patches. More importantly, different redox properties were observed for the 2D and 3D CeO₂. For example, re-oxidizing the Ce sites of the reduced 2D CeO₂ patches was found to be difficult as observed by *electron paramagnetic resonance (EPR)*.¹⁵⁸ For CeO₂-ZrO₂ systems, most previous studies indicated that mixed Ce_xZr_{1-x}O₂ solid solutions form.^{155,159,163,166-168} The redox properties of Ce_xZr_{1-x}O₂ are strongly dependent upon the structure and composition of the active phase. Due to the limitations of current surface science techniques, the activity of the catalyst is measured as an average over the entire CeO₂-ZrO₂ sample. Consequently, the origin of the improved redox property by adding ZrO₂ to the system is not clear.^{166,168} It has been suggested that the enhanced redox properties relates to the composition of the mixed CeO₂-ZrO₂ nanodomain.^{166,168} The nanoscale heterogeneity derived from the local composition and structure may play an important role in determining the support and promotion effects of ZrO₂.^{166,168} Putna et al. investigated CO oxidation on the CeO₂ film supported by the polycrystalline ZrO₂ and α -Al₂O₃ substrates.¹⁶² They reported that the CeO₂ film over the ZrO₂ substrate was highly reducible and much more reactive towards CO oxidation than the α -Al₂O₃ substrates. Furthermore, there was no evidence of forming a mixed CeO₂-ZrO₂ phase. The observed enhancement in activity was rationalized by the improved reducibility of CeO₂ film since ZrO₂ was buried under the CeO₂ film at the reaction conditions.¹⁶² These authors also suggested that the support effects of ZrO₂ might simply be explained by promoting the formation of small, incoherently dispersed CeO₂ islands.¹⁶²

To better understand of the origin of support effects on the CeO₂ catalyst, CO adsorption and oxidation over the oxide-on-oxide model catalyst, i.e. a stoichiometric Ce₂O₄ cluster (as the active oxide phase) supported on the reducible ZrO₂ and the irreducible γ -Al₂O₃ substrates was studied using first principles density functional theory (DFT) method. We demonstrated the distinctive effects of the irreducible and reducible supports on the reactivity of supported Ce₂O₄ clusters toward CO and CO₂ and analyzed the origin of the differences.

5.2 Methodology

All the calculations were carried out using the VASP code,⁸⁷ a DFT program package with plane wave as basis set. The interactions between ions and electrons was described using the projector augmented wave method.⁸⁷ The nonlocal exchange-correlation energy was evaluated by the PBE functional. For systems involving Ce atoms, the DFT+U method^{130,169-172} (U = 5 used in this work) was used to treat the highly correlated *f*-electrons of Ce atoms. The plane wave basis set with a cutoff energy of 400 eV was used to expand the wave function of valence electrons. Spin-polarization was included in all calculations. The atomic structures were relaxed until the forces on the unconstrained atoms were less than 0.05 eV/Å.

The ZrO₂ substrate was taken from the monoclinic ZrO₂ bulk structure optimized with the same set of parameters. The zirconium atoms in the bulk structure are all hepta-coordinated whereas the oxygen atoms are either tri- or tetra- coordinated. The optimized lattice parameters *a*, *b*, *c* and γ of ZrO₂ bulk are 5.160, 5.236, 5.319 Å and 99.64°, in good agreement with the experimental values of 5.151, 5.212, 5.317 Å and 99.23°.¹⁷³ Since the (111) orientation of ZrO₂ is the most stable surface, the ZrO₂(111) surface was

chosen as the supporting ZrO_2 substrate. The model $\text{ZrO}_2(111)$ slab consists of three O-Zr-O tri-layers. As shown in Figure 5.1a, within the surface tri-layer, the topmost layer consists of four bi-coordinated oxygen and four tri-coordinated oxygen sites (labeled as O_{2c} and O_{3c}). The middle layer of the top tri-layer consists of four hexa-coordinated and four hepta-coordinated Zr atoms (labeled as Zr_{6c} and Zr_{7c}).

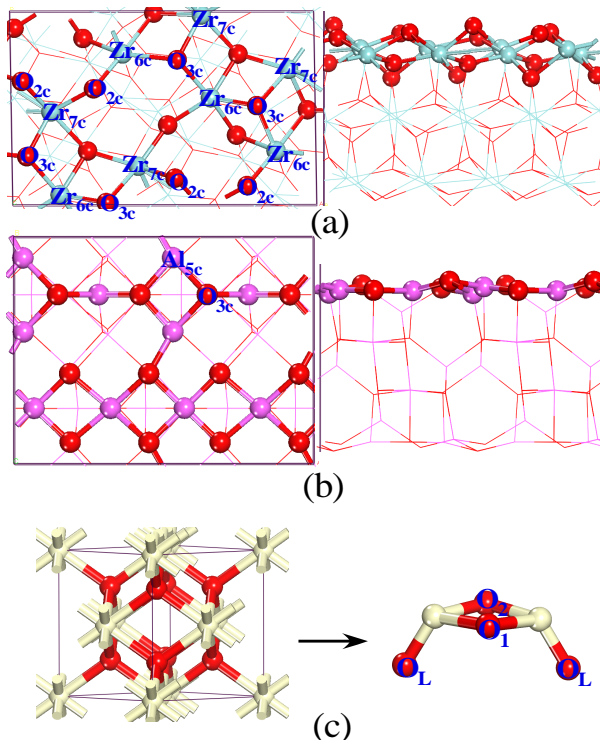


Figure 5.1. Top and side views of $\text{ZrO}_2(111)$ and $\gamma\text{-Al}_2\text{O}_3(100)$ surface slabs. (a) $\text{ZrO}_2(111)$; (b) $\gamma\text{-Al}_2\text{O}_3(100)$. The atoms in the top surface layer are shown in ball and stick; the other atoms in the systems are shown in line format. Zr_{6c} and Zr_{7c} (in light blue) are the hexa- and hepta-coordinated Zr atoms; O_{2c} and O_{3c} (in red) are di- and tri-coordinated O atoms; Al_{5c} (in magenta) is the penta-coordinated Al atom. Reproduced with permission from J. Phys. Chem. C, 2009, 113, 18296. Copyright 2009 American Chemical Society.

The $\gamma\text{-Al}_2\text{O}_3$ substrate was taken from the non-spinel $\gamma\text{-Al}_2\text{O}_3$ bulk structure. Previous experiments suggested that the penta-coordinated Al sites are available only on the (100) surface of the $\gamma\text{-Al}_2\text{O}_3$ and are the most likely nucleation sites for metal and metal oxide clusters.^{129,174} As a result, the $\gamma\text{-Al}_2\text{O}_3(100)$ surface was chosen as the $\gamma\text{-Al}_2\text{O}_3$ support in this work. As shown in Figure 5.1b, the $\gamma\text{-Al}_2\text{O}_3(100)$ surface is terminated with twelve

tri-coordinated oxygen and eight penta-coordinated Al^{3+} atoms. We note that both cations and anions are exposed in the topmost layer on the $\gamma\text{-Al}_2\text{O}_3(100)$ surface. This is different from the $\text{ZrO}_2(111)$ surface where the anion layer is distinctively higher than the cation layer. Both the $\text{ZrO}_2(111)$ and $\gamma\text{-Al}_2\text{O}_3(100)$ surface slabs are stoichiometric, non-polar and oxygen-terminated. The dimensions of the two surface unit cells were chosen to allow a nearly same coverage of the binding Ce_2O_4 cluster.

In all surface calculations, a vacuum space of at least 12 \AA was inserted in the direction perpendicular to the surface between images of the slab. The initial structure of the Ce_2O_4 cluster was constructed on the basis of the CeO_2 bulk structure and was optimized in a box with a vacuum space of at least 12 \AA in each direction. For the supported Ce_2O_4 cluster on both surfaces, the cluster together with the top two tri-layers of $\text{ZrO}_2(111)$ surface and the top two layers of $\gamma\text{-Al}_2\text{O}_3$ surface were allowed to relax during the geometry optimization. K-point meshes of $2 \times 3 \times 1$ and $2 \times 2 \times 1$ for $\text{ZrO}_2(111)$ and $\gamma\text{-Al}_2\text{O}_3(100)$, respectively, were used to generate the K-points according to the Monkhorst-Pack scheme. Convergence tests with regard to cutoff energy and K-points sample have been performed to ensure the accuracy of the calculations.

5.3 Results and Discussion

5.3.1. Adsorption of CO and CO_2 on the $\text{ZrO}_2(111)$ and $\gamma\text{-Al}_2\text{O}_3(100)$ Surfaces. *a. CO Adsorption.* On $\text{ZrO}_2(111)$, our optimization resulted in a CO molecule lying 2.56 \AA above a hexa-coordinated Zr site. Our calculated adsorption energy of CO in this structure is -0.43 eV , close to the measured heat of adsorption for CO ($0.46 \sim 0.52 \text{ eV}$) from microcalorimetry.¹⁷⁵ The C–O stretching frequency is calculated to be 2172 cm^{-1} which is blue shifted by 43 cm^{-1} with respect to the calculated C–O stretching frequency

of 2129 cm^{-1} in the gas phase. In the previous experimental studies, two different CO adsorption modes were reported on the monoclinic zirconia.^{175,176} The high C–O frequency that ranges from 2192 to 2195 cm^{-1} was assigned to CO adsorbed at the defective sites. The low C–O frequency in the range of $2184\sim 2187\text{ cm}^{-1}$, which is blue shifted by $41 \sim 44\text{ cm}^{-1}$ with respect to the experimental C–O stretching frequency of 2143 cm^{-1} in the gas phase,¹⁷⁷ was assigned to the adsorbed CO at the surface Zr cations. With respect to the calculated C–O stretching frequency in gas phase, our calculated C–O frequency for adsorbed CO is in good agreement with the experimental measurements. Since the (111) surface is the most stable surface and is expected to dominate the surface of a ZrO_2 particle,¹⁷⁸ the low C–O frequency mode in those experimental spectra should correspond to the adsorbed CO at the cationic Zr site of the $\text{ZrO}_2(111)$ surface.

On the $\gamma\text{-Al}_2\text{O}_3(100)$ surface, CO was found to adsorb at the penta-coordinated surface Al site with a O–Al distance of 2.33 \AA . The adsorption energy of CO on the $\gamma\text{-Al}_2\text{O}_3(100)$ surface is -0.15 eV . The calculated C–O stretching frequency is blue shifted by 16 cm^{-1} with respect to the gas phase value. Although there is no direct comparison with the experimentally observed IR spectra, our results are in general consistent with the previous theoretical calculations.^{96,179} In the early computational work of Zecchina et al, the band with a blue shift of 22 cm^{-1} was assigned to CO adsorption at the penta-coordinated Al^{3+} sites with an adsorption energy of -0.21 eV .¹⁷⁹ Digne et al⁹⁶ also reported a blue shift of $10\sim 16\text{ cm}^{-1}$ for CO adsorption on the penta-coordinated Al sites with the same $\gamma\text{-Al}_2\text{O}_3(100)$ surface model used in this work. The adsorption energy of CO were in a range of $-0.41 \sim -0.21\text{ eV}$, slightly larger than our value.

The vibrational properties of CO adsorbed on oxides have been used to elucidate the nature of the cationic sites.¹⁷⁹ On a non transition metal oxide surface, the interaction between CO and cation site is predominantly electrostatic. The blue shift of CO stretching frequency is a result of the polarized field of the cation, and the magnitude of the shift is proportional to the strength of the field.¹⁷⁹ We note, however, that Zr is a 4d transition metal element and the contribution of d orbitals often reduces the electrostatic effect. The fact that CO adsorbed on the ZrO₂(111) surface has a larger blue shift in C–O stretching frequency and a larger adsorption energy than CO adsorbed on γ -Al₂O₃(100) indicates that the local field induced by Zr⁴⁺ on the ZrO₂(111) surface is stronger than that by the Al³⁺ sites on γ -Al₂O₃(100). Consequently, the Zr⁴⁺ site on the ZrO₂(111) surface is expected to be more acidic than the Al³⁺ sites on γ -Al₂O₃(100).

b. CO₂ Adsorption. The acidic CO₂ molecule generally adsorbs on the basic sites of oxide surface.¹⁸⁰ Different strengths of surface basicity are expected to result in different adsorption configurations.^{83,181,182} Typically, CO₂ binds at a strong basic oxygen site in a monodentate configuration via a C–O_{surf} bond, whereas at the weak basic sites, it binds in bidentate or bridged configurations via both C–O_{surf} and O–M_{surf} bonds. On the ZrO₂(111) surface, we found that CO₂ adsorbs in a bidentate configuration, forming a carbonate like species. The C–O bond lengths of the carbonate species are 1.21, 1.28 and 1.51 Å, respectively. The adsorption energy was calculated to be +0.05 eV, indicating that the adsorption is slightly endothermic. However, our vibrational frequency analysis of the adsorption structure shows that the resulting carbonate is at a true minimum since no imaginary frequency was found. The frequencies corresponding to the symmetric and asymmetric stretching are 1850 and 1187 cm⁻¹, respectively. These values are close to

those of bridged carbonate species.¹⁸³ The adsorption of CO₂ on γ -Al₂O₃(100) has been studied previously.¹⁸¹ The adsorbed CO₂ binds a surface O–Al bridge site and forms a bidentate carbonate species. The calculated adsorption energy of CO₂ on the γ -Al₂O₃(100) surface is –0.80 eV.

5.3.2. Ce₂O₄ Cluster on the ZrO₂(111) and γ -Al₂O₃(100) Supports. The optimized structure of the unsupported Ce₂O₄ cluster consists of a planar ring and two out-of-plane oxygen “legs” (O_L), as shown in Figure 5.1c. Based on the chemical intuition that aligns the cluster cations with the surface anions and the cluster anions with surface cationic sites, multiple binding configurations of the Ce₂O₄ cluster over on ZrO₂(111) and γ -Al₂O₃(100) have been examined. The stability of the supported Ce₂O₄ cluster was evaluated by calculating its binding energy,

$$E_{bind} = E_{ce2o4}^S - (E_{ce2o4} + E_{supp}), \quad (5.1)$$

where E_{ce2o4}^S is the total energy of the Ce₂O₄ cluster interacting with the supporting substrate; E_{ce2o4} and E_{supp} are the total energies of the unsupported Ce₂O₄ cluster and the substrate, respectively. According to this definition, a more negative binding energy corresponds to a stronger interaction between the cluster and the supporting surface.

The most stable structure of the Ce₂O₄ cluster on the ZrO₂(111) surface has a binding energy of –5.32 eV. The top and side views of this structure are shown in Figure 5.2a. Two O_L atoms of the Ce₂O₄ cluster bind with the surface Zr_{6c} and Zr_{7c} sites in a bridging configuration. The bond lengths of the O_L–Zr_{6c} and O_L–Zr_{7c} are 2.15 and 2.09 Å, respectively. The planar structure of Ce–O₁–Ce–O₂ is tilted with respect to the ZrO₂(111) surface plane so that the O₁ atom points to the substrate surface with a O₁–Zr_{7c} bond of 2.11 Å. In addition, each Ce atom interacts with an O_{2c} site at a Ce–O_{2c} distance of ~

2.20 Å, further enhancing the interaction between the cluster and the support. Bader charge analysis⁹⁰ indicates that the ZrO₂ surface slab is slightly reduced with a total charge of -0.20 |e|. This charge was transferred from the supported Ce₂O₄ cluster.

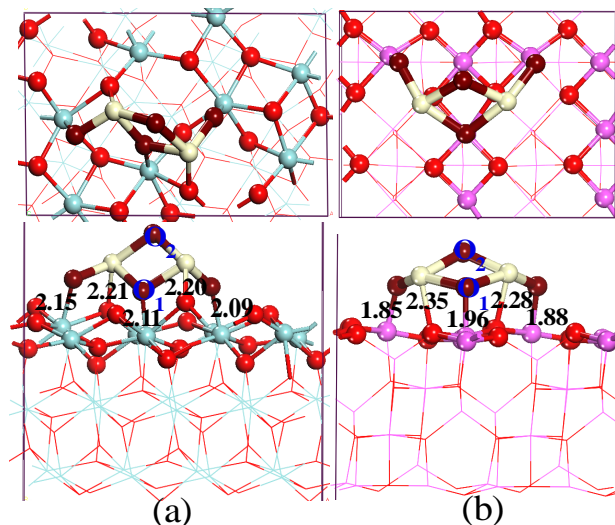


Figure 5.2. Optimized structures of Ce₂O₄ cluster supported on the (a) ZrO₂(111) and (b) γ-Al₂O₃(100) surfaces. (c) Optimized structure of the unsupported Ce₂O₄ cluster. The color scheme is the same as that of Figure 1. Oxygen atoms of Ce₂O₄ cluster are shown in dark red; Ce atoms are shown in yellow. Reproduced with permission from J. Phys. Chem. C, 2009, 113, 18296. Copyright 2009 American Chemical Society.

On the γ-Al₂O₃(100) surface, all the oxygen atoms are tri-coordinated. The strength of the interaction between a cluster Ce ion and the surface oxygen site is expected to depend on their distance. In the most stable structure of the Ce₂O₄ cluster supported on the γ-Al₂O₃(100) surface, shown in Figure 5.2b, the distances between the oxygen atoms of the cluster and the bonded Al_{5c} sites are 1.85, 1.88, and 1.96 Å, respectively. The two Ce–O_{3c} bond lengths are 2.35 and 2.28 Å. The calculated binding energy of Ce₂O₄ on the γ-Al₂O₃(100) surface is -4.21 eV. Bader charge analysis indicates that no net charge transfer is found between the supported Ce₂O₄ cluster and the γ-Al₂O₃(100) slab. This can be attributed to the irreducible nature of the γ-Al₂O₃ surface.

The interaction between the Ce_2O_4 cluster and the $\gamma\text{-Al}_2\text{O}_3(100)$ substrate is weaker than that between Ce_2O_4 and $\text{ZrO}_2(111)$. The binding of the Ce_2O_4 cluster on the $\text{ZrO}_2(111)$ and $\gamma\text{-Al}_2\text{O}_3(100)$ surfaces arises from the cation and anion pairs between the cluster and surface sites. The relative stabilities of the Ce_2O_4 cluster on the supports can be affected by many factors, including the charge and coordination unsaturation of surface cationic sites as well as the geometric mismatch between the cluster and the substrate. First, the formal charges of the cationic sites on $\text{ZrO}_2(111)$ and $\gamma\text{-Al}_2\text{O}_3(100)$ are +4 and +3, respectively. Second, the $\text{ZrO}_2(111)$ surface exposes both the bi-coordinated and the tri-coordinated oxygen sites while the $\gamma\text{-Al}_2\text{O}_3(100)$ surface exposes only the tri-coordinated oxygen sites. The stronger binding of Ce_2O_4 on $\text{ZrO}_2(111)$ than on $\gamma\text{-Al}_2\text{O}_3(100)$ can be attributed to an overall effect of both factors.

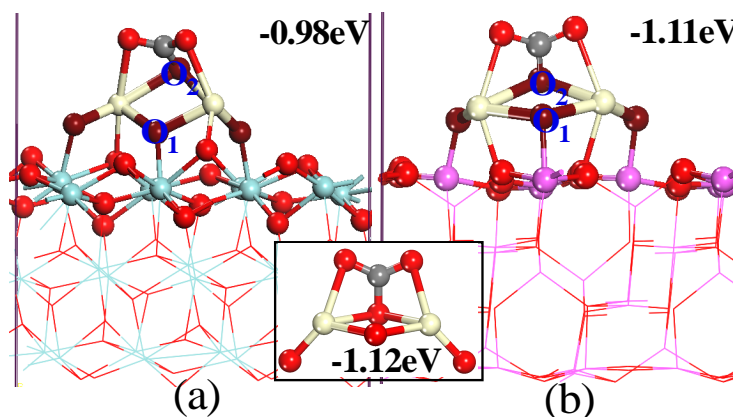


Figure 5.3. CO_2 adsorption on (a) $\text{ZrO}_2(111)$ supported and (b) $\gamma\text{-Al}_2\text{O}_3(100)$ supported Ce_2O_4 cluster. CO_2 adsorption on the unsupported Ce_2O_4 cluster is shown in the inset. The C atom is in gray. Reproduced with permission from J. Phys. Chem. C, 2009, 113, 18296. Copyright 2009 American Chemical Society.

5.3.3. CO_2 Adsorption on the Supported Ce_2O_4 Cluster. CO_2 also adsorbs on the basic oxygen sites of the supported Ce_2O_4 clusters. Figure 5.3 shows the relaxed structures for

CO₂ adsorption on both ZrO₂(111) and γ -Al₂O₃(100) supported Ce₂O₄ clusters. In both adsorption structures, the carbon atom binds an oxygen atom of the Ce₂O₄ cluster, forming a surface carbonate CO₃²⁻ species. CO₂ adsorption on the supported Ce₂O₄ cluster is typically attributed to an acid-base interaction due to the strong basicity of the oxygen atoms in the Ce₂O₄ cluster.^{184,185} The adsorption energies of CO₂ on the ZrO₂(111) and the γ -Al₂O₃(100) supported Ce₂O₄ cluster are -0.98 and -1.11 eV, which are close to the adsorption energy of -1.12 eV of CO₂ on the unsupported Ce₂O₄ cluster in a similar configuration. Bader charge analysis showed that the CO₂ adsorption did not cause charge transfer between support and Ce₂O₄: the ZrO₂(111) slab remains reduced by $\sim -0.2 |e|$ whereas there is no net charge in the γ -Al₂O₃(100) slab. Charge redistributions did occur between the adsorbed CO₂ molecule and the Ce₂O₄ clusters. Since there is no charge transfer between the Ce₂O₄ clusters and the two substrates, it is expected that the ZrO₂(111) and γ -Al₂O₃(100) supports have very minor effects on the acid-base interaction between CO₂ and the Ce₂O₄ clusters.

Unlike the typical adsorption configuration of CO₂ on single crystal metal oxide surfaces in which at least one of the oxygen atoms of the resulting carbonate species does not interact directly with the cationic sites of the surface,⁵⁶ all three oxygen atoms of the carbonate species shown in Figure 5.3 are in the range of forming bonds with the Ce atoms of the cluster. The calculated asymmetric and symmetric stretching frequencies for the carbonate species formed on ZrO₂(111) supported Ce₂O₄ cluster are 1529 and 1262 cm⁻¹, respectively. The corresponding frequencies on the γ -Al₂O₃(100) supported Ce₂O₄ cluster are 1517 and 1278 cm⁻¹, respectively. On the unsupported Ce₂O₄ cluster, the carbonate species has the frequencies of 1514 and 1266 cm⁻¹. Clearly, these frequencies

of the carbonates, both on the supported clusters and unsupported cluster, are in the range of but different from the reported assignments of the monodentate, bidentate and bridged configurations of adsorbed CO₂ on metal oxide surfaces,¹⁸⁴ suggesting the uniqueness of CO₂ adsorption configuration on the Ce₂O₄ clusters.

5.3.4. CO Adsorption on Ce Sites of the Supported Ce₂O₄ Cluster. CO molecule can adsorb through its carbon atom onto the acidic Ce site of the supported Ce₂O₄ cluster in an upright configuration. The optimized structures of CO adsorption on the Ce site of the ZrO₂(111) supported Ce₂O₄ (Figure 5.4a) and γ -Al₂O₃(100) supported Ce₂O₄ the (Figure 5.4b) are very similar. The calculated CO adsorption energies are -0.25 and -0.28 eV respectively. Compared to the CO adsorbed on the unsupported Ce₂O₄ cluster (-0.24 eV), the weak interaction between CO molecule and the supported Ce₂O₄ cluster via the C–Ce bonding indicates both supports have little effects on “physical” adsorption of CO on the Ce₂O₄ cluster.

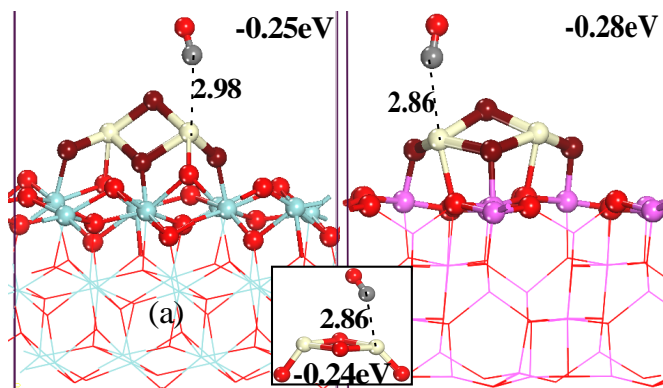


Figure 5.4. CO adsorption on Ce atom of (a) ZrO₂(111) supported and (b) γ -Al₂O₃(100) supported Ce₂O₄ cluster. CO adsorption on the Ce atom of the unsupported Ce₂O₄ cluster is shown in the inset. Reproduced with permission from J. Phys. Chem. C, 2009, 113, 18296. Copyright 2009 American Chemical Society.

5.3.5. The Reactivity of the $\text{ZrO}_2(111)$ and the $\gamma\text{-Al}_2\text{O}_3(100)$ Supported Ce_2O_4

Clusters. The reactivity of the $\text{ZrO}_2(111)$ and the $\gamma\text{-Al}_2\text{O}_3(100)$ supported Ce_2O_4 clusters are investigated by “reactive” adsorption of CO. In addition to the physisorbed CO on the supported and the unsupported Ce_2O_4 clusters discussed in section 5.3.4, a CO molecule can also be adsorbed through its carbon atom, bridging the two oxygen atoms of the supported Ce_2O_4 cluster. After adsorption, the CO molecule, in combination with the two oxygen atoms of the cluster, forms a carbonate like (CO_3^{2-}) species. We therefore refer to this CO adsorption mode as CO *reactive* adsorption. The optimized structures of CO reactive adsorption on the $\text{ZrO}_2(111)$ and $\gamma\text{-Al}_2\text{O}_3(100)$ supported Ce_2O_4 clusters are shown in Figure 5.5a and 5.5b. After CO reactive adsorption, the O_1 and O_2 atoms of the supported Ce_2O_4 cluster were pulled out of their original positions to form the CO_3^{2-} species. Meanwhile, the other atoms of the Ce_2O_4 clusters underwent pronounced relaxations. As shown in Figure 5.5a, the two Ce atoms were pushed apart from each other with respect to their original positions in the adsorbed cluster structure before CO adsorption. Nevertheless, both O_L atoms and both Ce atoms as well as the O_1 atom remain bonded with the support. The lengths of the three C–O bond in the CO_3^{2-} species formed on the $\text{ZrO}_2(111)$ supported Ce_2O_4 cluster are 1.28, 1.29, and 1.34 Å, respectively. These C–O bond distances are very close to the C–O distance of 1.28 Å in CaCO_3 ,¹⁸⁶ confirming the formation of a CO_3^{2-} species after CO reactive adsorption. Moreover, the vibrational frequencies calculated for the adsorption structure are 1510 and 1299 cm^{-1} , consistent with the experimental values on the CeO_2 surface, although the comparable values were assigned to an inorganic carboxylate.¹⁸⁴ On the $\gamma\text{-Al}_2\text{O}_3(100)$ supported Ce_2O_4 cluster, the optimized structure is more symmetric after CO reactive

adsorption, as shown in Figure 5.5b. Although the original structure of the Ce_2O_4 cluster is also deformed after CO adsorption, the atoms of Ce_2O_4 remain bonded with the γ - $\text{Al}_2\text{O}_3(100)$ substrate. The calculated C–O distances of the CO_3^{2-} species formed on the γ - $\text{Al}_2\text{O}_3(100)$ supported Ce_2O_4 cluster are 1.27, 1.28 and 1.37 Å, respectively, and again, are very similar to the CO_3^{2-} in bulk CaCO_3 . The frequencies calculated for the CO_3^{2-} species are 1562 and 1255 cm^{-1} , which are also in agreement with the experimental values.¹⁸⁴

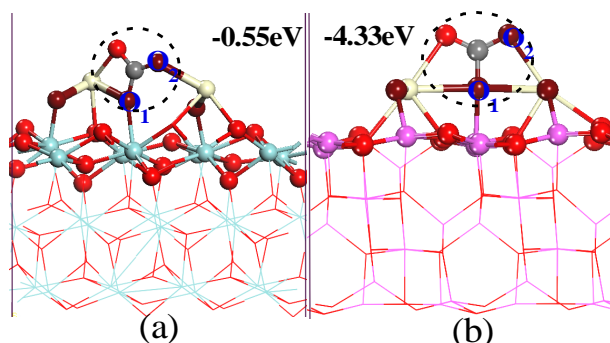


Figure 5.5. Carbonate-like structure formed on (a) $\text{ZrO}_2(111)$ supported and (b) γ - $\text{Al}_2\text{O}_3(100)$ supported Ce_2O_4 cluster upon reactive adsorption of CO. Reproduced with permission from J. Phys. Chem. C, 2009, 113, 18296. Copyright 2009 American Chemical Society.

Furthermore, we examined the energetics for reactive adsorption of CO. The adsorption energies are calculated as,

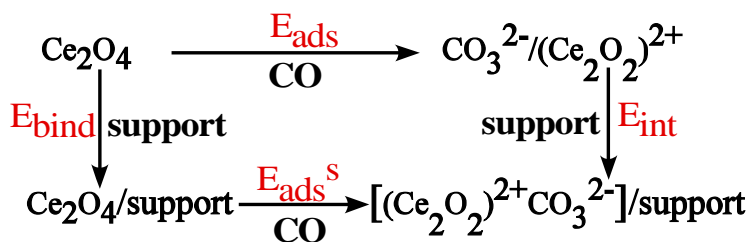
$$E_{ads}^S = E_{(\text{Ce}_2\text{O}_2)(\text{CO}_3)}^S - (E_{\text{Ce}_2\text{O}_4}^S + E_{\text{CO}}) \quad (5.2)$$

where $E_{(\text{Ce}_2\text{O}_2)(\text{CO}_3)}^S$ is the total energy of system in which CO is reactively adsorbed on the supported Ce_2O_4 cluster. The calculated CO adsorption energies for the $\text{ZrO}_2(111)$ and γ - $\text{Al}_2\text{O}_3(100)$ supported Ce_2O_4 clusters are -0.55 and -4.33 eV, respectively. Bader charge analysis showed that in addition to the charge redistribution associated with the formation of the CO_3^- species, the $\text{ZrO}_2(111)$ and γ - $\text{Al}_2\text{O}_3(100)$ supports gained electron charges of 0.37 and 0.28 |e|, respectively, indicating both substrates were reduced upon

CO adsorption. In the case of ZrO₂(111), CO adsorption makes the substrate further reduced with respect to the substrate only supporting the Ce₂O₄ cluster. We expected the contributions from the CO–Ce₂O₄ interaction to CO adsorption energies to be similar since CO only interacts directly with the Ce₂O₄ clusters in both systems. Such a significant difference in CO adsorption energies was, therefore, not anticipated. The obvious difference between the two systems is the substrate: zirconia is reducible whereas alumina is not. As a reference, we calculated the reactive adsorption of CO on the unsupported Ce₂O₄ cluster. The optimized adsorption structure is similar to those of the Ce₂O₄-CO fragments in Figure 5.5a and b. The adsorption energy is –2.60 eV according to

$$E_{ads} = E_{(Ce_2O_2)(CO_3)} - (E_{Ce_2O_4} + E_{CO}) \quad (5.3)$$

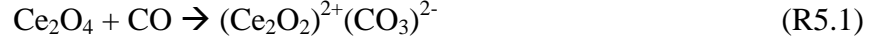
where $E_{(Ce_2O_2)(CO_3)}$ is the total energy of reactively adsorbed CO on the unsupported Ce₂O₄ cluster. If we use the adsorption energy on the unsupported Ce₂O₄ as a reference, the two supports will have an opposite effect on the CO reactive adsorption: the adsorption energy is decreased with ZrO₂(111) being the support but increased with γ -Al₂O₃(100) as the support.



Scheme 5.1. Thermodynamic cycle of CO reactive adsorption on the supported Ce₂O₄ cluster. Reproduced with permission from J. Phys. Chem. C, 2009, 113, 18296. Copyright 2009 American Chemical Society.

To understand the origin of the dramatic difference between the ZrO₂(111) and γ -Al₂O₃(100) supported Ce₂O₄ cluster towards CO reactive adsorption, we constructed a

thermodynamic cycle of converting Ce_2O_4 to $(\text{Ce}_2\text{O}_2)^{2+}(\text{CO}_3)^{2-}$ through CO reactive adsorption on the two supports. As shown in Scheme 5.1, the formation of CO_3^{2-} causes CO to lose two electrons to the adjacent two Ce^{4+} ions. The step on the unsupported and both supported Ce_2O_4 clusters can be described as:



Thus the adsorption structures shown in Figure 5.5 can be divided into two parts: the support and the $(\text{Ce}_2\text{O}_2)^{2+}(\text{CO}_3)^{2-}$ complex. The interaction energy (E_{int}) between the support and the $(\text{Ce}_2\text{O}_2)^{2+}(\text{CO}_3)^{2-}$ complex can be calculated as:

$$E_{int} = E_{(\text{Ce}_2\text{O}_2)(\text{CO}_3)}^S - (E_{(\text{Ce}_2\text{O}_2)(\text{CO}_3)} + E_{supp}) \quad (\text{5.4})$$

The calculated E_{int} are -3.27 eV for $\text{ZrO}_2(111)$ and -5.94 eV for $\gamma\text{-Al}_2\text{O}_3(100)$. Based on thermodynamic cycle illustrated in Scheme 5.1, we have

$$E_{ads}^S = E_{ads} + E_{int} - E_{bind} \quad (\text{5.5})$$

With E_{ads} known from Eq.(5.3), E_{ads}^S will only depend on the value of $(E_{int} - E_{bind})$.

E_{int} (or E_{bind}) measures the strength of the interaction between $(\text{Ce}_2\text{O}_2)^{2+}(\text{CO}_3)^{2-}$ (or Ce_2O_4) and the support. The calculated E_{int} and E_{bind} for both supports are provided in Table 5.1. On the $\text{ZrO}_2(111)$ support, the interaction between $(\text{Ce}_2\text{O}_2)^{2+}(\text{CO}_3)^{2-}$ and $\text{ZrO}_2(111)$ ($E_{int} = -3.27$ eV) is weaker than that between Ce_2O_4 and $\text{ZrO}_2(111)$ ($E_{bind} = -5.32$ eV). Consequently, $E_{int} - E_{bind}$ is positive (2.05 eV). This makes the CO reactive adsorption much weaker on the $\text{ZrO}_2(111)$ supported Ce_2O_4 than that on the unsupported Ce_2O_4 . On the other hand, the binding of $(\text{Ce}_2\text{O}_2)^{2+}(\text{CO}_3)^{2-}$ ($E_{int} = -5.94$ eV) is significantly stronger than that of Ce_2O_4 ($E_{bind} = -4.21$ eV) on the $\gamma\text{-Al}_2\text{O}_3(100)$ substrate, yielding a negative value of $(E_{int} - E_{bind})$ (-1.73 eV). This results in an increased CO reactive adsorption energy on the $\gamma\text{-Al}_2\text{O}_3(100)$ support Ce_2O_4 cluster by

1.73 eV stronger with respect to the unsupported Ce₂O₄ cluster. Overall, difference of the CO reactive adsorption energy on the two supports is 3.78 eV. Clearly, the ZrO₂(111) and γ -Al₂O₃(100) substrates induced completely opposite effects for the Ce₂O₄ cluster toward reactive adsorption of CO.

Table 5.1. Calculated reactive adsorption energies (eV) of CO on the unsupported Ce₂O₄ cluster (E_{ads}), an on the ZrO₂(111) and γ -Al₂O₃(100) supported Ce₂O₄ cluster ($E_{\text{ads}}^{\text{s}}$); the binding energies of Ce₂O₄ cluster (E_{bind}) and (Ce₂O₂)²⁺CO₃²⁻ (E_{int}) on the ZrO₂(111) and the γ -Al₂O₃(100) substrates. Reproduced with permission from J. Phys. Chem. C, 2009, 113, 18296. Copyright 2009 American Chemical Society.

System	E_{ads}	$E_{\text{ads}}^{\text{s}}$	E_{bind}	E_{int}
Ce ₂ O ₄	-2.60	-	-	-
Ce ₂ O ₄ /ZrO ₂ (111)	-	-0.55	-5.32	-3.27
Ce ₂ O ₄ / γ -Al ₂ O ₃ (100)	-	-4.33	-4.21	-5.94

To further elucidate the effect of different supports on the CO reactive adsorption on Ce₂O₄, we performed a local density of state analysis for the Ce atoms in the Ce₂O₄ cluster supported on the ZrO₂(111) and γ -Al₂O₃(100) substrates, as well as the unsupported Ce₂O₄ cluster. The projected density of states (PDOSs) of the Ce atoms was plotted in Figure 5.6. Before CO adsorption, the PDOSs of the two Ce atoms in the Ce₂O₄ cluster on both substrates are very similar, as shown in Figure 5.6a and d. Upon CO adsorption, the *f*-associated peaks of the Ce atoms were shifted downward on both ZrO₂(111) (Figure 5.6b, c) and γ -Al₂O₃(100) (Figure 5.6e,f) supports. On the ZrO₂(111) supported Ce₂O₄ cluster shown in Figure 5.2a, the main *f*-states are located at 1 ~ 2 eV above the Fermi level, as shown in Figure 5.6a. This indicates that the *f*-states of the Ce atoms are unoccupied and the Ce atoms are fully oxidized. After reactive adsorption of CO, these *f*-states are split into two parts: one is located at the Fermi level while the other lies at a relatively higher energy of ~ 3 eV above the Fermi level, as shown in Figure 5.6b

and c. Moreover, the states located at $-5 \sim -1$ eV with equally dominant d and f features before CO adsorption have been shifted downward to $-6 \sim -2$ eV and lost some intensity after CO adsorption. Although the two Ce atoms in Figure 5.5a appear not to be structurally symmetric, the PDOSs of these two Ce atoms shown in Figure 5.6b and c are very similar. Therefore, both Ce atoms were reduced through partial occupation of their $4f$ states upon CO reactive adsorption. On the γ - $\text{Al}_2\text{O}_3(100)$ supported Ce_2O_4 cluster, the initially unoccupied f states of the Ce atoms are located at $0.5 \sim 1.5$ eV above the Fermi level (Figure 5.5d). After CO reactive adsorption, these f states are shifted to ~ -1 eV below the Fermi level and become occupied (Figure 5.6e and f), again indicating the Ce atoms were reduced.

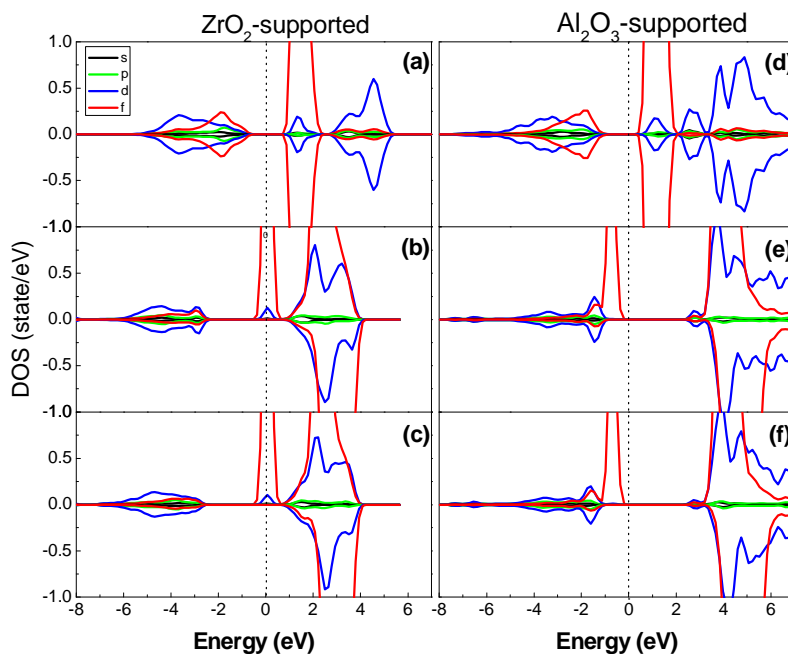
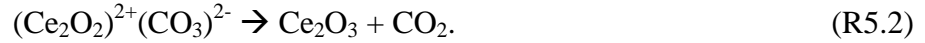


Figure 5.6. PDOS of the Ce atoms in the $\text{ZrO}_2(111)$ -supported Ce_2O_4 before (a) and after (b,c) CO reactive adsorption and PDOS of the Ce atoms in the $\text{Al}_2\text{O}_3(100)$ -supported Ce_2O_4 before (d) and after (e,f) CO reactive adsorption. Reproduced with permission from J. Phys. Chem. C, 2009, 113, 18296. Copyright 2009 American Chemical Society.

Figure 5.6 also shows the differences between the splits of states on the two supports. On $\text{ZrO}_2(111)$, the occupied $4f$ states are located at the Fermi level and close to the bottom of the conduction band. In contrast, these occupied states on $\gamma\text{-Al}_2\text{O}_3(100)$ are located at the top of the occupied valence band and well-below the Fermi level. The different characteristics of Ce $4f$ states on the two supporting oxides are likely results of the different properties of the two oxides. The reducible $\text{ZrO}_2(111)$ destabilizes the occupied Ce $4f$ states after reduction, and thereby, the $(\text{Ce}_2\text{O}_2)^{2+}(\text{CO}_3)^{2-}$ intermediate, and promotes the turnover of CO to CO_2 . On the other hand, the irreducible $\gamma\text{-Al}_2\text{O}_3(100)$ stabilizes the occupied Ce $4f$ states, and consequently, the $(\text{Ce}_2\text{O}_2)^{2+}(\text{CO}_3)^{2-}$ intermediate. The high stability of the intermediate formed on $\gamma\text{-Al}_2\text{O}_3(100)$ makes the reaction stagnate at the intermediate states and slows down the overall reaction.

The oxidation of CO has been frequently used as a probe reaction to investigate the reactivity of ceria-based catalysts.^{153,156,157,165,187,188} It is believed that the lattice oxygen acts as oxidant and the reaction occurs via the Mars-van Krevelen mechanism.^{149,150} Aneggi et al demonstrated that the reaction is surface structure sensitive.¹⁸⁹ The carbonate-like species have been proposed as likely intermediates during CO oxidation over the ceria-based catalysts.¹⁸⁹ In the following discussion, we demonstrate the support effects on the reactivity of the Ce_2O_4 cluster for CO oxidation based on the formation of the $(\text{Ce}_2\text{O}_2)^{2+}(\text{CO}_3)^{2-}$ intermediate by analyzing the complete cycle on the $\text{ZrO}_2(111)$ and $\gamma\text{-Al}_2\text{O}_3(100)$ supported, as well as the unsupported Ce_2O_4 clusters. The oxidation of CO in these systems can be schematically decomposed into three steps, as shown in Figure 5.7a. In the first step, CO molecule adsorbs on the Ce_2O_4 cluster forming the carbonate-like complex species. The first step is exothermic on Ce_2O_4 supported on both $\text{ZrO}_2(111)$

and $\gamma\text{-Al}_2\text{O}_3(100)$ and the reaction energies are -0.55 and -4.33 eV. The second step is to desorb CO_2 and form an oxygen-deficient Ce_2O_3 cluster supported on the substrates by decomposing the carbonate-like $(\text{Ce}_2\text{O}_2)^{2+}(\text{CO}_3)^{2-}$ species via the following reaction:



The calculated reaction energies for (R5.2) are -0.50 and $+1.71$ eV for the $\text{ZrO}_2(111)$ and $\gamma\text{-Al}_2\text{O}_3(100)$ supported clusters, respectively. We note that after CO_2 desorption the resulted Ce_2O_3 clusters on both supports kept the skeletal structures of the original supported Ce_2O_4 clusters. To complete the catalytic cycle, the Ce_2O_3 cluster has to be re-oxidized to regenerate Ce_2O_4 ,



The reaction energies of the oxidation step (R5.3) are calculated to be -2.21 and -0.63 eV for the $\text{ZrO}_2(111)$ supported and the $\gamma\text{-Al}_2\text{O}_3(100)$ supported clusters, respectively. Figure 5.7b summarizes the energetics in the potential energy profiles for the reaction on the $\text{ZrO}_2(111)$ and $\gamma\text{-Al}_2\text{O}_3(100)$ supported Ce_2O_4 clusters. Figure 5.7 also includes the energetics of the corresponding reaction steps on the unsupported Ce_2O_4 cluster. The reaction energies of three steps (R5.1~R5.3) on the $\text{CeO}_2(100)$ surface were reported by Nolan et al.¹⁷¹ using DFT+U (U = 5) method. The local structure of the (100) surface where CO reactive adsorption occurs is very similar to that of the unsupported Ce_2O_4 cluster in this work. The adsorption energy of CO on the $\text{CeO}_2(100)$ surface with the similar adsorption structure is -3.21 eV. (We note that the adsorption energy of CO on $\text{CeO}_2(110)$ depends on the U values in DFT+U calculation, as demonstrated by Huang and Fabris.¹⁷²) The reaction energy for CO oxidation on the $\text{CeO}_2(100)$ surfaces is -0.88 eV.¹⁷¹ We re-analyzed their results based on the reaction cycle in Figure 5.7a and

obtained the CO₂ desorption energies of +2.33 eV on the CeO₂(100) surface shown in Figure 5.7b.

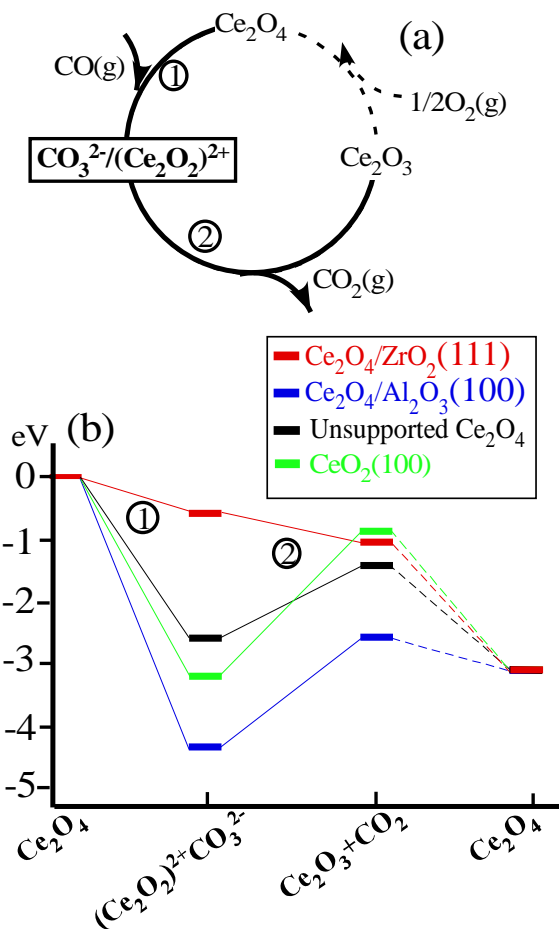


Figure 5.7. Potential energy profiles of CO oxidation on unsupported (black), ZrO₂(111) (red) and γ -Al₂O₃(100) (blue) supported Ce₂O₄ cluster, and CeO₂(100) (green) surface. Reproduced with permission from J. Phys. Chem. C, 2009, 113, 18296. Copyright 2009 American Chemical Society.

As shown in Figure 5.7b, the ZrO₂(111) and γ -Al₂O₃(100) substrates have dramatically different effects on the CO oxidation reaction over the supported Ce₂O₄ clusters. The formation of the intermediate (Ce₂O₂)²⁺(CO₃)²⁻ (R5.1) and the re-oxidation step (R5.3) are exothermic on both supports. However, CO₂ desorption (R5.2) is exothermic on the ZrO₂(111) supported Ce₂O₄ cluster but endothermic on the γ -

$\text{Al}_2\text{O}_3(100)$ supported Ce_2O_4 cluster. Although the reactive adsorption of CO is energetically favorable over the $\gamma\text{-Al}_2\text{O}_3(100)$ supported Ce_2O_4 , the extremely high energy cost to desorb CO_2 is expected to hinder the catalytic turnover. The CO_2 desorption energy from the $\text{CeO}_2(100)$ surface is even higher. In fact, the formation of carbonate-like species was observed experimentally after introducing CO into the system and the CO conversion to CO_2 is far less than 100%.¹⁶⁵ This is concomitant to our results, suggesting that CO_2 desorption is the most likely rate-limiting step for CO oxidation in ceria-based catalysts. Compared to the unsupported Ce_2O_4 cluster, our results predict a negative effect of the $\gamma\text{-Al}_2\text{O}_3(100)$ support on CO oxidation. In contrast, all three steps on the $\text{ZrO}_2(111)$ supported Ce_2O_4 cluster are exothermic. Therefore, we expect that the $\text{ZrO}_2(111)$ substrate will promote the turnover of CO oxidation on the supported Ce_2O_4 cluster. These predictions are consistent with previous experimental observations. For example, Aguila et al. studied the oxidation of CO on $\gamma\text{-Al}_2\text{O}_3$, ZrO_2 and SiO_2 supported CeO_2 catalysts at low temperature.¹⁵⁶ They reported a higher CO conversion on ZrO_2 supported CeO_2 catalyst than on the other two supports. Putna et al. investigated CO oxidation on CeO_2 thin films supported by $\alpha\text{-Al}_2\text{O}_3$ and polycrystalline ZrO_2 .¹⁶² They found a significant fraction of CO was oxidized on the ZrO_2 supported CeO_2 thin film whereas on the $\alpha\text{-Al}_2\text{O}_3$ supported CeO_2 only very small fraction of CO was oxidized. The lattice oxygen of the supported CeO_2 islands was believed to be responsible for the oxidation reaction.¹⁶² Although exact structures of the $\gamma\text{-Al}_2\text{O}_3$, $\alpha\text{-Al}_2\text{O}_3$ and polycrystalline ZrO_2 supports used in those experiments are different from our model $\text{Ce}_2\text{O}_4/\gamma\text{-Al}_2\text{O}_3(100)$ and $\text{Ce}_2\text{O}_4/\text{ZrO}_2(111)$, we believe that our models capture a key aspect of those supported catalytic systems: the reducibility of the support. More

importantly, our results demonstrated the reactivity of the supported oxide clusters can be manipulated by using different oxide substrates.

5.4 Conclusion

First-principles density functional theory calculations were used to examine the effect of $\text{ZrO}_2(111)$ and $\gamma\text{-Al}_2\text{O}_3(100)$ as supports on the reactivity of the Ce_2O_4 clusters for CO oxidation. Our results showed that the supports do not affect the acid-base interaction, as manifested by the adsorption CO_2 and CO in upright configuration. However, for the reactive adsorption of CO, the two substrates were found to have very different impacts on the reaction energies. The reactive adsorption of CO leads to a $(\text{Ce}_2\text{O}_2)^{2+}(\text{CO}_3)^{2-}$ species with adsorption energies of -0.55 eV and -4.33 eV, on $\text{ZrO}_2(111)$ and $\gamma\text{-Al}_2\text{O}_3(100)$ supported Ce_2O_4 , respectively. The results were analyzed in the context of catalytic oxidation of CO by ceria. ZrO_2 is expected to be a more active support due to the relatively smooth potential energy profile. On the other hand, the $\gamma\text{-Al}_2\text{O}_3(100)$ -supported ceria is likely to be less efficient due to the formation of the highly stable $(\text{Ce}_2\text{O}_2)^{2+}(\text{CO}_3)^{2-}$ intermediate. The results suggest that the catalytic properties can be tailored by varying the supports.

CHAPTER 6

SUMMARY

As illustrated in the above three chapters, by choosing the proper model and theoretical method, the performance of heterogeneous catalyst systems can be studied as a function of chemical composition, molecular structure and electronic structure. Unlike experimental measurements, where the data reveal only the average of a sample, the theoretical modeling is proved to be able to pin down to the active site and yield important structural, electronic and energetic information of the reaction. Furthermore, as the metal-on-oxide systems have been intensely studied in the past decade, to our best knowledge the modeling of an oxide-on-oxide system presented in this dissertation was the first. We hope our work will shed light on even broader studies of similar highly dispersed catalytic systems.

BIBLIOGRAPHY

- (1) Thomas, J. M.; Thomas, W. J. *Principles and practice of heterogeneous catalysis*; Wiley-VCH, First Edition (1967), Second Edition (1997).
- (2) Heck, R. M.; Farrauto, R. J.; Gulati, S. T. *Catalytic air pollution control: Commercial technology* 3rd ed.; Wiley, 2009.
- (3) Steele, B. C. H.; Heinzl, A. *Nature* **2001**, *414*, 345.
- (4) Hove, M. A. V.; Weinberg, W. H.; Chan, C.-M. *Low-energy diffraction*; Springer Verlag, 1986.
- (5) Goodman, P. *Fifty years of electron diffraction*; D. Reidel Publishing, 1981.
- (6) Pendry, J. B. *Low energy electron diffraction*; Academic Press, 1974.
- (7) Binnig, G.; Rohrer, H.; Gerber, C.; Weibel, E. *Phys. Rev. Lett.* **1982**, *49*, 57.
- (8) Tersoff, J.; Hamann, D. R. *Phys. Rev. B* **1985**, *31*, 805.
- (9) Binnig, G.; Rohrer, H.; Gerber, C.; Weibel, E. *Appl. Phys. Lett.* **1982**, *40*, 178.
- (10) Humphris, A. D. L.; Miles, M. J.; Hobbs, J. K. *Appl. Phys. Lett.* **2005**, *86*.
- (11) Roiter, Y.; Minko, S. *J. Am. Chem. Soc.* **2005**, *127*, 15688.
- (12) Campbell, C. T. *J. Chem. Soc. Faraday Trans.* **1996**, *92*, 1435.
- (13) Freund, H. J.; Kuhlbeck, H.; Neumann, M. *Adsorption on ordered surfaces of ionic solids and thin films*; Springer-Verlag: Berlin, 1993; Vol. 33.
- (14) Henrich, V. E.; Cox, P. A. *The surface science of metal oxides*; Cambridge University Press: Cambridge, U.K., 1994.

- (15) Goodman, D. W. *Chem. Rev.* **1995**, 95, 523.
- (16) Campbell, C. T. *Surf. Sci. Rep.* **1997**, 27, 1.
- (17) Gunter, P. L. J.; Niemantsverdriet, J. W.; Ribeiro, F. H.; Somorjai, G. A. *Catal. Rev.-Sci. Eng.* **1997**, 39, 77.
- (18) Freund, H. J.; Kühlenbeck, H.; Staemmler, V. *Rep. Prog. Phys.* **1996**, 59, 283.
- (19) Segre, E. *From falling bodies to radio waves: Classical physicists and their discoveries*; W. H. Freeman and Company, 1984.
- (20) Schrodinger, E. *Am. Physik* **1926**, 79, 361.
- (21) Hohenberg, P.; Kohn, W. *Phys. Rev.* **1964**, 136, B864
- (22) Kohn, W.; Sham, L. J. *Phys. Rev.* **1965**, 140, A1133.
- (23) Teller, E. *Rev. Mod. Phys.* **1962**, 34, 627.
- (24) Balazs, N. *Phys. Rev.* **1967**, 156, 42.
- (25) Hartree, D. R. *Proc. Camb. Phil. Soc* **1930**, 24, 89.
- (26) Fock, F. *Zs. f. Phys* **1930**, 61, 126.
- (27) Wigner, E. P. *Faraday Soc.* **1938**, 34, 678.
- (28) Perdew, J. P.; Kurth, S. *Density functionals: Theory and applications*; Springer: Berlin, 1998.
- (29) Becke, A. D. *J. Chem. Phys.* **1993**, 98, 1372.
- (30) Kim, K.; Jordan, K. D. *J. Phys. Chem.* **1994**, 98, 10089.
- (31) Stephens, P. J.; Devlin, F. J.; Chabalowski, C. F.; Frisch, M. J. *J. Phys. Chem.* **1994**, 98, 11623.
- (32) Runge, E.; Gross, E. K. U. *Phys. Rev. Lett.* **1984**, 52, 997.

- (33) Car, R.; Parrinello, M. *Phys. Rev. Lett.* **1985**, *55*, 2471.
- (34) Arrhenius, S. *J. Phys. Chem* **1889**, *4*, 226.
- (35) Eyring, H. *J. Chem. Phys* **1935**, *3*, 107.
- (36) Eyring, H. *Chem. Rev.* **1935**, *17*, 65.
- (37) Evans, M. G.; Polanyi, M. *Trans. Faraday Soc.* **1935**, *31*, 875.
- (38) Wigner, E. *J. Chem. Phys* **1937**, *5*, 720.
- (39) Keck, J. C. *Adv. Chem. Phys.* **1967**, *13*, 85.
- (40) Marcus, R. A.; Rice, O. K. *J. Phys. Chem.* **1951**, *55*, 894.
- (41) Marcus, R. A. *J. Chem. Phys.* **1952**, *20*, 359.
- (42) Wieder, G. M.; Marcus, R. A. *J. Chem. Phys.* **1962**, *37*, 1835.
- (43) Rosentock, H. M.; Wallenstein, M. B.; Wahrhaftig, A. L.; Eyring, H. *Proc. Natl. Acad. Sci* **1952**, *38*, 667.
- (44) Henkelman, G.; Jonsson, H. *J. Chem. Phys.* **2000**, *113*, 9978.
- (45) Henkelman, G.; Uberuaga, B. P.; Jonsson, H. *J. Chem. Phys.* **2000**, *113*, 9901.
- (46) Bader, R. F. W. *Atoms in molecules - a quantum theory*; Oxford University Press: Oxford, 1990.
- (47) Henkelman, G.; Arnaldsson, A.; Jonsson, H. *Comp. Mater. Sci.* **2006**, *36*, 354.
- (48) Takahashi, N.; Shinjoh, H.; Iijima, T.; Suzuki, T.; Yamazaki, K.; Yokota, K.; Suzuki, H.; Miyoshi, N.; Matsumoto, S.; Tanizawa, T.; Tanaka, T.; Tateishi, S.; Kasahara, K. *Catal. Today* **1996**, *27*, 63.
- (49) Liu, Z. M.; Woo, S. I. *Catal. Rev.-Sci. Eng.* **2006**, *48*, 43.

- (50) William s. Epling, L. E. C. *Catal. Today* **2004**, 96, 21.
- (51) Burcham, L. J.; Wachs, I. E. *Catal. Today* **1999**, 49, 467.
- (52) Olsson, L.; Westerberg, B.; Persson, H.; Fridell, E.; Skoglundh, M.; Andersson, B. *J. Phys. Chem. B* **1999**, 103, 10433.
- (53) Fridell, E.; Persson, H.; Westerberg, B.; Olsson, L.; Skoglundh, M. *Catal. Lett.* **2000**, 66, 71.
- (54) Mahzoul, H.; Brilhac, J. F.; Gilot, P. *Appl. Catal. B-Environ.* **1999**, 20, 47.
- (55) Lietti, L.; Forzatti, P.; Nova, I.; Tronconi, E. *J. Catal.* **2001**, 204, 175.
- (56) Cant, N. W.; Patterson, M. J. *Catal. Today* **2002**, 73, 271.
- (57) Stone, P.; Ishii, M.; Bowker, M. *Surf. Sci.* **2003**, 537, 179.
- (58) Casapu, M.; Grunwaldt, J. D.; Maciejewski, M.; Wittrock, M.; Gobel, U.; Baiker, A. *Appl. Catal. B-Environ.* **2006**, 63, 232.
- (59) Szailer, T.; Kwak, J. H.; Kim, D. H.; Hanson, J. C.; Peden, C. H. F.; Szanyi, J. *J. Catal.* **2006**, 239, 51.
- (60) Szanyi, J.; Kwak, J. H.; Kim, D. H.; Burton, S. D.; Peden, C. H. F. *J. Phys. Chem. B* **2005**, 109, 27.
- (61) Broqvist, P.; Panas, I.; Fridell, E.; Persson, H. *J. Phys. Chem. B* **2002**, 106, 137.
- (62) Karlsen, E. J.; Nygren, M. A.; Pettersson, L. G. M. *J. Phys. Chem. B* **2003**, 107, 7795.
- (63) Schneider, W. F. *J. Phys. Chem. B* **2004**, 108, 273.
- (64) Branda, M. M.; Di Valentin, C.; Pacchioni, G. *J. Phys. Chem. B* **2004**, 108, 4752.

- (65) Broqvist, P.; Gronbeck, H.; Fridell, E.; Panas, I. *Catal. Today* **2004**, *96*, 71.
- (66) Broqvist, P.; Panas, I.; Gronbeck, H. *J. Phys. Chem. B* **2005**, *109*, 15410.
- (67) Gronbeck, H.; Broqvist, P.; Panas, I. *Surf. Sci.* **2006**, *600*, 403.
- (68) Tutuianu, M.; Inderwildi, O. R.; Bessler, W. G.; Warnatz, J. *J. Phys. Chem. B* **2006**, *110*, 17484.
- (69) Broqvist, P.; Gronbeck, H.; Fridell, E.; Panas, I. *J. Phys. Chem. B* **2004**, *108*, 3523.
- (70) Piacentini, m. *Top. Catal.* **2004**, *30/31*, 71.
- (71) Piacentini, M.; Maciejewski, M.; Baiker, A. *Appl. Catal. B-Environ.* **2007**, *72*, 105.
- (72) Olsson, L.; Fridell, E.; Skoglundh, M.; Andersson, B. *Catal. Today* **2002**, *73*, 263.
- (73) Hilgendorff, M. *Topics in Catalysis* **2004**, *30-31*, 155.
- (74) Ingelsten, H. H.; Skoglundh, M.; Fridell, E. *Appl. Catal. B-Environ.* **2003**, *41*, 287.
- (75) Svedberg, P.; Jobson, E.; Erkfeldt, S.; Andersson, B.; Larsson, M.; Skoglundh, M. *Top. Catal.* **2004**, *30-31*, 199.
- (76) Westerberg, B.; Fridell, E. *J. Mol. Catal. a* **2001**, *165*, 249.
- (77) Piacentini, M.; Strobel, R.; Maciejewski, M.; Pratsinis, S. E.; Baiker, A. *J. Catal.* **2006**, *243*, 43.
- (78) Abdulhamid, H.; Fridell, E.; Skoglundh, M. *Appl. Catal. B-Environ.* **2006**, *62*, 319.

- (79) Toops, T. J.; Smith, D. B.; Epling, W. S.; Parks, J. E.; Partridge, W. P. *Appl. Catal. B-Environ.* **2005**, *58*, 255.
- (80) Szanyi, J.; Kwak, J. H.; Hanson, J.; Wang, C. M.; Szailer, T.; Peden, C. H. *F. J. Phys. Chem. B* **2005**, *109*, 7339.
- (81) Dawody, J.; Skoglundh, M.; Wall, S.; Fridell, E. *J. Mol. Catal. A-Chem.* **2005**, *225*, 259.
- (82) Pinto, H. P.; Nieminen, R. M.; Elliott, S. D. *Phys. Rev. B* **2004**, *70*.
- (83) Collins, S. E.; Baltanas, M. A.; Bonivardi, A. L. *J. Phys. Chem. B* **2006**, *110*, 5498.
- (84) Piacentini, M.; Maciejewski, M.; Baiker, A. *Appl. Catal. B-Environ.* **2005**, *60*, 265.
- (85) Piacentini, M.; Maciejewski, M.; Baiker, A. *Appl. Catal. B* **2005**, *59*, 187.
- (86) Wang, C. M.; Kwak, J. H.; Kim, D. H.; Szanyi, J.; Sharma, R.; Thevuthasan, S.; Peden, C. H. *F. J. Phys. Chem. B* **2006**, *110*, 11878.
- (87) Kresse, G.; Joubert, D. *Phys. Rev. B* **1999**, *59*, 1758.
- (88) Perdew, J. P.; Burke, K.; Ernzerhof, M. *Phys. Rev. Lett.* **1996**, *77*, 3865.
- (89) Monkhorst, H. J.; Pack, J. D. *Phys. Rev. B* **1976**, *13*, 5188.
- (90) Sanville, E.; Kenny, S. D.; Smith, R.; Henkelman, G. *J. Comput. Chem.* **2007**, *28*, 899.
- (91) Zollweg, R. *Phys. Rev.* **1995**, *100*, 671.
- (92) Sun, M. Y.; Nelson, A. E.; Adjaye, J. *J. Phys. Chem. B* **2006**, *110*, 2310.
- (93) Nelson, A. E.; Sun, M. Y.; Adjaye, J. *J. Phys. Chem. B* **2006**, *110*, 20724.
- (94) Paglia, G.; Buckley, C. E.; Rohl, A. L. *J. Phys. Chem. B* **2006**, *110*, 20721.

- (95) Digne, M.; Raybaud, P.; Sautet, P.; Rebours, B.; Toulhoat, H. *J. Phys. Chem. B* **2006**, *110*, 20719.
- (96) Digne, M.; Sautet, P.; Raybaud, P.; Euzen, P.; Toulhoat, H. *J. Catal.* **2004**, *226*, 54.
- (97) Gutierrez, G.; Taga, A.; Johansson, B. *Phys. Rev. B* **2002**, *65*, 012101.
- (98) Broqvist, P.; Gronbeck, H.; Fridell, E.; Panas, I. *J. Phys. Chem. B* **2004**, *108*, 3523.
- (99) Ozensoy, E.; Szanyi, J.; Peden, C. H. F. *J. Phys. Chem. B* **2005**, *109*, 3431.
- (100) Dawody, J.; Eurenus, L.; Abdulhamid, H.; Skoglundh, M.; Olsson, E.; Fridell, E. *Appl. Catal. A-Gen.* **2005**, *296*, 157.
- (101) Du, A. J.; Smith, S. C.; Yao, X. D.; Lu, G. Q. *Journal of Physical Chemistry B* **2005**, *109*, 18037.
- (102) Bazzanella, N.; Checchetto, R.; Miotello, A.; Sada, C.; Mazzoldi, P.; Mengucci, P. *Appl. Phys. Lett.* **2006**, *89*.
- (103) Checchetto, R.; Bazzanella, N.; Miotello, A.; Mengucci, P. *J. Alloys Compd.* **2007**, *446*, 58.
- (104) Du, A. J.; Smith, S. C.; Yao, X. D.; Lu, G. Q. *J. Phys. Chem. B* **2006**, *110*, 21747.
- (105) Du, A. J.; Smith, S. C.; Yao, X. D.; Lu, G. Q. *J. Am. Chem. Soc.* **2007**, *129*, 10201.
- (106) Pozzo, M.; Alfe, D.; Amieiro, A.; French, S.; Pratt, A. *J. Chem. Phys.* **2008**, *128*.

- (107) Dolci, F.; Di Chio, M.; Baricco, M.; Giamello, E. *J. Mater. Sci.* **2007**, *42*, 7180.
- (108) Du, A. J.; Smith, S. C.; Yao, X. D.; Sun, C. H.; Li, L.; Lu, G. Q. *Appl. Phys. Lett.* **2008**, *92*.
- (109) Jung, K. S.; Kim, D. H.; Lee, E. Y.; Lee, K. S. *Catal. Today* **2007**, *120*, 270.
- (110) Grochala, W.; Edwards, P. P. *Chem. Rev.* **2004**, *104*, 1283.
- (111) Liang, G.; Huot, J.; Boily, S.; Van Neste, A.; Schulz, R. *J. Alloys Compd.* **2000**, *297*, 261.
- (112) Wagemans, R. W. P.; van Lenthe, J. H.; de Jongh, P. E.; van Dillen, A. J.; de Jong, K. P. *J. Am. Chem. Soc.* **2005**, *127*, 16675.
- (113) Li, W. Y.; Li, C. S.; Ma, H.; Chen, J. *J. Am. Chem. Soc.* **2007**, *129*, 6710.
- (114) Frisch, M. J. Gaussian 03; Gaussian Inc.: Pittsburgh, PA, 2003.
- (115) Parr, R. G.; Yang, W. *Density-functional theory of atoms and molecules*; Oxford University Press: Oxford, 1989.
- (116) Lee, C. T.; Yang, W. T.; Parr, R. G. *Phys. Rev. B* **1988**, *37*, 785.
- (117) Kresse, G.; Furthmuller, J. *Comp. Mater. Sci.* **1996**, *6*, 15.
- (118) Blochl, P. E. *Phys. Rev. B* **1994**, *50*, 17953.
- (119) Lyalin, A.; Solov'yov, I. A.; Solov'yov, A. V.; Greiner, W. *Phys. Rev. A* **2003**, *67*, 063203.
- (120) Knight, W. D. *Phys. Rev. Lett* **1984**, *52*, 2141.
- (121) Diederich, T.; Doppner, T.; Braune, J.; Tiggesbaumker, J.; Meiwes-Broer, K. H. *Phys. Rev. Lett.* **2001**, *86*, 4807.

- (122) Rao, B. K.; Jena, P. *J. Chem. Phys.* **1999**, *111*, 1890.
- (123) Kiran, B.; Jena, P.; Li, X.; Grubisic, A.; Stokes, S. T.; Gantefor, G. F.; Bowen, K. H.; Burgert, R.; Schnockel, H. *Phys. Rev. Lett.* **2007**, *98*.
- (124) Thomas, J. M.; Thomas, W. J. *Principles and practice of heterogeneous catalysis*; VCH: New York, 1997.
- (125) Ertl, G.; Knozinger, H.; Weikamp, J. T., Handbook of heterogeneous catalysis.
- (126) Al-Abadleh, H. A.; Grassian, V. H. *Surf. Sci. Rep.* **2003**, *52*, 63.
- (127) Cheng, L.; Ge, Q. F. *Surf. Sci.* **2007**, *601*, L65.
- (128) Cheng, L.; Ge, Q. F. *J. Phys. Chem. C* **2008**, *112*, 16924.
- (129) Kwak, J. H.; Mei, D.; Yi, C. W.; Kim, D. H.; Peden, C. H. F.; Allard, L. F.; Szanyi, J. *J. Catal.* **2009**, *261*, 17.
- (130) Mei, D.; Ge, Q.; Kwak, J. H.; Kim, D. H.; Szanyi, J.; Peden, C. H. F. *J. Phys. Chem. C.* **2008**, *112*, 18050.
- (131) Backhaus-Ricoult, M. *Annu. Rev. Mater. Res.* **2003**, *33*, 55.
- (132) Wachs, I. E.; Weckhuysen, B. M. *Appl. Catal. A-Gen.* **1997**, *157*, 67.
- (133) Deo, G.; Wachs, I. E. *J. Catal.* **1994**, *146*, 323.
- (134) Hu, H. C.; Wachs, I. E. *J. Phys. Chem.* **1995**, *99*, 10911.
- (135) Kim, D. S.; Wachs, I. E.; Segawa, K. *J. Catal.* **1994**, *149*, 268.
- (136) Niwa, M.; Sano, M.; Yamada, H.; Murakami, Y. *J. Catal.* **1995**, *151*, 285.
- (137) Yamada, H.; Niwa, M.; Murakami, Y. *Appl. Catal. A-Gen.* **1993**, *96*, 113.
- (138) Matsuoka, Y.; Niwa, M.; Murakami, Y. *J. Phys. Chem.* **1990**, *94*, 1477.

- (139) Wachs, I. E.; Deo, G.; Kim, D. S.; Vuurman, M. A.; Hu, H.; Ozkan, U. S.; Solymosi, F.; Datye, A. K.; Trifiro, F.; Iwasawa, Y.; Vanommen, J. G.; Andersson, A.; Jozwiak, W. K.; Wang, D.; Thomas, J. M.; Krauss, H. L.; Bordes, E.; Kung, H. H.; Dixit, L. *Stud. Surf. Sci. Catal.* **1993**, *75*, 543.
- (140) Freund, H. J.; Kuhlenbeck, H.; Staemmler, V. *Reports on Progress in Physics* **1996**, *59*, 283.
- (141) Schubert, M. M.; Hackenberg, S.; van Veen, A. C.; Muhler, M.; Plzak, V.; Behm, R. J. *J. Catal.* **2001**, *197*, 113.
- (142) Comotti, M.; Li, W. C.; Spliethoff, B.; Schuth, F. *J. Am. Chem. Soc.* **2006**, *128*, 917.
- (143) Panagiotopoulou, P.; Kondarides, D. I. *Catal. Today* **2006**, *112*, 49.
- (144) Mul, G.; Zwijnenburg, A.; van der Linden, B.; Makkee, M.; Moulijn, J. A. *J. Catal.* **2001**, *201*, 128.
- (145) Stangland, E. E.; Stavens, K. B.; Andres, R. P.; Delgass, W. N. *J. Catal.* **2000**, *191*, 332.
- (146) Kalvachev, Y. A.; Hayashi, T.; Tsubota, S.; Haruta, M. *J. Catal.* **1999**, *186*, 228.
- (147) Waters, R. D.; Weimer, J. J.; Smith, J. E. *Catal. Lett.* **1995**, *30*, 181.
- (148) Haruta, M. *Cattech* **2002**, *6*, 102.
- (149) Campbell, C. T.; Peden, C. H. F. *Science* **2005**, *309*, 713.
- (150) Yang, J.; Sudik, A.; Siegel, D. J.; Halliday, D.; Drews, A.; Carter, R. O.; Wolverton, C.; Lewis, G. J.; Sachtler, J. W. A.; Low, J. J.; Faheem, S. A.; Lesch, D. A.; Ozolins, V. *J. Alloys Compd.* **2007**, *446*, 345.

- (151) Trovarelli, A. *Catal. Rev.-Sci. Eng.* **1996**, 38, 439.
- (152) Trovarelli, A. *Catalysis by ceria and related materials*; Imperial College Press: UK, 2002.
- (153) Gamarra, D.; Belver, C.; Fernandez-Garcia, M.; Martinez-Arias, A. *J. Am. Chem. Soc.* **2007**, 129, 12064.
- (154) Ganduglia-Pirovano, M. V.; Hofmann, A.; Sauer, J. *Surf. Sci. Rep.* **2007**, 62, 219.
- (155) Kaspar, J.; Fornasiero, P.; Graziani, M. *Catal. Today* **1999**, 50, 285.
- (156) Aguila, G.; Gracia, F.; Araya, P. *Appl. Catal. A-Gen.* **2008**, 343, 16.
- (157) Madier, Y.; Descorme, C.; Le Govic, A. M.; Duprez, D. *J. Phys. Chem. B* **1999**, 103, 10999.
- (158) Martinez-Arias, A.; Fernandez-Garcia, M.; Salamanca, L. N.; Valenzuela, R. X.; Conesa, J. C.; Soria, J. *J. Phys. Chem. B* **2000**, 104, 4038.
- (159) Reddy, B. M.; Lakshmanan, P.; Bharali, P.; Saikia, P.; Thrimurthulu, G.; Muhler, M.; Grunert, W. *J. Phys. Chem. C* **2007**, 111, 10478.
- (160) Sayle, D. C.; Maicaneanu, S. A.; Watson, G. W. *J. Am. Chem. Soc.* **2002**, 124, 11429.
- (161) Deo, G.; Wachs, I. E. *J. Phys. Chem.* **1991**, 95, 5889.
- (162) Putna, E. S.; Bunluesin, T.; Fan, X. L.; Gorte, R. J.; Vohs, J. M.; Lakis, R. E.; Egami, T. *Catal. Today* **1999**, 50, 343.
- (163) Reddy, B. M.; Bharali, P.; Saikia, P.; Thrimurthulu, G.; Yamada, Y.; Kobayashi, T. *Ind. Eng. Chem. Res.* **2009**, 48, 453.

- (164) Reddy, B. M.; Saikia, P.; Bharali, P.; Park, S. E.; Muhler, M.; Grunert, W. *J. Phys. Chem. C* **2009**, *113*, 2452.
- (165) Sasikala, R.; Gupta, N. M.; Kulshreshtha, S. K. *Catal. Lett.* **2001**, *71*, 69.
- (166) Wang, R.; Crozier, P. A.; Sharma, R.; Adams, J. B. *Nano Lett.* **2008**, *8*, 962.
- (167) Reddy, B. M.; Khan, A. *Catal. Surv. Asia* **2005**, *9*, 155.
- (168) Wang, R. G.; Crozier, P. A.; Sharma, R.; Adams, J. B. *J. Phys. Chem. B* **2006**, *110*, 18278.
- (169) Fabris, S.; Vicario, G.; Balducci, G.; de Gironcoli, S.; Baroni, S. *J. Phys. Chem. B* **2005**, *109*, 22860.
- (170) Piinkerton, F. E.; Meyer, M. S.; Meisner, G. P.; Balogh, M. P.; Vajo, J. J. *J. Phys. Chem. C* **2007**, *111*, 12881.
- (171) Nolan, M.; Parker, S. C.; Watson, G. W. *Phys. Chem. Chem. Phys.* **2006**, *8*, 216.
- (172) Huang, M.; Fabris, S. *J. Phys. Chem. C* **2008**, *112*, 8643.
- (173) Stefanovich, E. V.; Shluger, A. L.; Catlow, C. R. A. *Phys. Rev. B* **1994**, *49*, 11560.
- (174) Kwak, J. H.; Hu, J. Z.; Kim, D. H.; Szanyi, J.; Peden, C. H. F. *J. Catal.* **2007**, *251*, 189.
- (175) Bolis, V.; Morterra, C.; Volante, M.; Orio, L.; Fubini, B. *Langmuir* **1990**, *6*, 695.
- (176) Morterra, C.; Aschieri, R.; Volante, M. *Mater. Chem. Phys.* **1988**, *20*, 539.

- (177) Paukshtis, E. A. *Infrared spectroscopy in heterogeneous acid-base catalysis*; Nauka: Novosibirsk, 1992.
- (178) Christensen, A.; Carter, E. A. *Phys. Rev. B* **1998**, *58*, 8050.
- (179) Zecchina, A.; Platero, E. E.; Arean, C. O. *J. Catal.* **1987**, *107*, 244.
- (180) Morterra, C.; Magnacca, G. *Catal. Today* **1996**, *27*, 497.
- (181) Pan, Y.; Liu, C.-j.; Ge, Q. *Langmuir* **2008**, *24*, 12410.
- (182) Tai, J. R.; Ge, Q. F.; Davis, R. J.; Neurock, M. *J. Phys. Chem. B* **2004**, *108*, 16798.
- (183) Turek, A. M.; Wachs, I. E.; Decanio, E. *J. Phys. Chem.* **1992**, *96*, 5000.
- (184) Li, C.; Sakata, Y.; Arai, T.; Domen, K.; Maruya, K.; Onishi, T. *J. Chem. Soc. Faraday Trans. 1* **1989**, *85*, 929.
- (185) Li, C.; Sakata, Y.; Arai, T.; Domen, K.; Maruya, K. I.; Onishi, T. *J. Chem. Soc. Faraday Trans. 1* **1989**, *85*, 1451.
- (186) Thomas, J. R.; Deleeuw, B. J.; Vacek, G.; Crawford, T. D.; Yamaguchi, Y.; Schaefer, H. F. *J. Chem. Phys.* **1993**, *99*, 403.
- (187) Liu, X. W.; Zhou, K. B.; Wang, L.; Wang, B. Y.; Li, Y. D. *J. Am. Chem. Soc.* **2009**, *131*, 3140.
- (188) Sayle, T. X. T.; Parker, S. C.; Sayle, D. C. *Phys. Chem. Chem. Phys.* **2005**, *7*, 2936.
- (189) Aneggi, E.; Llorca, J.; Boaro, M.; Trovarelli, A. *J. Catal.* **2005**, *234*, 88.

APPENDICES

APPENDIX I. VASP Input Files

INCAR

System = Mg surface

Start parameter for this Run:

NWRITE = 2; LPETIM=F *write-flag & timer*
ENCUT = 450.0
PREC = high
ISTART = 0 *job : 0-new 1-cont 2-samecut*
ICHARG = 2 *charge: 1-file 2-atom 10-const*
ISPIN = 1 *spin polarized calculation?*
INIWAV = 1 *electr: 0-lowe 1-rand 2-diag*
NELM = 200; NELMIN= 2; NELMDL= 0 *# of ELM steps*
EDIFF = .5E-04 *stopping-criterion for ELM*

Ionic Relaxation

EDIFFG = .5E-03 *stopping-criterion for IOM*
NSW = 1 *number of steps for IOM*
NBLOCK = 1; KBLOCK = 115 *inner block; outer block*
IBRION = 2 *ionic relax: 0-MD 1-quasi-New 2-CG*
ISIF = 2
IWAVPR = 1 *prediction: 0-non 1-charg 2-wave 3-comb*
ISYM = 2 *0-nonsym 1-usesym*
LCORR = T *Harris-correction to forces*
POTIM = 0.500 *time-step for ion-motion*
TEIN = 5000.0 *initial temperature*
SMASS = -1 *Nose mass-parameter (am)*

Electronic Relaxation 2

IALGO = 48 *algorithm*
LDIAG = T *sub-space diagonalisation*
LREAL = F *real-space projection*
LPLANE = T
NPAR = 1
LSCALU = F
NSIM = 4
LORBIT = 12

DOS related values:

EMIN = 10.00; EMAX = -10.00 *energy-range for DOS*
ISMEAR = 0; SIGMA = 0.1 *broadening in eV -4-tet -1-fermi 0-gaus*

POTCAR

PAW_PBE Mg 05Jan2001

2.000000000000000000

parameters from PSCTR are:

VRHFIN =Mg: s2p0

LEXCH = PE

EATOM = 23.0029 eV, 1.6907 Ry

TITEL = PAW_PBE Mg 05Jan2001

LULTRA = F use ultrasoft PP ?

IUNSCR = 1 unscreen: 0-lin 1-nonlin 2-no

RPACOR = 2.000 partial core radius

POMASS = 24.305; ZVAL = 2.000 mass and valenz

RCORE = 2.000 outmost cutoff radius

RWIGS = 2.880; RWIGS = 1.524 wigner-seitz radius (au A)

ENMAX = 210.012; ENMIN = 157.509 eV

ICORE = 2 local potential

LCOR = T correct aug charges

LPAW = T paw PP

EAUG = 274.554

DEXC = -.136

RMAX = 3.182 core radius for proj-oper

RAUG = 1.300 factor for augmentation sphere

RDEP = 2.025 radius for radial grids

QCUT = -3.929; QGAM = 7.858 optimization parameters

Description

1 E TYP RCUT TYP RCUT

0 .000 23 2.000

0 2.000 23 2.000

1 .000 23 2.000

1 2.000 23 2.000

2 .000 23 2.000

Error from kinetic energy argument (eV)

NDATA = 100

STEP = 20.000 1.050

1.04 1.03 1.03 1.02 1.02 1.00 .983 .970

.942 .908 .890 .851 .809 .764 .718 .671

.623 .576 .530 .463 .421 .381 .324 .290

.258 .214 .176 .154 .124 .991E-01 .781E-01 .607E-01

.465E-01 .352E-01 .262E-01 .192E-01 .123E-01 .875E-02 .546E-02 .386E-02

.254E-02 .184E-02 .153E-02 .142E-02 .140E-02 .140E-02 .137E-02 .128E-02

.116E-02 .986E-03 .794E-03 .646E-03 .483E-03 .354E-03 .248E-03 .195E-03

.....

.110411849401E-01 .222294381191E-02 -.769082318013E-02 -.188122184779E-01 -

.312592923923E-01

-.451552348125E-01 -.606274240112E-01 -.778063850533E-01 -.968246278328E-01 -
.117815051255E+00
-.140908114251E+00 -.166226693095E+00 -.193878249699E+00 -.223945644936E+00 -
.256478870224E+00

End of Dataset

PAW_PBE H 15Jun2001

1.0000000000000000

parameters from PSCTR are:

VRHFIN =H: ultrasoft test

LEXCH = PE

EATOM = 12.4884 eV, .9179 Ry

TITEL = PAW_PBE H 15Jun2001

LULTRA = F use ultrasoft PP ?

IUNSCR = 0 unscreen: 0-lin 1-nonlin 2-no

RPACOR = .000 partial core radius

POMASS = 1.000; ZVAL = 1.000 mass and valenz

RCORE = 1.100 outmost cutoff radius

RWIGS = .700; RWIGS = .370 wigner-seitz radius (au A)

ENMAX = 250.000; ENMIN = 200.000 eV

RCLOC = .701 cutoff for local pot

LCOR = T correct aug charges

LPAW = T paw PP

EAUG = 400.000

RMAX = 2.174 core radius for proj-oper

RAUG = 1.200 factor for augmentation sphere

RDEP = 1.112 radius for radial grids

QCUT = -5.749; QGAM = 11.498 optimization parameters

.....

.218291785052E+00 .231111285582E+00 .244653165208E+00 .258955547168E+00
.274058360669E+00

.290003411772E+00 .306834456261E+00 .324597274563E+00 .343339748817E+00
.363111942119E+00

.383966180135E+00 .405957135129E+00 .429141912617E+00 .453580140822E+00
.479334063113E+00

.506468633774E+00 .535051617308E+00 .565153691761E+00 .596848556376E+00
.630213044198E+00

.665327240103E+00 .702274605035E+00 .741142107159E+00 .782020360869E+00
.825003774715E+00

.870190709396E+00 .917683647268E+00 .967589374872E+00 .102001918033E+01
.107508906766E+01

.113291999036E+01 .119363810694E+01 .125737506141E+01 .132426829240E+01
.139446137456E+01

.146810439717E+01 .154535438480E+01 .162637576612E+01 .171134089760E+01
.180043064973E+01

.189383506471E+01 .199175409551E+01 .209439843814E+01

End of Dataset

POSCAR

System: Mg₁₀H₂cluster

1.0000000000000000

20.0000000000000000	0.0000000000000000	0.0000000000000000
0.0000000000000000	20.0000000000000000	0.0000000000000000
0.0000000000000000	0.0000000000000000	20.0000000000000000

10 2

Direct

0.3024582491600278	0.3223225089071744	0.1975114696982939
0.4392890084967666	0.2485222338819169	0.1940740464683674
0.5112309247480651	0.3781776000761421	0.2237877554118134
0.3602572435061475	0.2597495995746340	0.3274403435789272
0.3712669872237620	0.4538305050257938	0.2276336207534491
0.4300904730949092	0.3898751586293988	0.3608118596951291
0.4932382803046711	0.5075843311194194	0.2948241745509927
0.5113223105808880	0.2660293457359018	0.3261589719714888
0.2809929479054621	0.3887775668772402	0.3314743448823219
0.4138569692793003	0.3703656961723810	0.1075264382392041
0.4300904730949092	0.3608118596951291	0.3223225089071744
0.4300904730949092	0.2660293457359018	0.3314743448823219

KPOINTS

For Surfaces:

K-Point Grid

0

Monkhorst Pack

3 3 1

0 0 0

For Clusters:

K-Point Grid

0

Monkhorst Pack

1 1 1

0 0 0

For Clusters:

K-Point Grid

0

Monkhorst Pack

3 3 4

0 0 0

APPENDIX II. Gaussian Input Files

Structure optimization:

%chk=Mg10_2+.chk *directory for checkpoint file*
%mem=300MB *specify the memory usage*
b3lyp/6-31+g(d,p) opt *specify calculation type and basis set*

Title Card Required

2 1 *charge and spin state*
Mg 6.4 6.2 4.5 *coordinates(Cartesian)*
Mg 8.7 4.3 5.0
Mg 9.4 7.0 3.9
Mg 7.1 5.2 7.3
Mg 7.3 9.1 4.7
Mg 8.2 7.9 7.3
Mg 10.4 9.1 5.7
Mg 10.4 6.1 6.6
Mg 9.2 6.0 9.2
Mg 5.3 7.7 6.7

Transition state locating

%chk=Mg10_2+_TS.chk
%mem=300MB
PBE/6-31+g(d,p) opt=(ts,EstmFC) freq *transition state and frequency calculation*
geom=check guess=read iop(5/13=1,1/11=1) *structure read from checkpoint*

Title Card Required

2 1 *structure will be read from checkpoint, no coordinate input*

IRC calculation

%chk=Mg10-TS.chk *checkpoint file must be an optimized transition state*
%mem=300MB
IRC=(reverse,calcFC,MaxPoints=30,internal) *thirty IRC steps*
Iop(5/13=1,2/16=1) PBE/6-31+g(d,p) geom=check guess=read

Title Card Required

0 1

VITA

Graduate School
Southern Illinois University

Lei Cheng

Date of Birth: May 17, 1981

500 W. Charles Rd. #26, Carbondale, IL 62901

Shengli Str. #26, Rushan, Shandong 264500, China

leicheng@siu.edu

Qingdao University, Qingdao, China,

Bachelor of Science, Polymer Synthesis, July 2003

Dissertation Title: FIRST-PRINCIPLES DENSITY FUNCTIONAL THEORY STUDIES
OF REACTIVITIES OF HETEROGENEOUS CATALYSTS DETERMINED BY
STRUCTURE AND SUBSTRATE

Major Professor: Qingfeng Ge

Publications:

Lei Cheng and Qingfeng Ge, *Surf. Sci.* 601, L65-L68 (2007)

Lei Cheng and Qingfeng Ge, *J. Phys. Chem. C*, 112, 16924 (2008)

Lei Cheng, Donghai Mei and Qingfeng Ge, *J. Phys. Chem. C*, 113, 18296 (2009)

Lei Cheng, Jianjun Liu and Qingfeng Ge (in preparation)